

The Pennsylvania State University
The Graduate School
Department of Electrical Engineering

**MULTI-WAVELENGTH RAMAN-RAYLEIGH LIDAR FOR
ATMOSPHERIC REMOTE SENSING**

A Thesis in
Electrical Engineering

by

Yi-Chung Rau

Copyright 1994 Yi-Chung Rau

Submitted in Partial Fulfillment
of the Requirements
for the Degree of

Doctor of Philosophy

May 1994

We approve the thesis of Yi-Chung Rau.

Date of Signature

C. Russell Philbrick
Professor of Electrical Engineering
Thesis Advisor
Chair of Committee

Craig F. Bohren
Distinguished Professor of Meteorology

Charles L. Croskey
Associate Professor of Electrical Engineering

John D. Mathews
Professor of Electrical Engineering

John Mitchell
Professor of Electrical Engineering

Larry C. Burton
Professor of Electrical and Computer Engineering
Head of the Department of Electrical Engineering

ABSTRACT

Several different lidar analysis techniques have been applied to the measurements of atmospheric properties, with particular emphasis on temperature profile from the ground to 80 km using the Penn State lidar instrument. These different lidar techniques are the molecular scattering (Rayleigh) lidar with wavelength at 532 nm or 355 nm , the two-wavelength lidar using the combination of returns from wavelengths at 532 nm and 355 nm , and the molecular nitrogen scatter Raman lidar at a wavelength of 607 nm . In the upper stratosphere and mesosphere, from 30 km to 80 km , the single-wavelength molecular scatter lidar technique has proven successful and has been demonstrated to be preferable for measurements of atmospheric density and temperature using the molecular backscattered signal.

An important result from two-wavelength lidar is the ability to define the minimum height range that can be used for molecular scatter analysis. Further, the two-wavelength lidar technique has limited use for the stratospheric density and temperature measurements, this technique has been used to separate the molecular and particle portion of the backscattered signal in the upper region of the stratospheric volcanic aerosol layer, 27 km to about 35 km . By observing the two-wavelength particle backscatter ratio, we monitored the presence of volcanic particles and concluded that there were usually two or more particle types in the stratospheric aerosol layer during the LADIMAS Campaign, October through December 1991.

The tropospheric density and temperature profiles have been determined from the transmission-corrected vibrational N_2 Raman channel signal, under some atmospheric conditions. Density and temperature measurements, using the N_2 Raman signal, were compared with the results of balloon measurements and generally good agreement was found from 1 km to 15 km , when the troposphere was cloudless. We found that the quality of the retrieved tropospheric density and temperature profiles, obtained above the boundary layer, depends upon there being

no strong layers of clouds present. The tropospheric extinction profile has been derived from the vibrational Raman N_2 signal by using the difference between the signal profile and a model or a balloon measured density profile. More recently, the rotational Raman technique has provided accurate tropospheric temperature measurements from the ground to 5 km, even in the presence of tropospheric aerosols and thin cloud layers.

This research effort has investigated the conditions of applicability of molecular scattering (Rayleigh) lidar, two-wavelength Rayleigh lidar, and vibrational Raman and rotational Raman lidar techniques. The two-wavelength lidar technique can identify regions containing aerosols, and show when the dominant aerosol type changes. We have demonstrated the limitations and potential capabilities of Rayleigh and Raman techniques. Vibrational and rotational components of the Raman scatter can be used for measurements of atmospheric structure properties and for definition of the optical environment.

TABLE OF CONTENTS

LIST OF TABLES	vii
LIST OF FIGURES	viii
ACKNOWLEDGMENTS	xii
Chapter 1 INTRODUCTION	1
1.1 Background	1
1.2 Historical Review of Laser Remote Sensing	2
1.3 Lidar System Configuration	13
1.3.1 Transmitter	16
1.3.2 Receiver and Detector	16
1.3.3 Data Processing and Storage Unit	19
1.4 Statement of the Problem	21
1.5 Thesis Organization	24
Chapter 2 MOLECULAR SCATTERING LIDAR DATA ANALYSIS	25
2.1 Molecular (Rayleigh) Scattering Lidar Equation	25
2.2 AIDA Campaign Data Analysis	27
2.3 Photon Signal Processing	32
2.3.1 Background Noise Determination and Substraction	33
2.3.2 Profile Filtering and Smoothing	34
2.3.3 Background Substraction before or after Smoothing	35
2.4 Atmospheric Profiles	40
2.4.1 Backscatter Ratio Profile	40
2.4.2 Density and Density Ratio Profiles	42
2.4.3 Temperature Profile	46
Chapter 3 MULTI-WAVELENGTH LIDAR DETECTION OF AEROSOL AND ATMOSPHERIC PROPERTIES	50
3.1 Multi-wavelength Lidar for Particle Detection	51
3.2 Two-Wavelength Lidar Atmospheric Properties	64

3.2.1 Numerical Approach of Two-Wavelength Lidar Inversion Algorithm	65
3.2.2 Two-Wavelength Inversion Algorithm	70
3.3 Summary of Chapter	77
Chapter 4 ATMOSPHERIC PROFILING USING THE RAMAN TECHNIQUE	80
4.1 Raman Scattering Process	81
4.1.1 Stokes and Anti-Stokes Raman Lines	81
4.1.2 Vibrational Raman Scattering	82
4.1.3 Rotational Raman Scattering	84
4.2 Raman Backscattering and Atmospheric Measurements	88
4.3 Raman Lidar Atmospheric Properties Measurements	90
4.3.1 Using Raman Techniques to Measure Extinction coefficient and Atmospheric Transmission	90
4.3.2 Raman Lidar Density and Temperature Measurements	94
4.4 Raman Lidar Optical Properties Measurements	101
4.5 Summary of Chapter	103
Chapter 5 CONCLUSIONS AND SUGGESTED FUTURE WORK	111
5.1 Summary and Conclusions	111
5.2 Recommendation for Future Work	116
Bibliography	118

LIST OF TABLES

I.	Comparison of optical interaction processes applicable to laser remote sensing methods in the atmosphere	7
II.	Transmitter parameters of Penn State LAMP lidar system	17
III.	Receiver parameters of Penn State LAMP lidar system	20
IV.	Two-wavelength particle backscatter ratio (R_{12}) at the stratospheric aerosol layer during LADIMAS Campaign '91, with the corresponding one standard deviation error, the average stratospheric aerosol wavelength dependence \bar{Q} , and its range.	60
V.	First Stokes lines of O_2 , N_2 and H_2O	82
VI.	Vibrational Raman N_2 channel extinction coefficient, cloud thickness and location, and temperature profiling quality	107

LIST OF FIGURES

1.1.	Schematic and physical description of the various lidar remote sensing techniques (after Measures, 1984).	5
1.2.	The configuration of the biaxial monostatic lidar transmitter and receiver.	14
1.3.	The operational diagram of The Penn State LAMP lidar system (coaxial monostatic type) consisting of transmitter, receiver, and detector.	15
1.4.	Atmospheric transmittance varies with altitude from surface to 100 km (Calculated from Lowtran 7, [Kneizys <i>et al.</i> 1988]).	18
1.5.	The atmospheric density and temperature profiles from U.S. Standard Atmosphere, 1976, measured with applicable lidar techniques.	23
2.1.	A whole night raw photocount profile has been constructed from sodium resonant lidar measurements taken on 5/6 April 1989. The sodium layer is shown in the altitude range from 80 to 110 km. The dip at 10 km is caused by detector gain switching.	28
2.2.	The data record checking region of photocount data profile taken on 5/6 April 1989, during AIDA Campaign.	30
2.3.	This figure juxtaposes examples of good and bad records taken on 25/26 March 1989, during the AIDA Campaign, record #1 is valid data, record #2 and #3 are bad records.	31
2.4.	An example of an individual profile of data (26 seconds integration) ratio to mean night photocount profile, before the profile smoothing.	36
2.5.	The Hanning (raised cosine) filter was used to smooth profile of individual (26 seconds integration) photocount ratio to mean night photocount.	37
2.6.	An example of data illustrating the comparison of smoothing procedures applied to a high altitude channel data, measured at 03:20 UT, 3 December 1991, by The Penn State LAMP lidar during LADIMAS Campaign.	39
2.7.	Two-wavelength lidar backscatter ratio profiles, $R(Z)$, and aerosol backscatter ratio profiles, $R(Z)-1$, measured at 22:00 UT, 22 November 1991, during the LADIMAS Campaign. Volcanic dust, cloud and aerosol layers are shown at different altitudes.	41
2.8.	An example of an one hour density profile measured at 8 pm local time, 30 March 1989, during the AIDA Campaign.	43
2.9.	The hourly density ratio to U.S. Standard Atmosphere 1976 profile measured at 8 pm local time, 30 March 1989, during AIDA Campaign.	44

LIST OF FIGURES (CONTINUED)

2.10.	The mean-night density ratio profile measured on 15/16 January 1989 during AIDA Campaign. Dotted lines are one standard deviation error lines.	45
2.11.	The mean-night temperature profile measured on 15/16 January 1989 during AIDA Campaign. Dotted lines are one standard deviation error lines.	49
3.1.	The lidar backscatter ratio profile, $R(Z)$, and particle ratio profile, $R(Z)-I$ measured at 03:20 UT on 3 December 1991.	54
3.2.	The lidar backscatter ratio profiles of 532 nm and 355 nm measured at 22:00 UT on 22 November 1991.	56
3.3.	The two-wavelength particle backscatter ratio (R_{12}), β_{a1}/β_{a2} , measured at 22:00 UT on 22 November 1991.	58
3.4.	The two-wavelength lidar return profiles and two-wavelength particle backscatter ratio (R_{12}) profile measured at 09:28 UT on 29 March 1992.	61
3.5.	The several night's two-wavelength particle backscatter ratio (R_{12}) profiles in the altitude from 15 to 35 km, measured on 1122/2200, 1122/0121, 1203/0419, 1203/0452, 1204/0207, 1204/0241, 0329/0844, and 0329/0928.	63
3.6.	The two-wavelength lidar profiles and R_{12} profile measured at 03:20 UT on 3 December 1991 from ground to 40 km.	69
3.7.	The molecular density profiles derived from two-wavelength lidar equations by assuming one size of particles at stratospheric volcanic aerosol layer.	71
3.8.	The molecular density profiles derived from two-wavelength lidar equations by letting the wavelength dependence q fixed at 0.6 in the altitude range 23 to 26 km, and changing from 1 to 1.5 otherwise.	72
3.9.	The two-wavelength lidar derived density, density ratio, and temperature profiles with corresponding R_{12} profile measured at 22:00 UT on 22 November 1991.	74
3.10.	The two-wavelength lidar derived density, density ratio, and temperature profiles with corresponding R_{12} profile measured at 3:20 UT on 3 December 1991.	75
3.11.	The two-wavelength lidar derived density, density ratio, and temperature profiles with corresponding R_{12} profile measured at 5:28 UT on 3 December 1991.	76
3.12.	The consecutive two-wavelength particle backscatter ratio (R_{12}) profiles measured on 3 December 1991.	78
4.1.	The schematic representation of Raman vibrational Stokes scattering.	83

LIST OF FIGURES (CONTINUED)

4.2.	The theoretical distribution of vibrational-rotational Raman spectrum ($\nu = 0$ to 1 vibrational transition) at 300 K (after Inaba, 1972).	85
4.3.	The molecular Raman shifted from 532 nm of N_2 , O_2 , and H_2O	86
4.4.	The envelop of rotational Raman spectrum, the Raman rotational spectral envelop changes shape as a function of temperature.	87
4.5.	Extinction coefficient and transmission profiles have been derived from $607\text{ nm } N_2$ Raman channel signal measured at 22:00 UT on 22 November 1991.	93
4.6.	The original and transmission corrected $607\text{ nm}, N_2$ Raman channel signal profiles measured at 22:00 UT on 22 November 1991.	94
4.7.	The low altitude two wavelengths, N_2 and H_2O Raman signal profiles, and R_{12} profiles measured at 22:00 UT on 22 November 1991.	96
4.8.	The Raman signal, normalized balloon density, extinction coefficient, and transmission profiles measured at 22:00 UT on 22 November 1991. Three extinction coefficient and transmission profiles were derived from the difference between Raman 607 nm channel signal profile and normalized balloon, or model, profile, and 532 nm channel signal profile by Klett inversion.	97
4.9.	Density ratio and temperature profiles have been derived from $607\text{ nm } N_2$ Raman signal profile. The derived temperature profile is compared with the balloon measurement. One standard deviation error is the lidar measurement error. . . .	100
4.10.	Atmospheric properties profiles at 22:00 UT on 22 November 1991, were derived from transmission corrected Raman N_2 channel signal and compared with the profiles without transmission correction.	101
4.11.	Density ratio and temperature profiles were derived from transmission corrected $607\text{ nm } N_2$ Raman signal measured at 03:25 UT on 4 December 1991. A cloud layer distributed from 2 to 4 km altitude is shown which made the vibration Raman channel atmospheric profiles retrieval difficult.	103
4.12.	The Raman signal, normalized balloon density, derived extinction coefficient and transmission profiles measured at 03:25 UT on 4 December 1991. Two extinction coefficient and transmission profiles were derived from the difference between Raman 607 nm channel signal profile and normalized balloon, or model, profile. The existence of lower altitude cloud layer is evident.	104
4.13.	The Raman channel signal derived extinction coefficient and transmission profiles on a cloudy condition measured at 00:28 UT on 24 November 1991.	105

LIST OF FIGURES (CONTINUED)

- 4.14. The density ratio and temperature profiles derived from transmission corrected 607 nm N_2 Raman signal misread at 00:28 UT on 24 November 1991. The cloudy condition made vibration Raman channel atmospheric profiling unsuccessful. 106
- 4.15. Rotational N_2 Raman temperature measurement at 02:09 UT on 13 June 1993, from ground to 5 km has been compared with balloon released at 02:30 UT, 13 June 1993. On the right, two profiles show the 30 minutes integrated photocount at 528 nm and 530 nm . On the left, the solid line is the rotational Raman lidar temperature measurement and the dotted line is the balloon measurement [McKinley, 1994]. 109
- 5.1. The summarized density ratio and temperature profiles by different lidar techniques on 5 December 1991. Derived temperature profile is compared with the U.S. Standard Atmosphere, 1976.. 114

ACKNOWLEDGMENTS

The author wishes to express his appreciation to Dr. C. Russell Philbrick under whose guidance this research was performed, and for his untiring advice throughout the preparation of this dissertation. He would also like to thank Dr. Craig F. Bohren for his helpful discussions in science and in dissertation preparation. Special appreciation is extended to Dr. Charles L. Croskey, and Dr. John D. Mitchell, for their thoughtful advice and helpful discussion on this dissertation.

Thanks are due to Tim Stevens, Dave Machuga, Subha Maravada, George Evanisko, Steve Mckinley, Paul Haris, Sumati Rajan, and Jim Yurack for their help and contributions. The author would also like to thank Dr. Dan Lysak, Byron Chen, Qihou Zhou, Tom Petach, and Glenn Pancoast for their contributions as well. The author is grateful for Dr. Yu Tong Morton and Dr. John Morton for their valuable discussion, encouragement, help and friendship. Special thanks go to CSSL secretaries Linda Kellerman, Julie Corl, Doris Croskey, and Elaine Lethbridge for their great help and friendship during these years. The author likes to thank his parents for their support, both morally and financially through all these years. Finally, the author would like to thank his wife, Pei-chin, for her tireless reviewing and editing, and for without her continuing support this dissertation could not have been possible. As parents-to-be, the author and his wife will like to say welcome to their beloved coming baby who will join the family in the mid-September.

Part of work done in this thesis is based on data collected by National Science Foundation's CEDAR (Coupling Energetics and Dynamics of Atmospheric Regions) lidar in Arecibo Observatory during the AIDA campaign. The LAMP system has been supported by PSU/ARL project initiation funds, Penn State College of Engineering, Lidar Atmospheric Profile Sensor (LAPS) development program for the US Navy, and NSF CEDAR Program.

Chapter 1

INTRODUCTION

1.1 Background

The scattering of electromagnetic radiation by atmospheric molecules provides the basis for using lasers to detect and to monitor atmospheric constituents (N_2 , O_2 , H_2O , O_3 , CO_2 , etc.), and properties (pressure, density, temperature, etc.). The laser provides a versatile tool for remotely profiling and monitoring the physical properties of the atmosphere. Since the invention of lasers, developments have led to higher power, higher repetition rate, narrow-linewidth performance at many different wavelengths, near diffraction-limited performance, and higher reliability. These developments provide the capability for many different remote sensing techniques and allow the monitoring of atmospheric properties with high resolution in both time and space. The high resolution of laser remote sensing techniques can provide three-dimensional distributions of atmospheric constituents or structure properties.

The laser remote sensing technique called "lidar" (an acronym for Light Detection And Ranging) involves the measurement of backscattered radiation from atmospheric atoms, molecules, particles or any solid target placed in the beam path. Lidar measures backscattered intensity from the detection of returned signals at the emitted laser frequency and at other frequencies shifted by the energy states of molecules. In a region which contains only molecules, density and temperature profiles can be determined directly from lidar measurements. A fraction of the radiation which is scattered and shifted to wavelengths different from that of the output laser contains specific information about the composition of the target region. The detected radiation may be shifted or be broadened by inelastic scattering processes, such as vibrational or rotational Raman scattering. Measurements of atmospheric parameters, including the composition, structure

properties, and dynamic behavior of the atmosphere, have been demonstrated using lidar techniques developed during the past twenty years. In the future, lidar systems will play a key role in providing the basic information for our understanding of the meteorology, measurement of atmospheric properties, and data for long-term as well as short-term forecasting of weather.

1.2 Historical Review of Laser Remote Sensing

The idea of using light scattering by molecules to monitor atmospheric properties was demonstrated earlier than the invention of the laser. A searchlight method to measure scattering by the atmosphere was used to provide molecular density and temperature profiles from *10 to 61.8 km*. [Elterman, 1951]. The first reported use of lasers in atmospheric studies was Fiocco and Simullin's [1963] effort. They used a *0.5 J* ruby laser radar at a wavelength of *694 nm* to detect atmospheric molecular scattering echoes at heights near *60 km*. They also claimed to detect weak echoes, which they ascribed to dust clouds at high altitudes. About the same time, Ligda [1963] had initiated a program at Stanford Research Institute where a similar pulsed ruby laser radar system, or *Lidar* as Ligda called it, was used to probe the lower atmosphere and to study meteorological phenomena. Barrett and Ben-dov [1967] used a lidar to measure vertical profiles of lower atmospheric particle concentration and size distribution up to *1.5 km*. They showed the applicability of the lidar for air pollution measurements. Collis [1969] proposed some appropriate areas for lidar research such as the structure of dust layers in the upper atmosphere (*20 to 150 km*) and noctilucent cloud studies, atmospheric density (*50 to 80 km*), wave motion and turbulent air flow, boundary layer structure, turbulent mixing and diffusion processes, etc. Hamilton [1969] used a lidar to study the behavior of power station chimney smoke, such as the rise and growth of a plume. Strauch and Cohen [1972] described the capabilities of the lidar and directions for the future of atmospheric research. Comprehensive reviews of lidar measurements of the

atmosphere can be found in papers given by Derr and Little [1970], McCormick [1975], Killinger and Menyuk [1987], and in books by Hinkley [1976], Zeuv [1982], Measures [1992], and by Camagni and Sandroni [1984]. Grant [1991] reviewed the use of differential absorption lidar (DIAL) and Raman lidar for water vapor profile measurements. Carswell [1990] presented an overview of current lidar applications for aerosol measurements, and discussed the advantages and limitations of lidar. Other applications that he suggested include ceilometry, visibility measurements, wind profile measurements, and atmospheric pollutant tracking.

Laser remote sensing techniques include molecular scattering, particle (aerosol) scattering, Raman scattering, resonance scattering, fluorescence, absorption, differential absorption (DIAL) and differential scattering (DISC). Molecular scattering, particle/aerosol scattering, and Raman scattering are the techniques important to this research work and only these will be discussed in any depth, the other techniques will be briefly introduced.

Resonant scattering occurs from atomic species deposited by meteoric dust at altitudes between 80 and 100 km. Observations of the 90 km-altitude layer of atomic sodium by laser backscattering were published in the early 70s [Sandford and Gibson 1970, Gibson and Sandford 1971; Blamont *et al.* 1972]. Species such as sodium, calcium, iron, potassium and lithium, which are present in the mesopause region from meteoric dust, have been detected by lidar [Megie *et al.*, 1978a, b]. Several lidar groups have made observations of a phenomenon that has been called sudden sodium layers [von Zahn, *et al.* 1987, 1988], or sporadic sodium layers [Kwon *et al.*, 1988]. Resonance scattering lidars have contributed much to the study of gravity wave activity by using sodium as a tracer of wave motion [Beatty and Gardner, 1990].

Fluorescence is the spontaneous emission of a photon, following the excitation of an atom to a higher energy state. The atom is excited by absorbing incident radiation at a frequency, ν_0 , corresponding to a specific absorption line or band of the atom. Due to the large resonance

scattering cross-section, on the order of $10^{-17} \text{ m}^2/\text{sr}$ compared to $10^{-31} \text{ m}^2/\text{sr}$ for molecular scattering, fluorescent transitions are useful in identifying and measuring profiles of the low concentration atoms. The resonance scattering species can be particularly useful as passive tracers to measure the mesospheric dynamics, such as the sodium layer region [Derr and Little, 1970; She *et al.*, 1990a, 1992]. The resonance fluorescent technique is limited to higher altitudes where the collision frequency is sufficiently low to allow several fluorescent lifetimes for the emission to occur before the energy is quenched by collisional processes.

The DIAL system uses two emitted wavelengths, one tuned to a molecular or atomic absorption line and one tuned to a nearby non-absorbed wavelength. The concentration of the absorbing species is deduced from comparison of these two lidar signals. This technique was pioneered by Schotland [1966] who called it Differential Absorption of Scattered Energy (DASE) and used it to remotely determine the water vapor content of an atmosphere volume. By selecting appropriate wavelengths for absorption and background measurements, differential absorption measurements can determine the concentration of atmospheric pollutant gases, or natural atmospheric constituents such as water vapor. Korb and Weng [1982] made a theoretical study of a differential absorption lidar technique for measuring the atmospheric temperature profile by using a high J line in the oxygen A band, between 760 and 770 nm. The DIAL technique has also been used for the detection of the stratospheric ozone layer [Uchino *et al.*, 1978; McDermid *et al.*, 1990]. Papayannis *et al.* [1990] used a UV DIAL system for ground-based and airborne ozone measurements in the troposphere and the lower stratosphere both for daytime and nighttime operation. Browell [1991] used two frequency-doubled Nd:YAG lasers to pump two high-conversion-efficiency tunable dye lasers with frequency doublers for airborne lidar measurements of ozone and aerosols over the Arctic troposphere and stratosphere.

A brief schematic representation of each lidar technique is included in Figure 1.1, which

Lidar Technique

Schematic and Physical Description

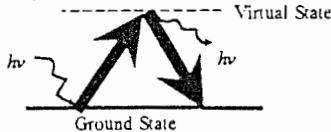
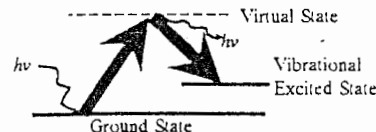

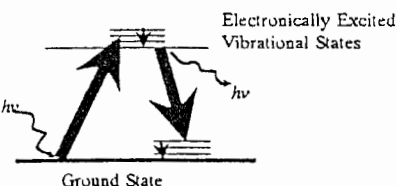
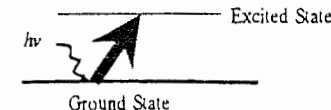
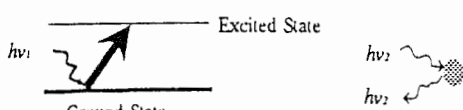
Rayleigh/Particle Scattering	Elastic Scattering : laser radiation scattered from atoms, molecules, or particles with no change of frequency.	 <p>The diagram shows a horizontal line for the Ground State and a dashed line for the Virtual State. An upward arrow labeled $h\nu$ starts from the Ground State and ends at the Virtual State. A downward arrow labeled $h\nu$ starts from the Virtual State and ends at the Ground State.</p>
Raman Scattering	Inelastic Scattering : laser radiation scattered from molecules with a frequency shift characteristic of the molecule.	 <p>The diagram shows a horizontal line for the Ground State, a dashed line for the Virtual State, and a solid line for the Vibrational Excited State. An upward arrow labeled $h\nu$ starts from the Ground State and ends at the Virtual State. A downward arrow labeled $h\nu$ starts from the Virtual State and ends at the Vibrational Excited State.</p>
Resonance Scattering	Laser radiation matched in frequency to that of a specific atomic transition is scattered by a large cross section and observed with no change of frequency.	 <p>The diagram shows a horizontal line for the Ground State and a solid line for the Excited State. An upward arrow labeled $h\nu$ starts from the Ground State and ends at the Excited State. A downward arrow labeled $h\nu$ starts from the Excited State and ends at the Ground State.</p>
Fluorescence	Laser radiation matched to a specific electronic transition of atom or molecule suffers absorption and subsequent emission at lower frequency.	 <p>The diagram shows a horizontal line for the Ground State and a higher solid line for Electronically Excited Vibrational States. An upward arrow labeled $h\nu$ starts from the Ground State and ends at the Electronically Excited Vibrational States. A downward arrow labeled $h\nu$ starts from the Electronically Excited Vibrational States and ends at a lower energy level.</p>
Absorption	Laser beam attenuated when frequency matched to the absorption band of given molecule.	 <p>The diagram shows a horizontal line for the Ground State and a solid line for the Excited State. An upward arrow labeled $h\nu$ starts from the Ground State and ends at the Excited State.</p>
Differential Absorption	The differential attenuation of two laser beams is and Scattering (DIAL) evaluated from backscattered signals when the frequency of one beam is closely matched to a given molecular transition while the other's is somewhat detuned from the transition.	 <p>The diagram shows a horizontal line for the Ground State and a solid line for the Excited State. An upward arrow labeled $h\nu_1$ starts from the Ground State and ends at the Excited State. A second upward arrow labeled $h\nu_2$ starts from the Ground State and ends at a point below the Excited State line, representing a detuned transition.</p>

Figure 1.1. Schematic and physical description of various lidar remote sensing techniques (after Measures, 1992).

is adapted from Measures [1992]. Table I lists the different kinds of lidar optical interaction processes, with an indication of the approximate scattering cross-section and the applications for each process.

In the elastic scattering (molecular or particle scattering) lidar techniques, the detected wavelength is the same as the laser output wavelength, except for any Doppler broadening due to the random motion of the scatterers. The backscattered radiation is collected by a telescope and detected by a photomultiplier tube or some other detector. The detected signal is recorded as a function of time to provide a range-resolved measurement of atmospheric scattering. Analysis procedures are applied to the recorded data to provide a measurement of the scattering particles' (atoms, molecules, or dust particles) vertical density distribution in the atmosphere, or to describe atmospheric optical properties (optical depth, extinction coefficient, transmittance etc.).

Elastic backscattering of a laser beam by atmospheric molecules has been widely used to measure density and temperature in the middle atmosphere [Philbrick *et al.*, 1987; Metzger and Gardner, 1989; Hauchecorne *et al.*, 1992]. The Rayleigh technique using high power lasers in the 30 to 80 km region was pioneered by Kent *et al.* [1971], and later was developed by Chanin and Hauchecorne [1981]. Rayleigh lidars have been used to observe gravity waves and tidal waves [Chanin and Hauchecorne, 1981; Philbrick *et al.*, 1987; Wilson *et al.*, 1990], semidiurnal and diurnal tidal effects [Gille, 1991], planetary waves [Philbrick and Chen, 1992], climatology trends [Hauchecorne, 1991], and the middle atmosphere response to solar rotation [Keckhut and Chanin, 1992]. Miller *et al.* [1987] observed monochromatic gravity wave events and estimated the critical wave parameters in a collaborative study, using the mobile Rayleigh scatter lidar, GLINT, when it was operated at Poker Flat, Alaska [Philbrick *et al.*, 1987].

Lidar provides a useful instrument for observing stratospheric dust layers. McCormick *et al.* [1978] used a Q-switched ruby ($\lambda = 694.3 \text{ nm}$) lidar to observe variations of volcanic

Table I**Comparison of Optical Interaction Processes Applicable to Laser Remote Sensing Methods in the Atmosphere**

Interaction Process	Frequency Relation	Cross-Section (m ²)	Scattering Species	Applications
Elastic Scattering - Molecular (Rayleigh Cabannes lines)	$\nu_r = \nu_o$	$\sim 10^{-31}$	Atoms and Molecules	High Altitude Density
- Particle	$\nu_r = \nu_o$	$\sim 10^{-31}$ ↓ $\sim 10^{-13}$	Aerosols, Droplets	Air Pollution, Atmospheric structures and motions, Cloud and Fog Studies
Inelastic Scattering - Raman - Rayleigh rotational lines	$\nu_r \neq \nu_o$	$\sim 10^{-34}$	Molecules identified by ν_r	N ₂ , O ₂ , Plume Pollutants, Boundary Layer H ₂ O, Temperature
Fluorescence Emission	$\nu_r \neq \nu_o$	$\sim 10^{-28}$	Molecules identified by ν_r	Minor species and pollutants
Resonance Scattering	$\nu_r = \nu_o$	$\sim 10^{-17}$ ↓ $\sim 10^{-21}$	Atoms identified by ν_o	High altitude atomic species (Na, K, Li ..)
Differential Absorption (DIAL)	ν_{on}, ν_{off}	$\sim 10^{-23}$	Molecules identified by λ_{on}	Low density or long range minor species; for example: stratospheric ozone

ν_r : Detection frequency; ν_o : Laser frequency.

ν_{on}, ν_{off} : Frequency at molecule absorption line and adjacent it. [Hinkley, 1976; Camagni and Sandroin, 1984]

stratospheric particles during October 1974 to July 1976 after the eruption of the Volcán de Fuego in Northern America. They also used airborne and ground-based lidars to measure the El Chich'on stratospheric aerosols from $90^{\circ}N$ to $56^{\circ}S$ [McCormick *et al.*, 1984]. Iwasaka and Isono [1977] used a two-wavelength, 694.3 nm and 1060 nm , lidar to observe stratospheric aerosols. From mid-June to September 1980, Lefrere *et al.* [1981] operated a lidar with a wavelength of 532 nm to measure aerosol layers following the volcanic eruption of Mt. St. Helens (18-25 May 1980). Sacco *et al.* [1989] used an elastic backscattering lidar to collect data on cloud distribution, motion, and aerosol concentration of Polar Stratospheric Clouds (PSCs), which play an important role in ozone hole events. Uchino and Tabata [1991] developed a mobile lidar, which consists of a XeCl laser and a Nd:YAG laser, for simultaneous measurements of stratospheric aerosols, ozone and temperature. Ferrare *et al.* [1992] and Gobbi *et al.* [1992] reported lidar observations of the early stratospheric effects of the Pinatubo eruption.

Derr and Little [1970] obtained wind velocity measurements by tracking scattering inhomogeneities in the atmosphere, calculating the distance traveled, and inferring the velocity. Kolev *et al.* [1988] used two lidars, a ruby lidar operating at selected elevation angles and directions and a Nd:YAG lidar operating vertically, to obtain wind velocity from the advection of aerosol inhomogeneities in the planetary boundary layer. Several groups have demonstrated the wind measurements capability by using the coherent scattered Doppler techniques known as Laser Doppler Velocimeters [Bilbro 1980; Hardesty, 1991]. The wind velocity is measured through the Doppler frequency shift of the backscattered laser beam resulting from the relative motion between the lidar and the scattering particles. Schwiesow and Cupp [1976] measured atmospheric dust devil vortices by using a Doppler velocimeter. Chanin *et al.* [1989] used Fabry-Perot interferometers to measure the Doppler shift of incoherent backscatter. They directly detected Doppler shift by measuring the wavelength on either side of the emitted laser line, and

compared the intensities to decide wind velocity. Abreu *et al.* [1980] used a multi-channel Fabry-Perot detector as a receiver for a Doppler lidar wind measurement. This detector includes a high-resolution, optically contacted plane etalon and a multi-ring anode detector to spatially scan the image plane of the Fabry-Perot.

Usually, the measured aerosol lidar signal intensity is due to a superposition of many different particle sizes. In the middle atmosphere, 30 to 100 km, scattering is dominated by molecules under normal conditions. In the boundary layer, 0 to 2 km, scattering is dominated by a mixture of particles with different sizes. While in the region from 2 to 30 km, the back-scattering signals are from a mix of both molecules and particles with a wide range of relative amounts.

In the middle atmosphere, 30 to 100 km, where molecular scattering is the dominant process, atmospheric density and temperature can be determined from backscatter signals directly. By comparing visible and ultraviolet lidar profiles, Philbrick *et al.* [1987] showed that it is possible to resolve the question of what altitude regions are properly analyzed as pure molecular scatter signal, thus defining those regions where density and temperature can be directly determined.

With more sophisticated instrumentation it is possible to detect characteristic shifts at specific wavelengths due to inelastic scattering, such as Raman scattering, where the radiation is detected at wavelengths shifted significantly from that of the laser. This shift uniquely determines the molecular gas composition of the scattering volume. The first observation of this secondary radiation was by Raman and Krishnan [1928] and Raman [1928]. Raman used a blue-violet filter for a beam of sunlight. As a filtered sun beam passed through a liquid or dust-free vapor, the wavelength shift phenomenon was observed by eye and confirmed by spectroscope. The fact is that molecules scatter small fractions of the incident electromagnetic radiation at specific shifted

wavelengths which are associated with the vibrational energy levels of molecules. The magnitude of the frequency shift is unique to the species of the scattering molecule and the intensity is proportional to the concentration, modified only by atmospheric transmission losses.

The potential of Raman lidar in pollutant detection has been studied theoretically and experimentally for more than two decades [Kobayasi and Inaba, 1969]. Leonard [1967] first reported observations of Raman vibrational scattering by nitrogen and oxygen in the atmosphere, and measured nitrogen Raman scattering to determine atmospheric transmission as a function of range [Leonard and Caputo, 1974]. Cooney [1968] and Cooney *et al.* [1969] presented lidar observations of Raman vibration-rotation scattering by nitrogen, ozone [Cooney, 1986, 1987], and water vapor [Cooney, 1970, 1990]. Cooney [1970] reported the first Raman lidar for water vapor profiling up to 2.5 km by using a high power laser to monitor the Raman shifted component (to the first Stokes line) of water vapor in the laser backscatter signals. Later he used a differentiating technique to extend the use of Raman lidar atmospheric measurements into the daytime [Cooney, 1973]. This technique uses the ratio of two wavelengths from different species which undergo Raman backscatter, for example H_2O / N_2 and O_2 / N_2 . Strauch *et al.* [1972] used Raman scattering signal from N_2 to measure atmospheric vertical temperature profiles and compared them with thermistor probes on a meteorological tower. Melfi [1972] reported the observation of nitrogen and water vapor Raman scattering; Melfi *et al.* [1969] and Melfi [1972]. Later, Melfi and Whiteman [1985] demonstrated the capability of interpreting the evolution of water vapor mixing ratio in both spatial and temporal resolution, and Melfi *et al.* [1989] have used Raman lidar to record the passage of frontal systems. Houston *et al.* [1986] designed a Raman lidar system, which used an excimer laser source to measure methane gas concentration at ranges from 100 m to 1 km. By monitoring both hydrocarbons and nitrogen, Bilbe *et al.* [1990] developed a mobile Raman lidar system to remotely measure natural gas released into the atmosphere.

Riebesell [1990] and Ansmann [1990, 1992] developed a combined Raman and elastic-backscatter lidar to profile atmospheric moisture, aerosol extinction, and lidar backscatter ratio.

A measurement of atmospheric temperature profiles using the backscattering signal from the pure Raman rotational spectrum from nitrogen also has been reported by Cooney [1972]. Arshinov *et al.* [1983] presented an atmospheric temperature measurements experiment by using a double grating monochromator in the lidar receiver. The purpose of this double grating monochromator is to isolate two portions of the pure rotational Raman spectrum of N_2 and O_2 and to suppress the line of aerosol light scattering. The relative intensity of the distribution Stokes and anti-Stokes rotational lines of the N_2 and O_2 Raman spectra are sensitive to temperature, and can give direct temperature measurements [Cooney, 1972; Hauchecorne *et al.*, 1992; Nedeljkovic *et al.*, 1993]. Renaut *et al.* [1980] and Cooney *et al.* [1985] developed daytime operation methods by using wavelengths in the solar-blind region of the spectrum below 300 nm.

The Raman, Rayleigh and two-wavelength lidar techniques have been proposed to measure atmospheric density from the troposphere to the upper mesosphere by Philbrick *et al.* [1987]. All these research activities show the capability for using Raman lidar to study the spatial and temporal evolution of water vapor in the lower atmosphere. With a two-wavelength lidar, it is possible to separate the regions of molecular scattering from the regions of particle scattering and to define the regions for analysis of molecular scattering signal with confidence [Philbrick *et al.*, 1987]. Using lidar inversion techniques similar to those proposed by Klett [1981, 1985], we can extract the atmospheric extinction coefficients from lidar signals at several different wavelengths. However, the required assumptions cause us to question the value of using Klett's approach. The N_2 Raman scattering provides the opportunity to directly measure atmospheric extinction, and then it is possible to describe what limits to place on extinction calculated from the Klett inversion. Based on the wavelength dependence of the particle scattering cross-section, it may be possible

to extract additional particle information from the backscattered signal by using two or more wavelengths simultaneously. Russell *et al.* [1982 a, b] simulated aerosol and cloud signals by an wavelength-independent technique and a wavelength-combining technique (1064 nm , 532 nm , and 355 nm) for density, temperature, aerosol, and cloud properties. Zuev [1982] presented the inverse problem of determining the atmospheric aerosol backscattering coefficient and number density profile with a multi-wavelength lidar, using six to eight different wavelengths to probe the atmosphere. Potter [1987] used a two-frequency lidar to calculate the total transmittance, the ratio of the extinction coefficients, and the extinction profiles at two frequencies. Sasano and Browell [1989] presented a multiple wavelength lidar technique, 355 nm , 532 nm and 1064 nm , which discriminates between several aerosol types such as maritime, continental, stratospheric, and desert aerosols based on wavelength dependence of the aerosol backscattering coefficient. Papayannis *et al.* [1990] discussed using either molecular and particle signals or the Raman nitrogen signal of a multi-wavelength lidar system to correct ozone measurements which were contaminated with scattering from particles or other gas molecules (i.e., SO_2) in the lower troposphere.

The high spectral resolution lidar (HRSL) technique is based on high resolution spectral analysis. Molecules and particles both contribute to the backscattered signal spectrum of lidar measurement. The velocities associated with random motions of the particles are much smaller than the thermal velocities of the atmospheric gases, and scattered energy is concentrated in a narrower band of frequencies, assuming that an injection seeded laser is used to generate a narrow line. Fiocco and DeWolf [1968] and Fiocco [1971] demonstrated that the spectral distribution of initially monochromatic light backscattered by the atmosphere consists of a narrow-band aerosol signal superimposed upon a Doppler broadened signal due to backscattering by molecules. By resolving the spectrum, it is possible to distinguish the contribution of the particles from that of the molecules. The high spectral resolution lidar (HRSL) has been developed to measure the

spatial distribution of aerosol optical properties and wind motion by Shipley *et al.* [1983], Sörga *et al.* [1983], Grund and Eloranta [1991] and Eloranta [1987] at the University of Wisconsin. The HRSL lidar measures scattering properties by separating laser light elastically backscattered by atmospheric particles from that which is Doppler broadened in the thermal motion of the molecules. The spectral separation is achieved by using a high spectral resolution Fabry-Perot optical interferometer. She *et al.* [1990, 1991, 1992] used a high spectral resolution fluorescence lidar to measure the temperature in the mesospheric sodium layer, and gravity wave perturbations in the mesopause region, by detecting the line-shape function of Doppler-broadened fluorescence spectra of $Na D_2$ transitions.

1.3 Lidar System Configurations

There are two basic arrangements for laser remote sensing, the bistatic system and the monostatic system [Measures, 1990]. The distinction depends upon whether the optical axes of the transmitter and the receiver are parallel to each other. The Penn State LAMP (Laser Atmospheric Measurements Program) lidar is a monostatic coaxial lidar. A basic lidar system consists of five subsystems: transmitter, receiver, detector, data processing and storing unit, and safety system. The laser transmitter and receiving mirror of a biaxial monostatic lidar are shown in Figure 1.2. Here, their optical axes are separated by a small distance as compared with the altitude range R . The receiver's field-of-view, Ω_r , is at least as large or larger than the transmitter's divergence solid angle, Ω_t . Thus above some overlap altitude, the receiver will receive backscattered photons from the entire gated volume of atmosphere which is illuminated by the laser beam. Typically the receiver's field-of-view is made a factor of two to five times the angular beam spread. The subsystems and arrangement of the remote sensing lidar used at Penn State is schematically shown in Figure 1.3.

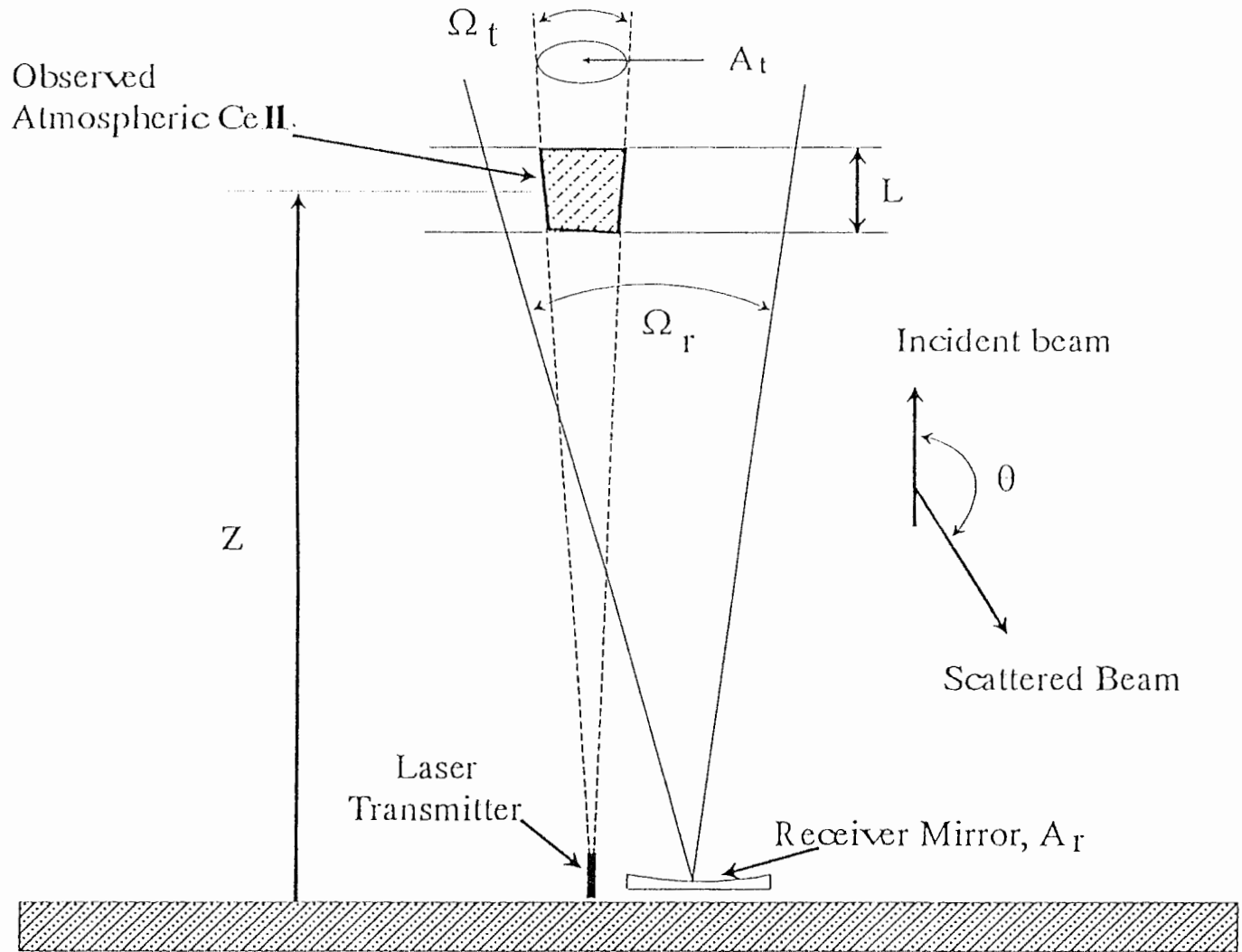


Figure 1.2 The configuration of biaxial monostatic lidar transmitter and receiver.

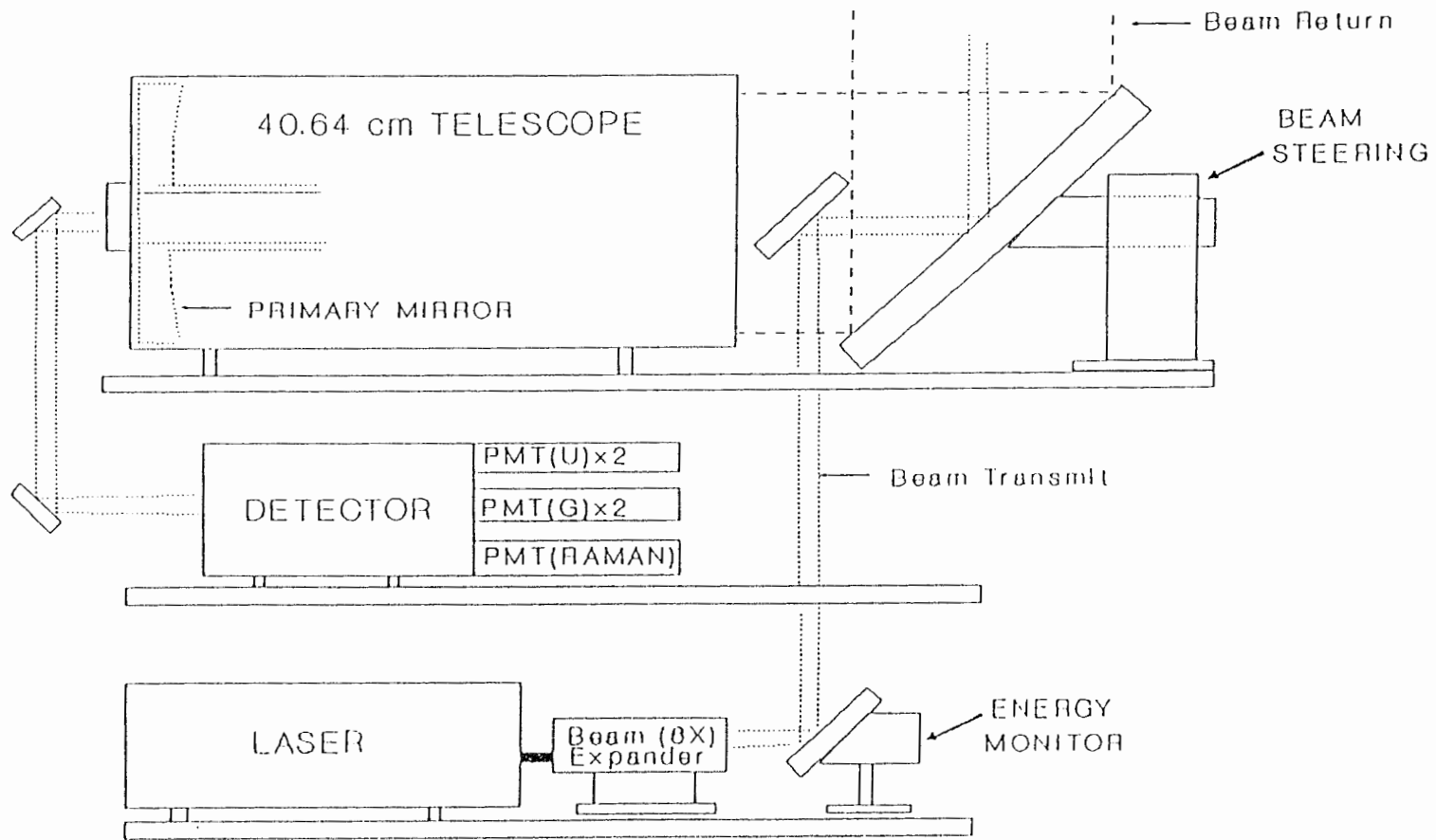


Figure 1.3 The operational diagram of transmitter, receiver, and detector of The Penn State LAMP lidar system (coaxial monostatic type).

1.3.1 Transmitter

The transmitter consists of an intense laser pulse source, a beam expansion telescope, and beam steering output optics. A high-power laser is necessary for ground-based high-altitude atmospheric measurements and for minor species Raman scattering measurements. Special attention has to be paid to the choice of the laser wavelength to have a detectable signal for lidar measurements and to avoid atmospheric absorption lines. Beam steering optics direct the laser beam to the atmospheric region of interest and maintain alignment with the receiver axis. A beam expander is used to reduce the divergence angle of the laser beam and an energy monitor is used to monitor the output laser energy. The laser source used in the Penn State LAMP Lidar is a Nd:YAG pulsed laser with a fundamental wavelength at 1064 nm , and with second and third harmonic generators to provide outputs at 532 nm and 355 nm , respectively. Parameters of the Penn State LAMP lidar transmitter are given in Table II. The variations of atmospheric transmittance, which were calculated from Lowtran7 [Kneizys et al. 1988] for a tropical maritime atmospheric model from the surface to 100 km altitude for these three laser wavelengths, are illustrated in Figure 1.4.

1.3.2 Receiver and Detector

The receiving telescope collects the return signal from the atmospheric region illuminated by the laser. The telescope used in the Penn State LAMP Lidar is an $f/15$, 40.64 cm classical Cassegrain system with an effective focal length of 609.6 cm . The Cassegrain telescope has the advantages of both compact design and long focal length. The field of view of this telescope is 1.6 mrad , which is three times the 0.45 mrad beam divergence of the unexpanded laser beam. This wide field of view can be reduced with a field stop to limit the sky background during daytime measurements.

Table II. Transmitter Parameters

Type	Continuum NY-82, Seeded Nd:YAG
Operational Wavelength	<i>1064 nm</i> <i>532 nm (18797 cm⁻¹)</i> <i>355 nm (28169 cm⁻¹)</i>
Pulse Energy	<i>1.5 J @ 1064 nm</i> <i>600 mJ @ 532 nm</i> <i>200 mJ @ 355 nm</i>
Pulse Rate	<i>20 Hz</i>
Pulse Width	<i>6 ns</i>
Pulse Length	<i>80 MHz</i>
Beam Divergence	<i>0.45 mrad</i> <i>0.09 mrad (with beam expander)</i>

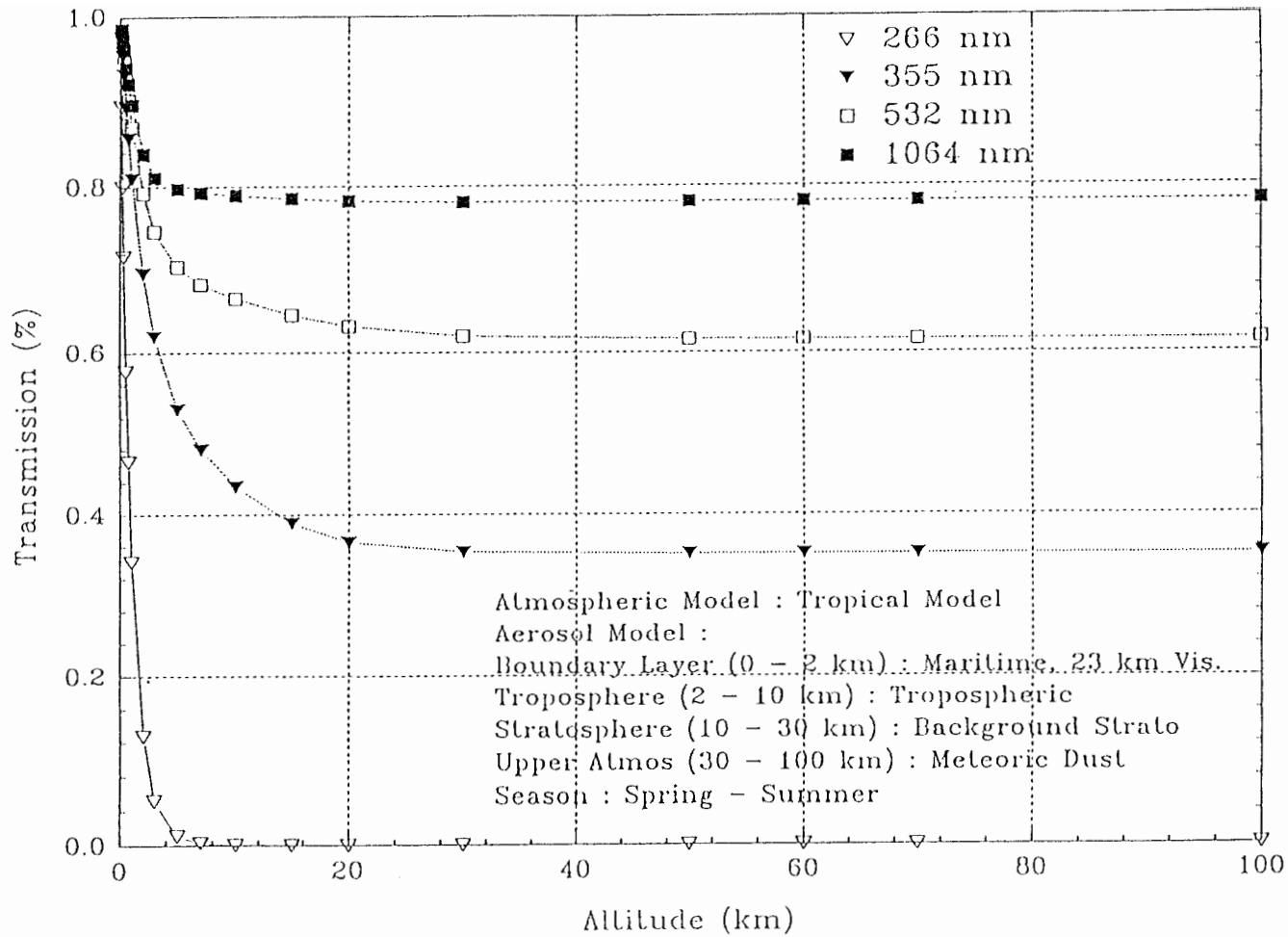


Figure 1.4 Atmospheric transmittance variation with altitude from surface to 100 km for the 23 km visibility coastal model (Calculated from Lowtran 7).

The optical signal collected by the telescope passes through a series of optical elements, including a collimating lens, Fabry lens, interference filters, and dichroic mirrors (beam splitter). The detected signal finally reaches the photomultiplier tube (PMT), which is a high-gain photon counting detector that is most efficient at visible and UV wavelengths ($\lambda \approx 200$ to 700 nm). Photomultiplier performance is determined by (1) the spectral response of its photocathode, (2) the dark-current characteristics of its photocathode, (3) the gain of the dynode chain, (4) time spreading effects of the electrons between the first dynode and the anode, (5) signal induced noise, especially at low photon level [Hunt and Poultnery, 1975; Measures, 1992], and (6) the transmission of the PMT windows, where the photocathode is usually deposited. Pettifer [1975] and Pettifer and Healey [1974] have reported a memory effect in photomultiplier tubes that has been termed "signal-induced noise". This effect is most noticeable after the complete termination of an exciting light flux when the tube output, expressed as an anode pulse count rate, does not immediately drop to the expected background value but decays toward the limiting value over a period of tens or hundreds of micro-seconds. A cool environment both during operation and storage can be very helpful for improving the performance of some of the high performance tubes by minimizing the dark current background [Evans, 1978].

The Penn State LAMP lidar system has two PMTs for the ultraviolet (355 nm) detection and two PMTs for the green (532 nm) detection. Both channels use one PMT for lower altitude (ground to 20 km) measurement and the other one for the higher (above 15 km) altitude measurement. Other PMTs are used for the detection of N_2 Raman scattering at 607 nm and for the detection of H_2O at 660 nm. The receiver optical parameters are listed in Table III.

1.3.3 Data Processing and Storage Unit

The data processing unit is used to acquire the electrical signals from the photomultiplier

Table III. Receiver Parameters

Type	Dall-Kirkham
<u>Diameter</u>	
Primary lens	40.64 cm (16 in)
Secondary lens	10.16 cm (4 in)
Field-of-View	1.5 mrad
Focal Length	609.6 cm (240 in)
F/#	F/15
<u>Photomultipliers</u>	
Quantum Efficiency	$\approx 24\%$ @ 355 nm $\approx 14\%$ @ 532 nm

or PMT tubes. A CAMAC data acquisition module with 0.5 microsecond range bins (75 meter resolution) is used to detect and integrate the photon counts. The electrical signals from the PMT are averaged and stored for one-minute intervals and accumulated after 30 files, then recorded to optical disks for later analysis. A personal computer and a high-volume (1 Gbyte) optical disk are integrated with the CAMAC module for the data storage and analysis. The background noise is also measured separately and stored for the analysis of error.

1.4 Statement of the Problem

Lidar remote sensing has the potential to provide measurements of atmospheric properties (pressure, density, and temperature) over the altitude region from the ground to 100 km, but accurate measurements using lidar techniques have been generally limited because of the presence of particles in the atmosphere. Below 30 km, stratospheric and tropospheric particles and clouds contaminate the molecular signal of the lidar profile, making it difficult to obtain an accurate measurements of atmospheric properties. The primary purpose of this study is to investigate to what degree the particle scattering signal can be separated from the molecular scattering signal by using a combination of two-wavelength and vibrational Raman lidar techniques. The goal is to obtain atmospheric density and temperature profiles in the mesosphere, stratosphere, and troposphere. Specifically, this study applies analysis and inversion techniques developed by other investigators, it shows the limitations of those techniques, and it proposes new approaches for current lidar measurements. The study applies techniques using the improved information from a two-wavelength lidar combined with vibrational Raman measurements. The study also presents the advantages and limitations of the two-wavelength Rayleigh/Raman lidar technique. The goal is to show how well the atmospheric structure properties can be described in the background of a turbid atmosphere using these approaches.

The vertical distributions of density and temperature of the U.S. Standard Atmosphere, 1976 [USSA76, 1976], from ground to *80 km*, are shown in Figure 1.5, with the different lidar techniques indicated in proposed applicable regions. The model profile represents typical conditions at middle latitudes. At any given level up to *80 km*, atmospheric density and temperature measurements are usually within *30%* of the corresponding standard atmosphere values as would be expected based on our knowledge of atmospheric variability. The backscattered signals from altitudes below *30 km* have both molecular and aerosol contributions in unknown proportions. The Raman vibrational backscattering intensity, from nitrogen or other molecules, is proportional only to the density of that specific molecule. The single wavelength Rayleigh backscatter profile is not sufficient to determine atmospheric density profiles at altitudes below *30 km* because of the strong particle scattering effects. By using a lidar with two or more different wavelengths, it is possible to discriminate, to some degree, between molecular and particle scattering and to describe where changes occur in the particle profile based on the different particles' wavelength dependence. By using both the frequency-shifted vibrational Raman signals and the unshifted atmospheric components of the signal, we want to examine our ability to separate the signal due to molecular constituents from that due to particle constituents of the atmosphere.

Lidar atmospheric measurements obtained above *30 km* can be directly converted to atmospheric temperature and density profiles used to study the dynamics of the middle atmosphere. The results of this investigation together with several prior measurements [Philbrick, 1992] have shown good agreement with meteorological rocket measurements in the stratosphere and mesosphere. For altitudes below *30 km*, where molecules and particles are mixed, a special approach must be taken for the measurements of atmospheric density and temperature. Using the two-wavelength lidar, I have investigated the degree to which the aerosol and molecular

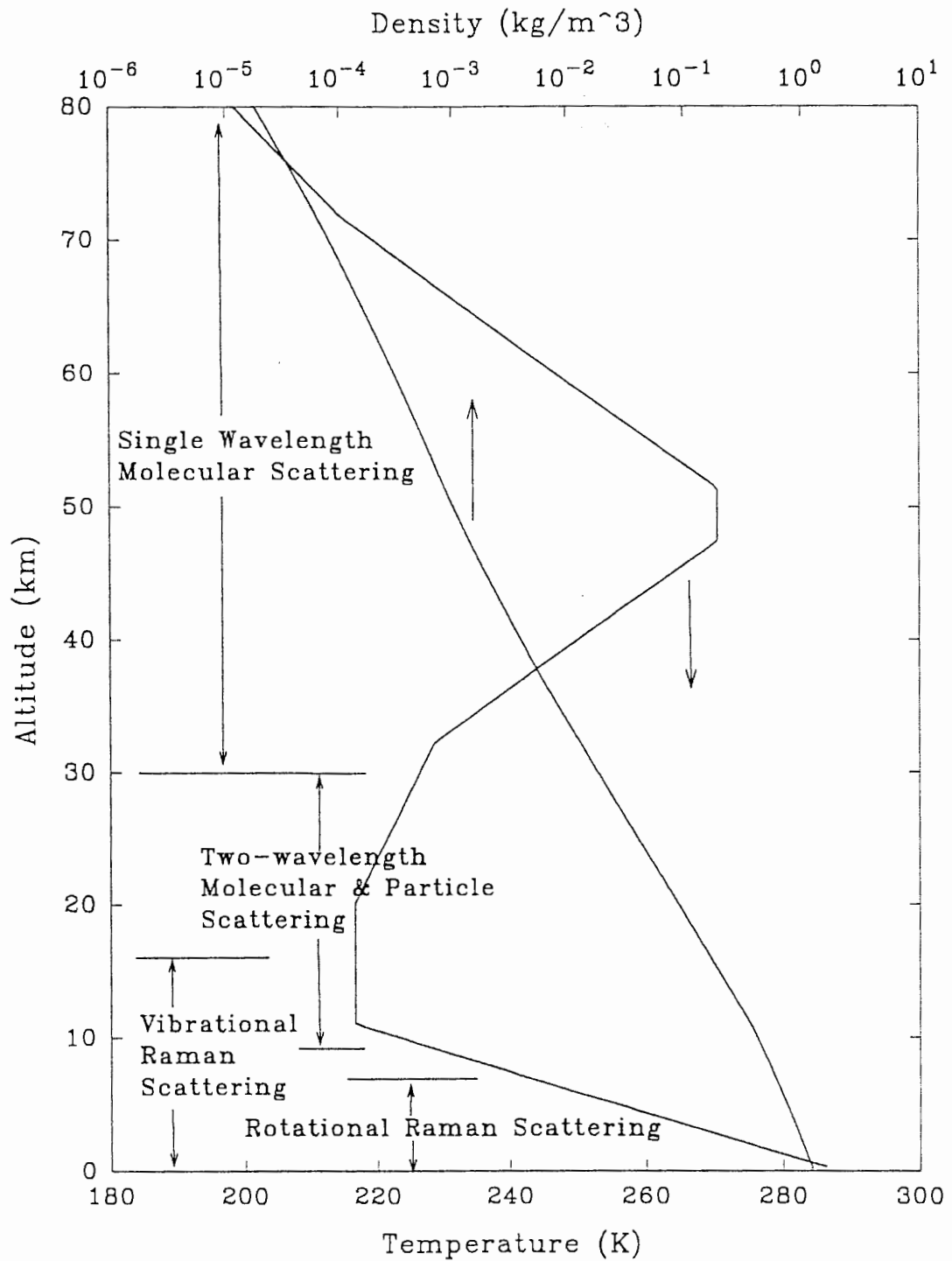


Figure 1.5 Atmospheric density and temperature profiles from U.S. Standard Atmosphere, 1976, with applicable lidar technique regions.

backscatter signals can be separated. This signal separation approach is expected to be useful in the range from 10 to 30 km. In the altitude range from the top of the boundary layer (0 to 2 km) to 10 km, the Raman-Rayleigh lidar is expected to be useful in obtaining the molecular backscatter signal. The goals of this study are to investigate and demonstrate the lidar capability for measurements of the lower atmospheric density and temperature to define their measurement accuracy, and ideally, to achieve an error of less than one percent for density and less than two degrees for temperature.

1.5 Thesis Organization

The work presented in this thesis is based on data obtained by the NSF CEDAR Sodium/Rayleigh lidar at Arecibo during the three-month period of the AIDA 1989 Campaign, and from the Penn State LAMP (Laser Atmospheric Measurement Program) lidar during a three-month period in late 1991 of the LADIMAS (LAtitudinal Distribution Middle Atmospheric Structure) Campaign on board the German research ship *RV POLARSTERN*. Chapter 2 describes the data processing and analysis aspects of the Rayleigh lidar measurements of the AIDA 1989 Campaign. In Chapter 3, the wavelength dependence of the particle backscattering coefficient, which can be used to separate the molecular and particle backscattering signals of the stratosphere for the two-wavelength (532 and 355 nm) lidar, and the two-wavelength lidar atmospheric measurements are discussed. The lower atmospheric measurements using the Raman-Rayleigh lidar techniques are discussed in Chapter 4, and the Raman lidar density and temperature calculations are presented. Finally, in Chapter 5, the conclusions and suggestions of areas for future work are presented.

Chapter 2

MOLECULAR SCATTERING LIDAR DATA ANALYSIS

The molecular (Rayleigh) scattering process allows the probing of atmospheric properties in some regions of the atmosphere. During the AIDA (acronym for Arecibo Initiative in Dynamics of the Atmosphere) 1989 Campaign, a sodium resonance lidar system was operated by the University of Illinois at Arecibo Observatory, Puerto Rico. Besides the high-altitude sodium layer observations, this sodium resonance lidar also provided low-altitude Rayleigh lidar measurements. The sodium resonance lidar is designed to measure the concentration of sodium atoms and to monitor gravity wave activity near the mesopause. As an add-on experiment to the sodium lidar measurements, Penn State University investigators proposed to use the data to investigate the molecular backscattered signal at lower altitudes, which include the stratosphere and lower mesosphere. These data provided profiles of density and temperature over this region used to study atmospheric variations and to better understand middle atmospheric dynamics. The study of middle atmospheric dynamics, which has been discussed by Chanin [1981], Hauchecorne [1992] etc., is beyond the scope of this report. The lidar equation and the data analysis of AIDA Campaign results are presented in this chapter. The data processing and analysis of a PSU two-wavelength/Raman lidar (LAMP) will be considered in the following two chapters.

2.1 Molecular (Rayleigh) Scattering Lidar Equation

The lidar operating principle is based on the scattered radiation from a laser beam transmitted into the atmosphere. Measurements of backscattered radiation from molecules and particles are obtained by using a telescope to collect the backscattered radiation on detectors. The analyzed signals provide information on the density of scatterers and other properties of the scattering volume. In a pulsed monostatic lidar, the received elastic (molecular or particle) scatter

signal from an altitude interval, $c\tau/2$, at range, Z , can be calculated by using the lidar equation,

$$P_r(Z) = P_L \frac{A_r}{Z^2} \xi \beta(Z) \frac{c\tau}{2} e^{-2\int_0^Z \alpha(r) dr}, \quad (2.1)$$

where,

- P_r is the received backscatter power,
- P_L is the transmitted laser power,
- A_r is the effective receiver area,
- Z is the scattering volume altitude from the detector,
- ξ is the overlap factor of laser beam divergence and telescopic field of view,
- β is the volume backscatter coefficient of the atmosphere,
- c is the speed of light (3×10^8 m/s),
- τ is the laser pulse duration,
- α is the volume extinction coefficient of the atmosphere.

From this received power, P_r , the number of received photons, $N(Z)$, at each altitude interval, $c\tau/2$, at range Z can be calculated as,

$$N(Z) = \frac{P_r(Z)\lambda}{hc}, \quad (2.2)$$

where,

- λ is the emitted laser wavelength,
- h is the Plank constant (6.625×10^{-34} Js).

The measured photon number is stored in memory devices (floppy, tape, disk, or optic disk) as the raw data profile for further analysis of atmospheric density and temperature.

2.2 AIDA Campaign Data Analysis

The raw lidar signals, as detected photon counts, were checked to remove bad data records in the first phase of the data reduction. Since the returned photon signal is proportional to the atmospheric density in the region dominated by molecular scattering, the measured signal decreases exponentially with altitude. In addition, the detected range of the scattering volume is increased after each time step, thus introducing a Z^2 dependence, which reduces the signal intensity even more rapidly. An example of the logarithmic character of a mean night photocount profile on 5/6 April 1989 is shown in Figure 2.1. The sodium layer is shown in the altitude region from 80 to 110 km. A dip on the profile below 10 km is due to the detector gain switching. By checking the logarithmic character over a specified altitude range, from 20 to 40 km altitude, bad data records were eliminated from the data set.

Each raw data profile was composed of the integrated signals of many laser return shots during each specified data run period. For example, there were 6,000 laser shots during 28 seconds for the NSF AIDA lidar measurement. Before checking the correctness of return profiles, the records of the AIDA data set were checked to verify that each raw profile had integrated the correct number of shot returns (6,000). If it did not have exactly 6,000 integrated shots, we treated it as a bad record and deleted it from our data base.

Valid high-altitude records were selected using the altitude range from 20 to 40 km as our data checking region. For the AIDA data, five criteria were used to check the validity of the data profiles:

- (a) the approximate photocount number at 30 km,
- (b) the approximate magnitude of the background noise in the region between 76 and 79 km,
- (c) the intercept on the Y-axis of the line fitted to the log of the data versus altitude,

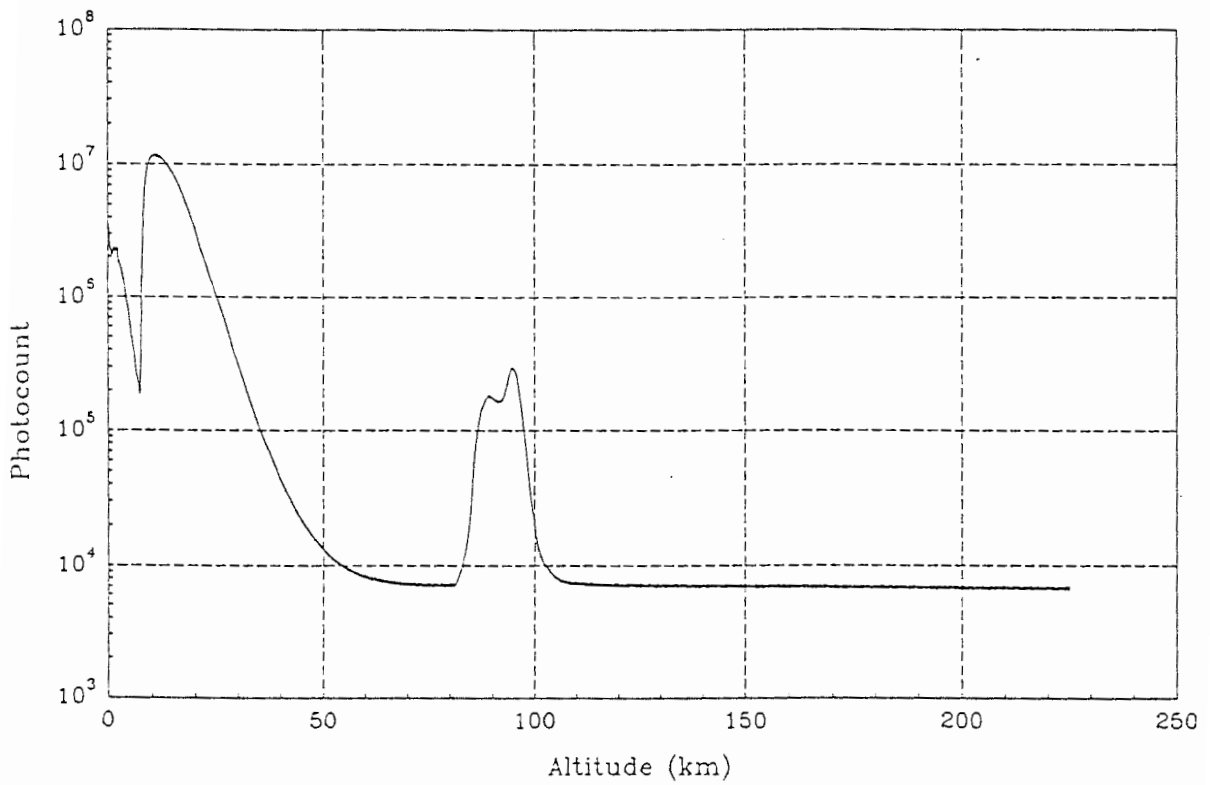


Figure 2.1 A whole night raw photocount profile has been constructed from sodium resonant lidar measurements taken on 5/6 April 1989. The sodium layer is shown in the altitude range from 80 to 110 km. The dip at 10 km is caused by detector gain switching.

- (d) the approximate value of the slope of this fitted curve,
- (e) the approximate magnitude of the standard deviation of the least square of the line fitted to the log of the data versus altitude.

First, the photon count of each record at 30 km was checked to verify that it remained within ± 2.5 standard deviations of the mean value obtained for the whole night. This altitude was chosen under the assumption that it is a particle-free region. Second, we took the average count between 76 km and 79 km , which was mostly the background noise signal, and examined it to see if it remained within ± 2.5 standard deviations of the whole night average, to verify that the background noise level did not change too much during the night. Third, a linear least-squares fit was made for the logarithm of the raw photocount versus altitude profiles between 20 km and 40 km . A nearly straight line relationship should exist for the logarithmic photon profile within this altitude range. An example of this raw photocount profile on a semi-log scale is shown in Figure 2.2.

The Y-axis (photocount) intersection points of different linear-least-squares-fitted profiles should group within ± 2.5 standard deviations of the whole night mean. In addition, the slope of each fitted line was checked to see whether it was within ± 2.5 standard deviations of the mean night slope. If any of these above criteria failed, we concluded that the profile was not valid and deleted it from the data set. The overall bad profiles, which were picked up by the above criteria during the AIDA Campaign '89, were less than one percent. As compared with procedure used by University of Illinois [Beatty, 1990], this test procedure faithfully picked out the bad records from the lidar analysis. Examples of some good and bad records are shown in Figure 2.3, where record number 1 is a good record, but examples number 2 and number 3 are bad data records.

After checking the whole night's data set and deleting the bad records, we examined the noise on the profiles. The photocount at each altitude bin should not be too much different from

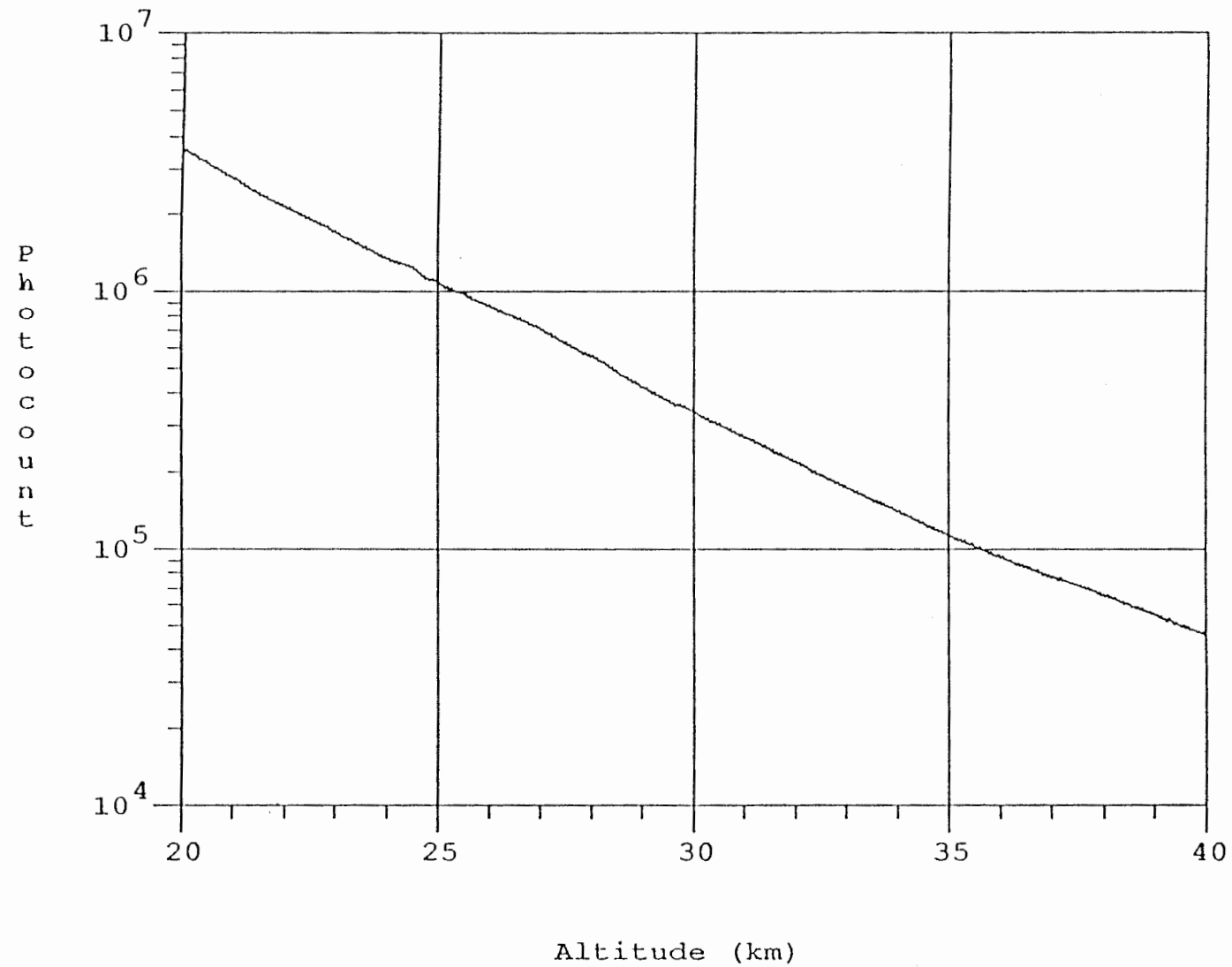
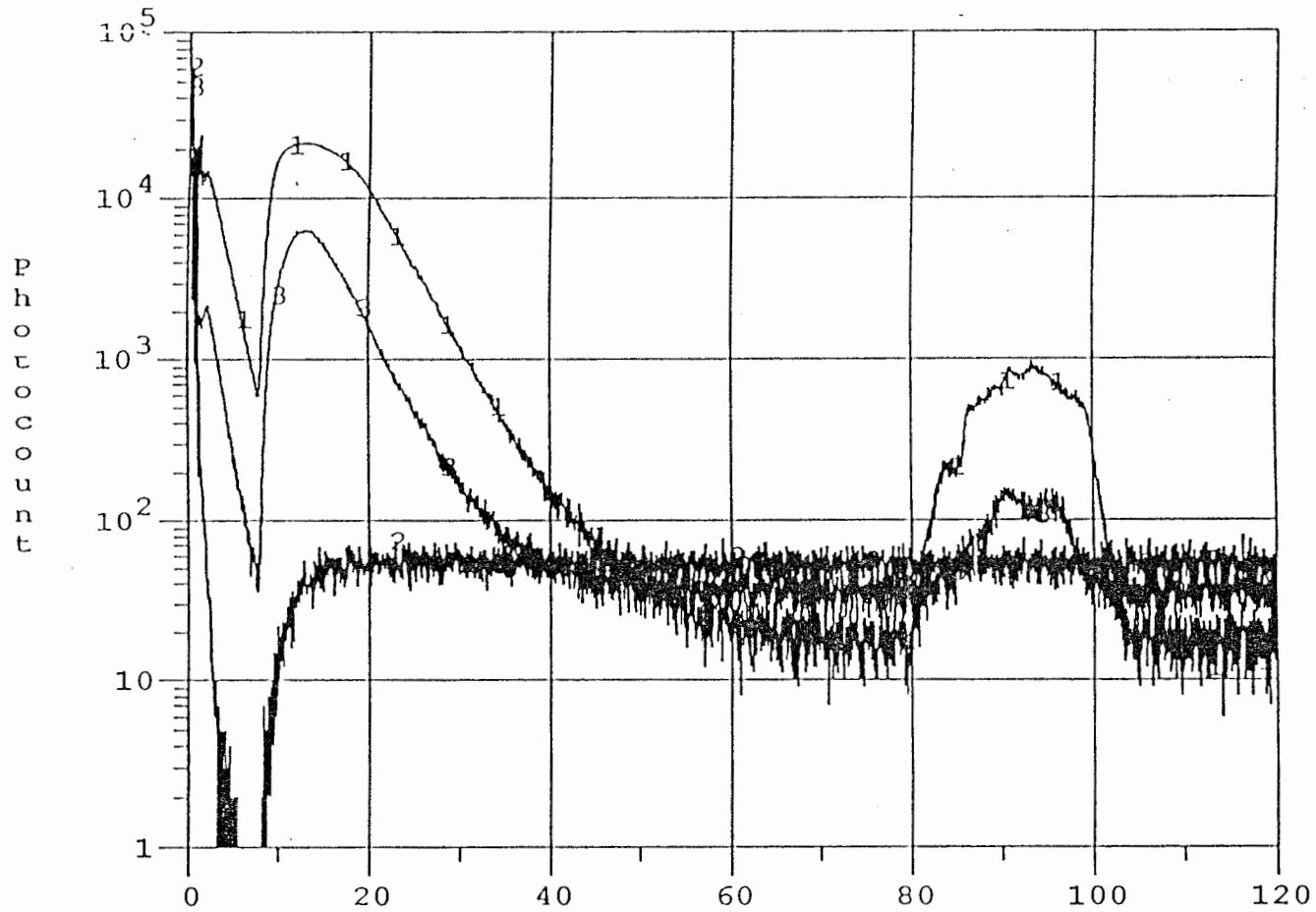


Figure 2.2. The data record checking region of photocount data profile taken on 5/6 April 1989, during AIDA Campaign.



Altitude (km); 1: record #1; 2: record #308; 3: record #370.

Figure 2.3. This figure juxtaposes examples of good and bad records taken on 25/26 March 1989, during the AIDA Campaign, record #1 is valid data, record #2 and #3 are bad records.

that of its neighbors. If the photocount value of a bin was greater than ± 3 standard deviations from its neighbors, this bin value was replaced by the arithmetic mean value of its neighbors on each side. This data editing procedure removes spurious points from the lidar data.

When the data checking and editing were completed, the data bins were combined in both the temporal and spatial domains to improve the statistical reliability of the analysis. For the AIDA data, ten consecutive profiles in the time domain were combined. Since the original integration of the data records was 26 seconds, the new combined integration period became four minutes and 20 seconds. This interval is near the Brunt-Väisälä period, which is the smallest period of propagating gravity waves. With this time spacing of profiles, the information on the characteristics of gravity waves with periods of about twelve minutes or longer will be preserved. Next, three consecutive altitude bins were combined, reducing the height resolution from 37.5 m to 112.5 m, which is a vertical scale smaller than that expected for most gravity waves in the middle atmosphere. Because the statistical error is proportional to the inverse square root of the measured count, by combining the photocount into a 4.3-minute integration time and 112.5 m height resolution bin, the measurement variance was reduced by a factor of approximately 5.5.

2.3 Photon Signal Processing

The backscattered signal from 30 to 90 km corresponds to scattering by molecules under middle atmosphere quiet conditions. The first step of our lidar signal processing was to estimate the background noise of the returned signal and to remove this background level from the raw profiles, to obtain the corrected molecular scattered signal at this altitude range. Then a properly chosen filter was used to smooth the high-frequency noise from the profile.

2.3.1 Background Noise Determination and Subtraction

The major types of background noise are detector noise and sky background noise. Detector noise includes dark-current noise, thermal (Johnson, Nyquist) noise and electromagnetic interference (EMI) noise, which is radiated in the local laboratory environment. Sky background noise includes scattered sunlight, scattered moon light, star light, cosmic ray events, and background ionizing radiation. As shown in Figure 2.1, the photocounts in the ranges from 76 *km* to 79 *km* and above 110 *km* were nearly constant. The returned signals in these two ranges were due to the background noise, which should be subtracted from the entire profile to obtain the corrected return signal of the atmosphere.

A closer examination of the raw photocount profile showed that the photocounts in these two ranges, above and below the sodium layer, were actually decreasing slightly with increasing height, instead of staying constant. The signal observed in the altitude range 76 to 79 *km* was mostly due to sky background with a small contribution from the atmospheric density. At altitudes above 105 *km*, which is well above the sodium layer, the signal decrease was probably caused by the long recovery of the photomultiplier from nonlinear saturation effects. These nonlinear effects were due to signal overloading at lower altitudes or associated with the transient effect from the high voltage switching technique used. The photomultiplier nonlinearity was difficult to simulate and varied markedly during the experiment. It was not practical to estimate the system background noise from the photon signal collected above 105 *km*.

We chose a background noise region below 79 *km* to avoid possible scattering signals from the sodium layer that ranged from 80 *km* to 105 *km*. Since the molecular scattering region was below 65 *km*, the photocount from 76 to 79 *km* was used to estimate the background noise. This region corresponds to about one and one-half density scale heights above 65 *km*. The U.S. Standard Atmosphere, 1976 [USSA76, 1976], model was used to estimate the atmospheric signal

within this region. The molecular contribution to the signal within this region was typically 13% to 20%. The difference between the collected photon signal and the estimated atmospheric signal within this region was calculated as the background signal. The corrected atmospheric signal can be obtained by subtracting this background, then corrected by the square of the distance from the range bin to detector. To increase the reliability of our measurement, we stopped the profile calculation at the point where it had a statistical error of 20 percent.

2.3.2 Profile Filtering and Smoothing

A Hanning (raised cosine) filter was used to smooth the signal profiles. The Hanning filter is similar to rectangular window filter, except the averaging points are weighted by a cosine function that falls to zero at the two end points. We used a Hanning filter as,

$$\frac{(1 + \cos(\frac{\pi * i}{(n+1)}))}{2} \quad (2.3)$$

Here, n is the window size, and i is the i th data point within the Hanning window. The Hanning filter was compared with other filters and was selected as the best choice of filter for the analysis of lidar data [Philbrick *et al.*, 1987a].

The Hanning filter window size, n , has to be chosen carefully. If the window size is too small, we cannot properly smooth the high-frequency noise. If the window size is too big, we will lose the atmospheric gravity wave information. We used a dynamic filter window to deal with the decreasing photocount with altitude. A narrow window filter was applied for the high photocount at lower altitudes because the high photocount implies small statistical error. We used a 3-point window with a 0.225 km width to smooth the data points below 30 km. A 61-point Hanning filter window, which covered 6.75 km, was used to smooth the data points above 60 km.

The filter window size was changed dynamically from three points to 61 points in the range from 30 km to 60 km in proportion to the signal level. The time-integrated profile for the entire night was filtered and was used to calculate the mean-night density profile, the density ratio profile as compared with the U.S. Standard Atmosphere 1976, and the temperature profile.

The smoothing procedure for the individual profiles was somewhat different from that of the mean-night profiles. A profile of each single data run was calculated as the ratio between the single data run and whole-night total, $P'(Z)$. This $P'(Z)$ profile, shown in Figure 2.4, was normalized to unity at 30 km. Instead of smoothing the individual photocount profile, this ratio profile, $P'(Z)$ was smoothed. By smoothing the ratio profile, the individual profile's variations were correlated with the whole-night profile.

The Hanning (raised cosine) filter was used to smooth the ratio profile of the individual, 5-minute integrated, and hourly integrated profiles. The filter window size was chosen in the same way as smoothing the whole-night profile. An example of the smoothed ratio profile is shown in Figure 2.5. After smoothing operation, the smoothed ratio profile was multiplied by the whole night profile to obtain the smoothed individual, 5-minute or hourly integrated, profile. The benefit of this smoothing procedure is that the smoothing is unbiased by the signal profile's exponential characteristic as a function of height.

2.3.3 Background Subtraction before or after Smoothing

The question of whether the background noise level should be removed before or after the profile smoothing was investigated. This calculation order should not make any difference if the background noise is additive noise. Additive noise means that the return signal is the sum of the laser backscattered atmospheric signal and the background noise (including system and sky background noise). In lidar measurements, these two kinds of signal are uncorrelated signals.

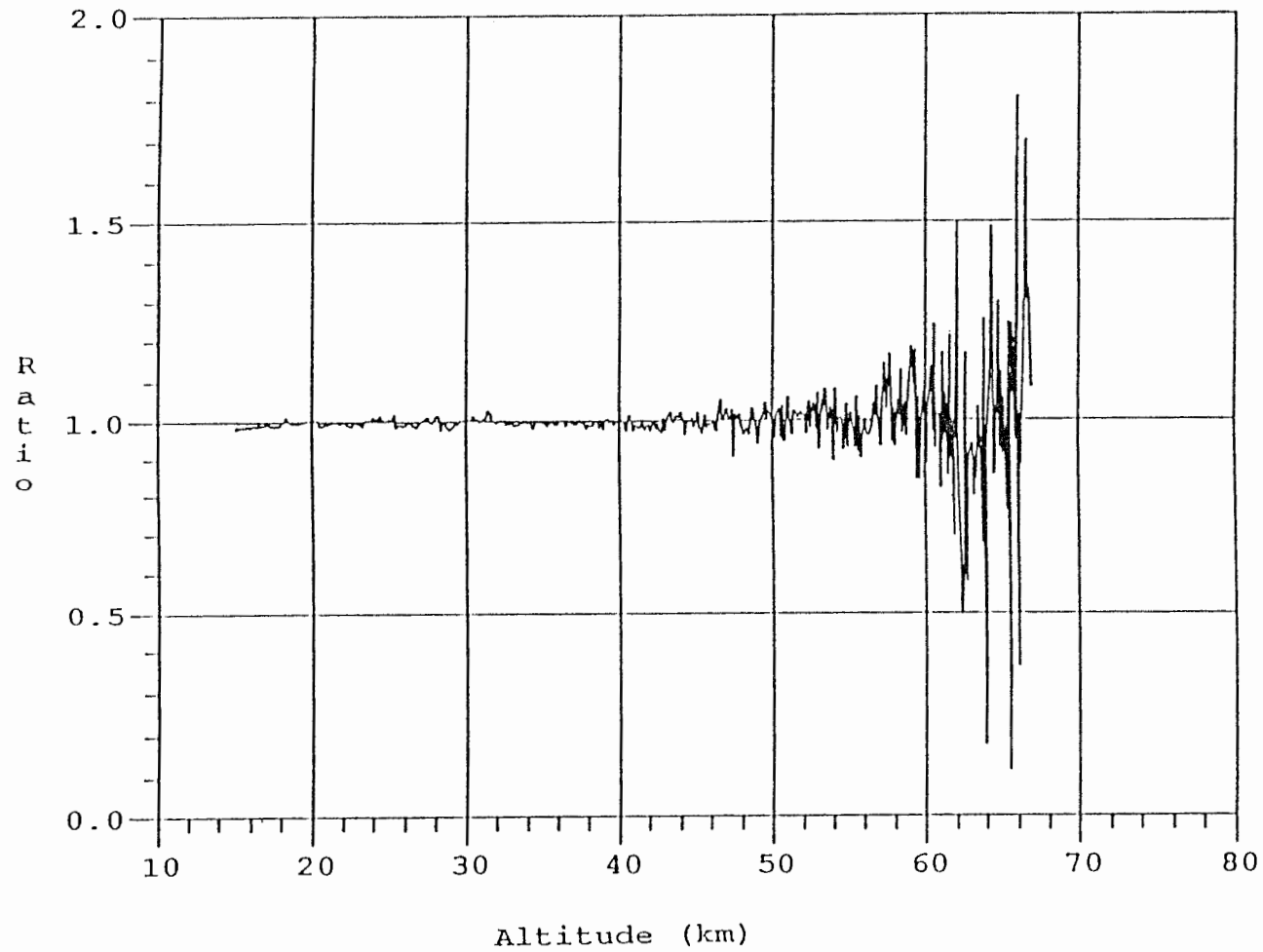


Figure 2.4. An example of an individual profile of data (26 seconds integration) ratio to mean night photocount profile, before the profile smoothing.

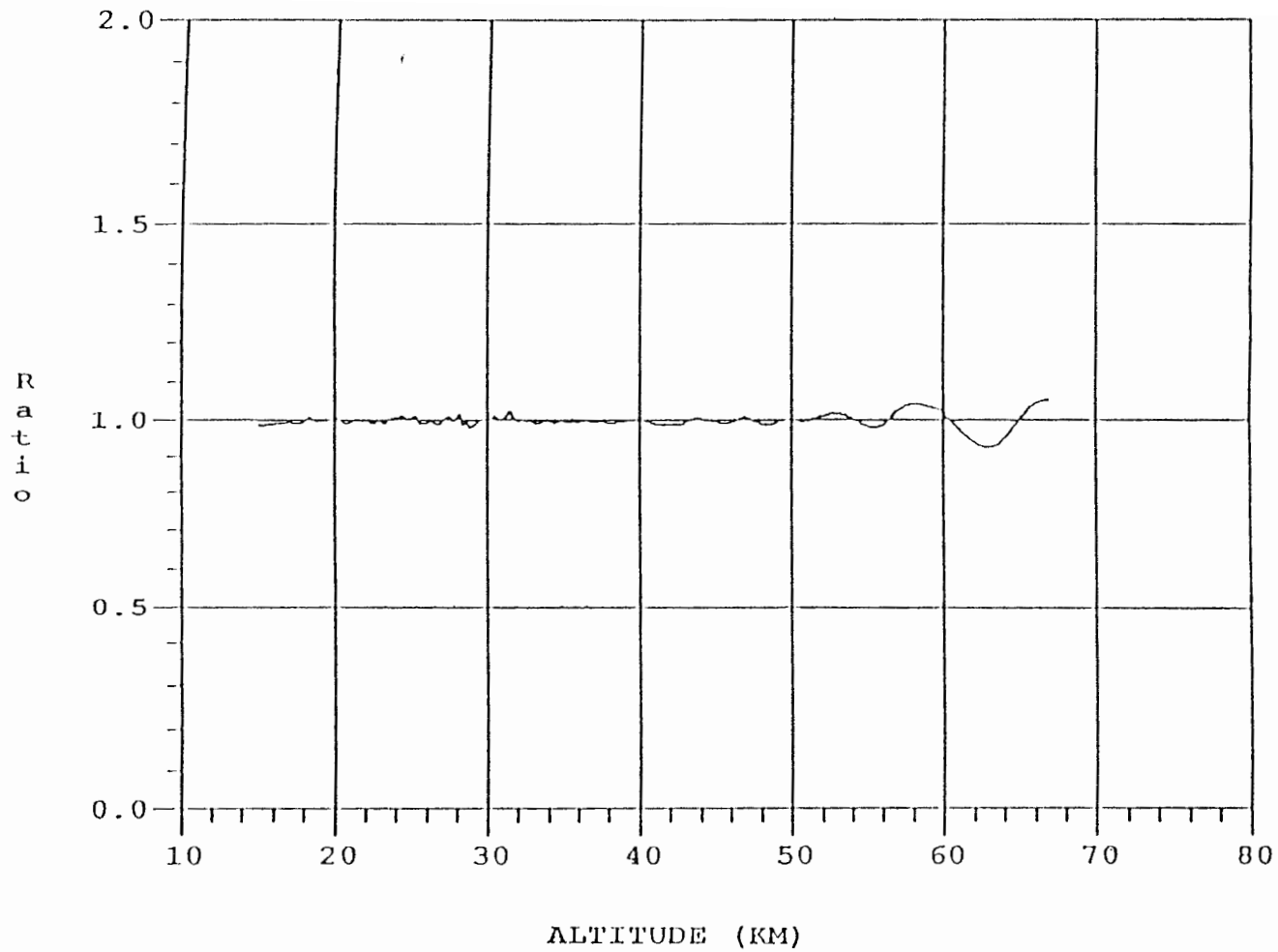


Figure 2.5. The Hanning (raised cosine) filter was used to smooth profile of individual (26 seconds integration) photocount ratio to mean night photocount.

This can be explained by the following comparison. First, we assumed that the return signal is $X(Z)$ which includes a constant background noise level B , where Z is the altitude. Then, a Hanning (raised cosine) filter, $(1+\cos Z)$, was used to smooth the photon return profile both before and after the background noise subtraction. If we use the Hanning filter to first smooth the raw profile and then subtract the background noise from this smoothed profile, the true return signal, X_1 , at altitude Z_0 can be obtained as,

$$X_1(Z_0) = \frac{1}{2\pi} \int_{-\pi}^{\pi} X(Z)(1+\cos Z)dZ - B. \quad (2.4)$$

On the other hand, if we first subtract the background noise from the raw return signal and then use the raised cosine filter to smooth this noise-subtracted profile, the final return signal, X_2 , at Z_0 is,

$$X_2(Z_0) = \frac{1}{2\pi} \int_{-\pi}^{\pi} [X(Z)-B]*(1+\cos Z)dZ, \quad (2.5)$$

Equation (2.5) can be rearranged as follows,

$$\begin{aligned} X_2(Z_0) &= \frac{1}{2\pi} \int_{-\pi}^{\pi} X(Z)*(1+\cos Z)dZ - \frac{1}{2\pi} \int_{-\pi}^{\pi} B*(1+\cos Z)dZ \\ &= \frac{1}{2\pi} \int_{-\pi}^{\pi} X(Z)*(1+\cos Z)dZ - B*\left\{\frac{1}{2\pi}[Z+\sin Z]_{-\pi}^{\pi}\right\} \quad (2.6) \\ &= \frac{1}{2\pi} \int_{-\pi}^{\pi} X(Z)*(1+\cos Z)dZ - B. \end{aligned}$$

This result is the same as Eq. (2.4), i.e., these two approaches are the same. Since the noise is additive, it does not matter whether we first smooth the profile and then subtract the background, or we first subtract the background noise and then smooth the profile. An example comparing these two data smoothing approaches is shown in Figure 2.6. By comparing the results of both smoothing approaches on lidar data, we show that the background noise in our lidar measurements

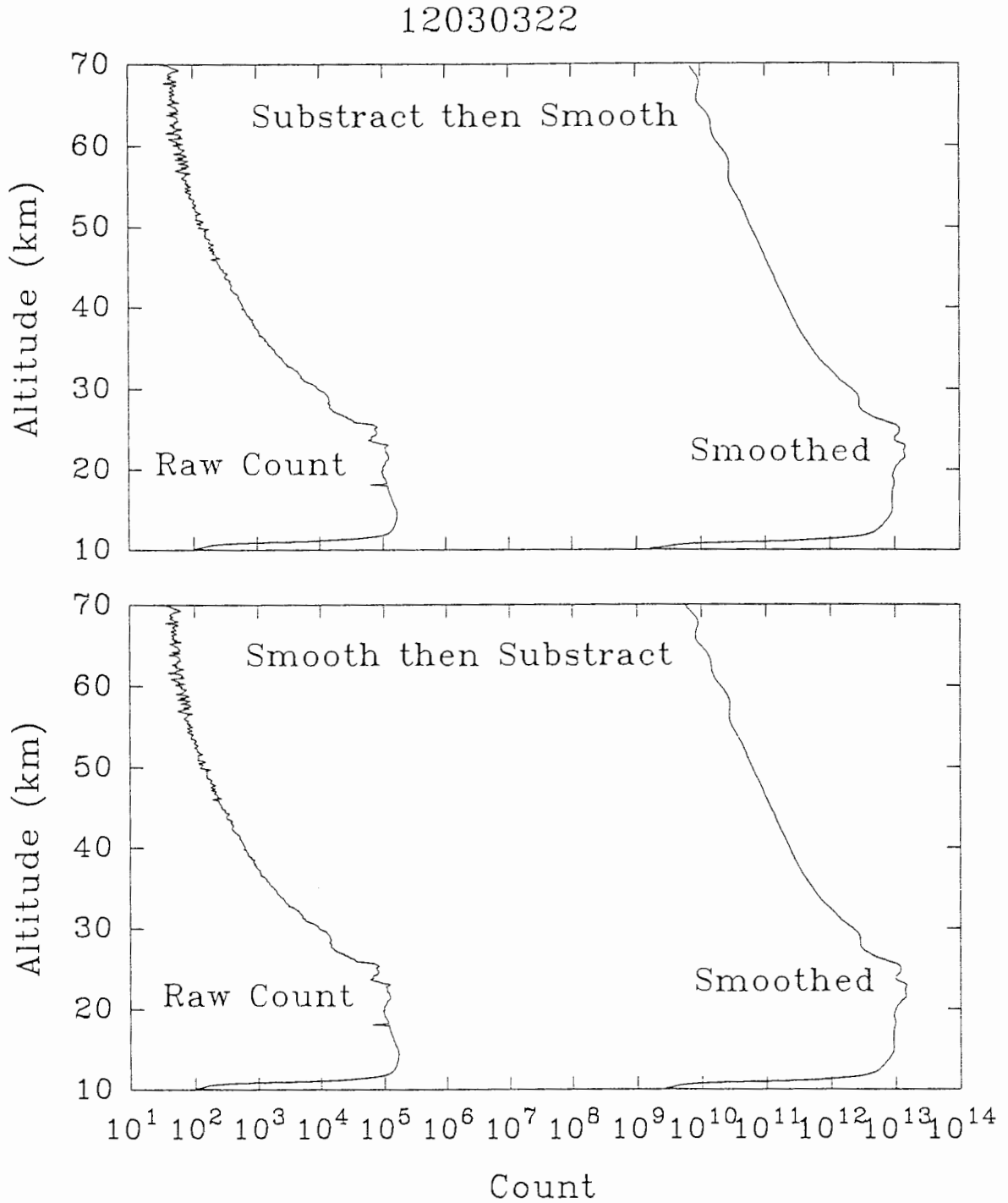


Figure 2.6. An example of data illustrating the comparison of smoothing procedures applied to a high altitude channel data, measured at 03:20 UT, 3 December 1991, by The Penn State LAMP lidar during LADIMAS Campaign.

is additive noise.

2.4 Atmospheric Profiles

Four kinds of profiles are derived from lidar atmospheric measurements: backscatter ratio profiles, relative density profiles, density ratio profiles, and temperature profiles. The backscatter ratio profile is used to study both atmospheric aerosol and cloud layers. Density, density ratio, and temperature profiles provide a unique way to study atmospheric dynamics. The different profile calculations are described in the following sections.

2.4.1 Backscatter Ratio Profile

In applying the lidar techniques to the stratospheric studies, the received signal profile, $P_r(Z)$, is compared to the signal profile that would result from the atmospheric molecules alone, $P_m(Z)$. The received signals are the elastic backscatter signals from both stratospheric gas molecules and particles. The molecular signal profile is usually from a model or from a balloon measurement which has been used to normalize the measured profile at 40 km . The result obtained from this comparison is a profile termed as "scattering ratio" and defined as,

$$R(Z) \equiv \frac{P_r(Z)}{P_m(Z)} = \frac{\beta_m(Z) + \beta_p(Z)}{\beta_m(Z)} = 1 + \frac{\beta_p(Z)}{\beta_m(Z)}, \quad (2.7)$$

where $\beta_p(Z)$ and $\beta_m(Z)$ are the elastic particle and molecule (i.e. Rayleigh) volume backscatter coefficients respectively at altitude Z . For a pure molecular region in the atmosphere, this scattering ratio is equal to one. The scattering ratio provides a measure of particle backscatter in the atmosphere. This scattering ratio profile provides a useful means to observe aerosol or cloud structures in lidar observations. Figure 2.7 presents the vertical backscatter ratio profiles from the ground to 40 km altitude from both the 355 nm and 532 nm channels measurements. These

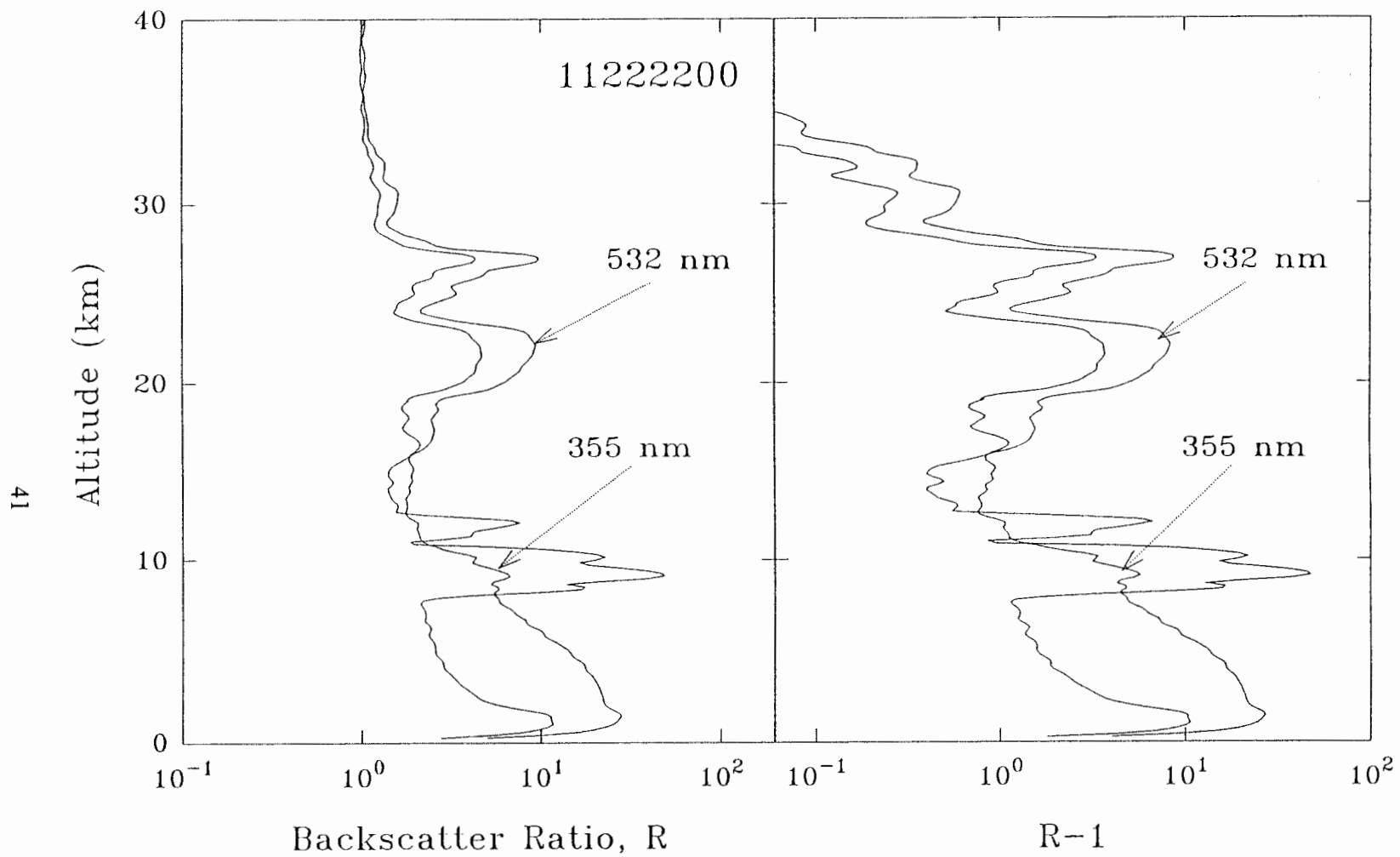


Figure 2.7. Two-wavelength lidar backscatter ratio profiles, $R(Z)$, and aerosol backscatter ratio profiles, $R(Z)-1$, measured at 22:00 UT, 22 November 1991, during the LADIMAS Campaign. Volcanic dust, cloud and aerosol layers

profiles were obtained from lidar measurements at 22:00 GMT on 22 November 1991 by the Penn State LAMP lidar during the LADIMAS Campaign. The two-wavelength lidar measurements showed that a particle-free atmosphere was present above 34 km . Above that altitude, the lidar backscatter ratio was approximately one for both channels. Two major stratospheric aerosol layers, shown on both channels, were located between 19 and 30 km . The backscatter ratio profiles indicated cirrus cloud layers from 8 to 13 km , the cirrus cloud signal was most distinct on the 532 nm channel.

2.4.2 Density and Density Ratio Profiles

The profiles of particular interest to us are the relative density profiles, the density to model ratio profiles, and the temperature profiles. A relative density profile is obtained by normalizing the signal profile to the model density at 30 km for the AIDA results. The returned signal above 30 km was assumed from molecular scattering only. An example of the density profile from a one-hour integration, beginning at 8:00 pm, on the night of March 30, 1989, is shown in Figure 2.8.

The density ratio profile is calculated by dividing the measured density by the model density. This profile is useful for observing wave structure and variations of the atmosphere, these wave structures are frequently not discernible in the log plot of the density profile. An example of density ratio profile for a one-hour integration at 8:00 pm local time on March 30, 1989 is shown in Figure 2.9. Another example of the mean-night density ratio profile on January 15, 1989 is shown in Figure 2.10, with one standard deviation error bars. The profile calculation was stopped at an upper end where the statistical error reached 10% . With commercially available high-power lasers and improved electronic detection systems, the Rayleigh lidar can be a reliable tool in observing wave activity through middle-atmosphere.

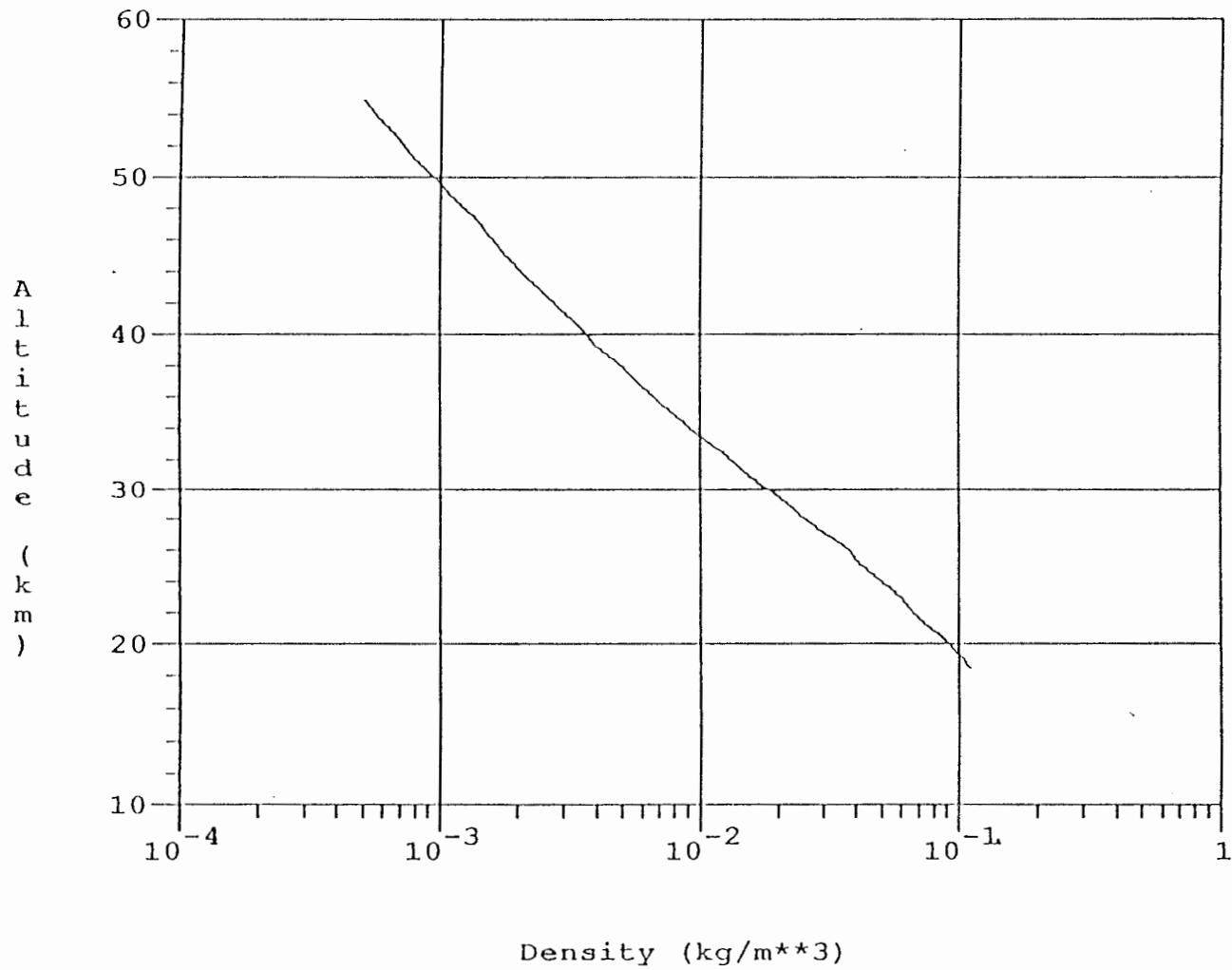


Figure 2.8. An example of an one hour density profile measured at 8 pm local time, 30 March 1989, during the AIDA Campaign.

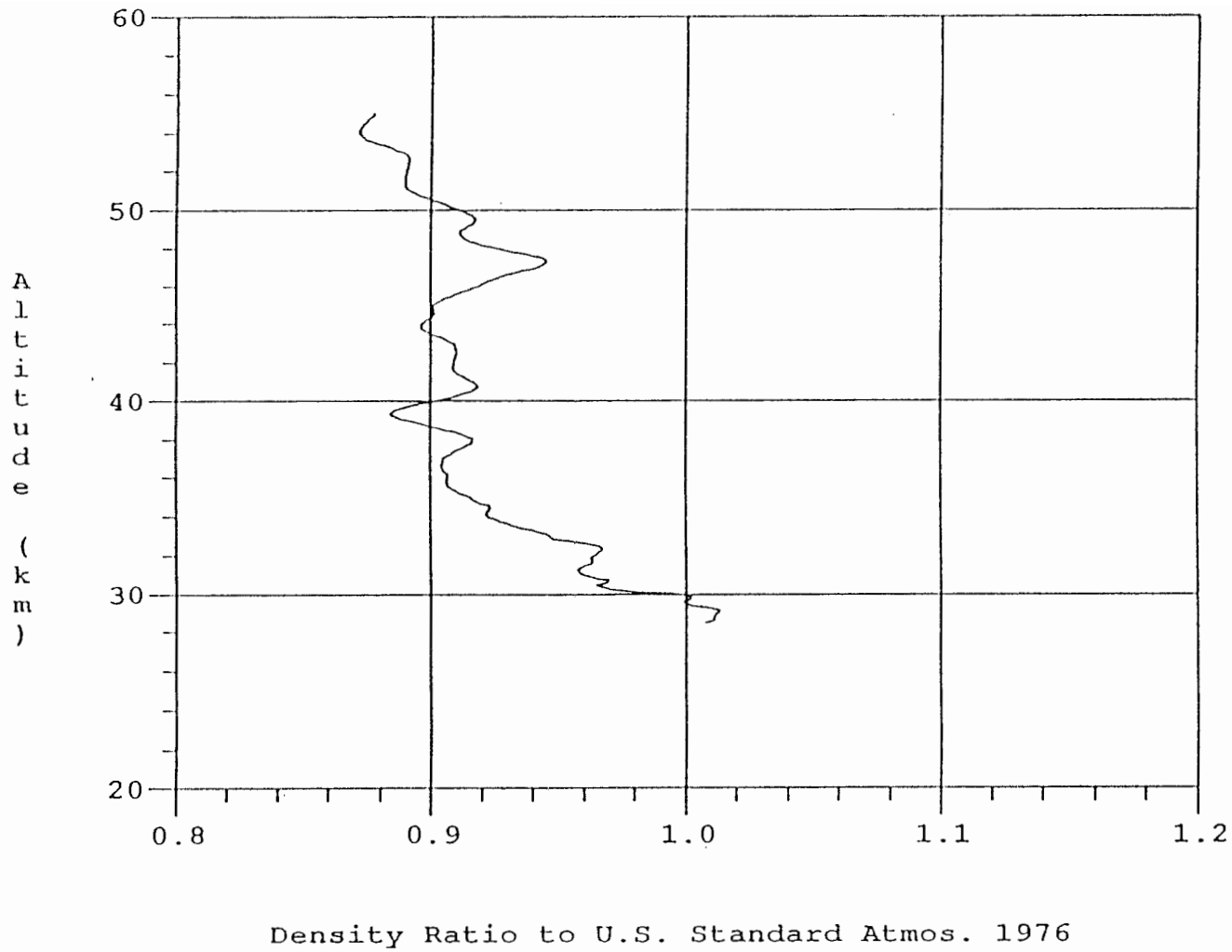


Figure 2.9. The hourly density ratio to U.S. Standard Atmosphere 1976 profile measured at 8 pm local time, 30 March 1989, during AIDA Campaign.

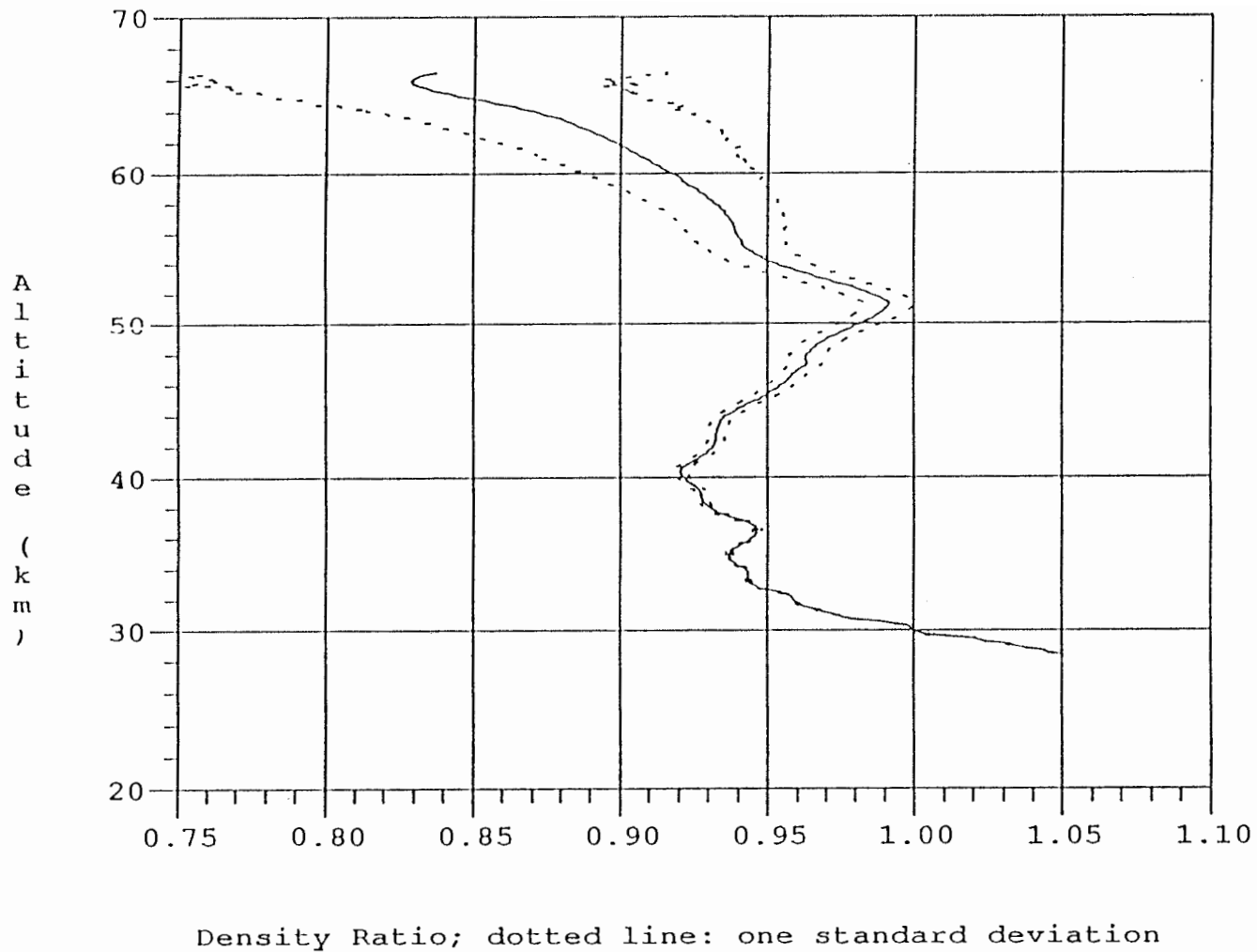


Figure 2.10. The mean-night density ratio profile measured on 15/16 January 1989 during AIDA Campaign. Dotted lines are one standard deviation error lines.

2.4.3 Temperature Profile

Atmospheric temperature is determined from atmospheric density by using the hydrostatic equilibrium equation, which states that the upward force due to the surrounding air pressure is counterbalanced by the downward gravitational force,

$$\frac{dp}{dZ} = -\rho g, \quad (2.8)$$

where,

p is the air pressure,

ρ is the air density.

By integrating both sides of Eq. (2.7), we have,

$$-\int_{P(Z_1)}^{P(Z_2)} dP(Z) = \int_{Z_1}^{Z_2} g(Z)\rho(Z)dZ, \quad (2.9)$$

which can be expressed as,

$$P(Z_1) - P(Z_2) = \int_{Z_1}^{Z_2} g(Z)\rho(Z)dZ. \quad (2.10)$$

From Eq. (2.9) and the ideal gas law,

$$P(Z) = \frac{\rho(Z)RT(Z)}{M}, \quad (2.11)$$

we can obtain an equation that relates atmospheric temperature to atmospheric density as follows [Philbrick *et al.*, 1985],

$$T(Z_1) = T(Z_2) \frac{\rho(Z_2)}{\rho(Z_1)} + \frac{M g}{R} \int_{Z_1}^{Z_2} \frac{\rho(Z)}{\rho(Z_1)} dZ, \quad (2.12)$$

where,

R is the universal gas constant,

$g(Z)$ is acceleration due to gravity,

M is the mean molecular weight,

$T(Z_1)$ is the atmospheric temperature at altitude Z_1 ,

$T(Z_2)$ is the upper level initial temperature at altitude Z_2 from atmospheric model,

Z_2 is the altitude of the initial temperature estimate.

Here, atmospheric densities at two adjacent altitudes appear as a ratio in the integration. Therefore, if the atmospheric density or the measured signal, $N_R(Z)$, which is proportional to the air density at each range, Z , is known, the atmospheric temperature profile can be calculated by integrating Eq. (2.11) downward with an initial upper level temperature, $T(Z_2)$. This initial temperature value is from the U.S. Standard Atmosphere, 1976, model, or some other model. The calculation loses its sensitivity to the initial value selection within one to one and one-half density scale heights (approximately 7 to 10 km).

The accuracy of this temperature integration technique depends upon the Rayleigh photocount $N_R(Z)$ and the accuracy of the upper end initial temperature, $T(Z_2)$. Through the error propagation analysis, the temperature variance at Z is expressed as,

$$\text{Var}[T(Z)] = \frac{T^2(Z)}{N_R(Z)} + \left\{ \text{Var}[T(Z_2)] + \frac{T^2(Z_2)}{N_R(Z_2)} \right\} e^{-\frac{2(Z_2-Z)}{H}}, \quad (2.13)$$

where, H is the atmospheric scale height, which is approximately 7 km in the upper stratosphere and lower mesosphere [Metzger and Gardner, 1989]. The standard deviation for the temperature measurement is,

$$\text{STD}(T(Z)) \approx \frac{T(z)}{\sqrt{N_R(Z)}}. \quad (2.14)$$

The observed mean night temperature profile on January 15, 1989, is shown in Figure 2.11, with the dashed curves representing one standard deviation error.

The temperature calculation must proceed through a downward integration to avoid integration divergence. This can be understood by considering that the statistical error of temperature is proportional to the square root of the measured density. If the calculation were to proceed upward, the error term in the integration, *ie.* the $\rho(Z)/\rho(Z_i)$ term in Equation (2.11), would increase. Consequently, if we integrate upward to obtain temperature, the density calculation error will be accumulated and the temperature integration will be divergent. On the other hand, if we proceed with the temperature integration downward, the statistical error becomes smaller as we move lower. As the density error ratio term $\rho(Z)/\rho(Z_i)$ becomes smaller, the temperature integration will converge to the true value.

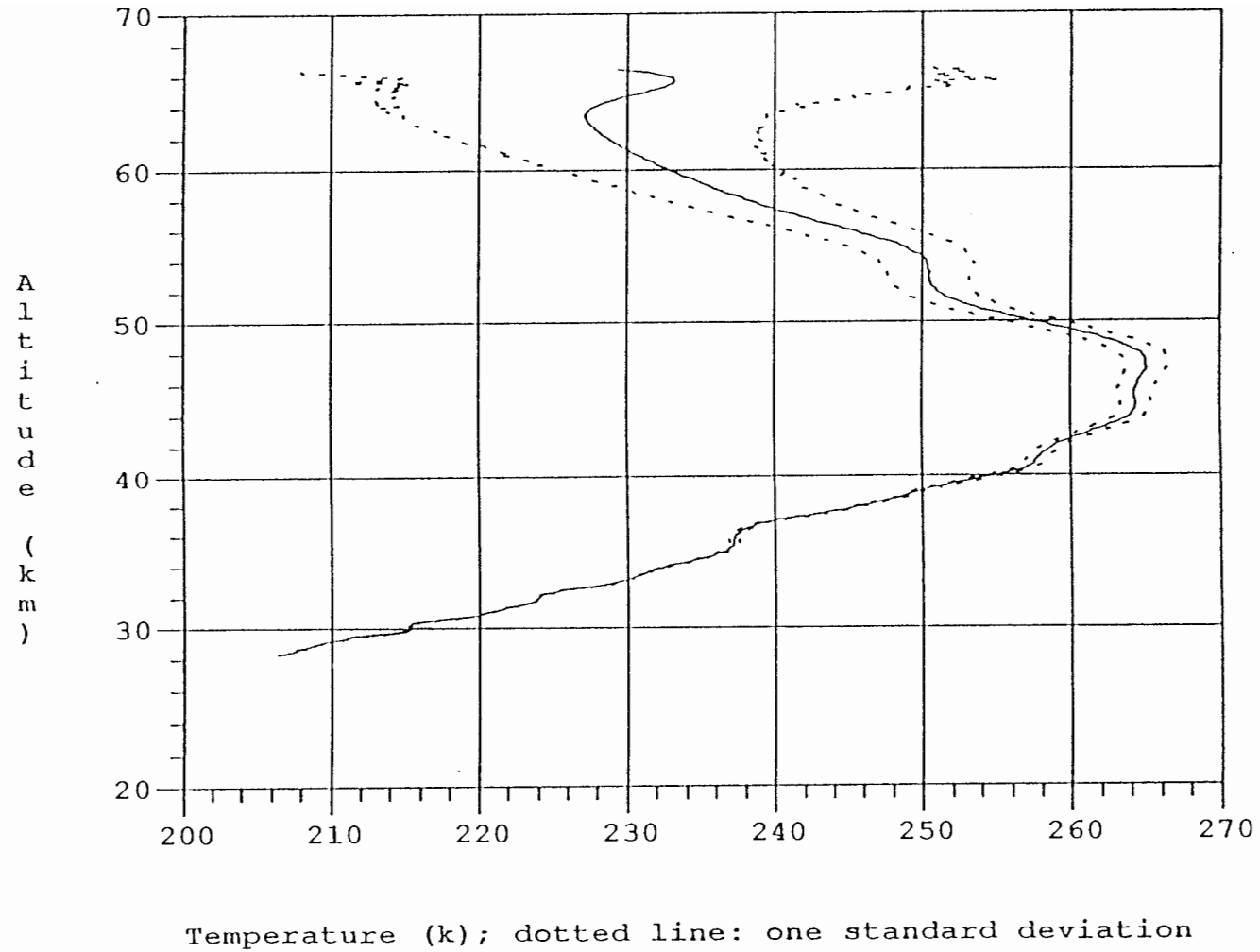


Figure 2.11. The mean-night temperature profile measured on 15/16 January 1989 during AIDA Campaign. Dotted lines are one standard deviation error lines.

Chapter 3

MULTI-WAVELENGTH LIDAR DETECTION OF AEROSOL AND ATMOSPHERIC PROPERTIES

The wavelength dependence of backscatter by molecules is different from that by particles, which suggests the use of a multi-wavelength lidar for the separation of aerosol and molecular backscatter signals. A multiple wavelength lidar can, in principle, be used to measure the wavelength dependence of the aerosol backscatter cross-section. Assuming that the wavelength dependence of molecules differs from that of particles, lidar measurements at two or more different wavelengths can be used to separate the molecular backscattering signal from the particle backscattering signal. Measurements of the molecular scattering signals give us the accurate profile of the relative atmospheric density. This density profile provides us with information about atmospheric pressure and temperature from the condition of hydrostatic equilibrium of the atmosphere (See section 2.4.3).

Using the different wavelength dependencies of molecules and particles, we have attempted to solve the inversion problem of separating the particle scattering from the molecular scattering using the two-wavelength lidar return signal. We developed a matching method that was based upon the analysis of lidar data to determine stratospheric aerosol presence. The matching method assumes a particle-free layer above a certain altitude (matching height). In the present work with the LAMP results, we assumed that there was no significant particle scattering above *40 km* based on our measurements. Thus, we analyzed the lidar signal collected at *40 km*, and above using the one-wavelength Rayleigh profile technique.

3.1 Multi-wavelength Lidar for Particle Detection

The aerosol backscattering cross-section is determined according to the physical and

chemical properties of the particles (their size, shape, and composition) and the laser wavelength. Lidar can be used to measure the vertical distribution of the particle volume extinction coefficient σ_a and backscatter coefficient β_a . The wavelength dependence of the particle backscatter coefficient is primarily associated with particle size distribution, assuming that the particles are spherical particles. The wavelength dependence of extinction and backscatter coefficients for molecular (Rayleigh) scatters have the following approximate forms,

$$\sigma_m \propto \lambda^{-4}, \quad (3.1)$$

$$\beta_m \propto \lambda^{-4}. \quad (3.2)$$

For the particle scatters, the wavelength dependence of extinction and backscatter coefficients are assumed to have the forms,

$$\sigma_p \propto \lambda^{-q}, \quad (3.3)$$

$$\beta_p \propto \lambda^{-q}. \quad (3.4)$$

The particle wavelength dependence, q , has been found to be in the range $0.7 \leq q \leq 1.9$. [Woodman, 1974; Cooney, 1987]. The wavelength dependence of particle scattering is therefore significantly different from that of the molecular scattering. It is this difference which makes the separation of the particle signal from the molecular signal possible.

Between October 8, 1991 and January 2, 1992, the Penn State LAMP (Lidar Atmospheric Measurements Program) lidar was on board the German research vessel *RV POLARSTERN* in a study called Latitudinal Distribution of Middle Atmosphere Structure (LADIMAS) [Philbrick *et al.*, 1992]. Besides the study of the latitudinal distribution of atmospheric structure, this campaign provided an opportunity to monitor the stratospheric aerosol layer latitudinal distribution, following the eruption of the Pinatubo volcano in June 1991 [Stevens, 1992]. The particles were

distributed throughout the stratosphere with a concentration peak near 20 km , which is frequently referred to as the Junge layer, Junge *et al.* [1961], and Junge and Manson [1961]. The major source of sulfate particles in the stratosphere is the sulfur-containing gas and particles emitted by volcanic eruptions and injected into the stratosphere [Melfi, 1976]. The significance of stratospheric aerosols is their possible effect on radiation transfer through the atmosphere and the subsequent effect on the Earth's total radiation balance.

To separate the particle portion of the scattering signal from the total returned signal, the lidar profiles are presented in terms of backscatter ratio, $R(Z)$, as,

$$R(Z) = 1 + \frac{B_p(Z)}{B_m(Z)}, \quad (3.5)$$

where $B_p(Z)$ and $B_m(Z)$ are the particle and molecular backscattering signals respectively. This scattering ratio, $R(Z)$, is also related to the turbidity [van de Hulst, 1981]. The turbidity is defined as the ratio of attenuation due to both molecules and particles to the attenuation due to molecules alone. The aerosol backscatter ratio, which is the ratio of the aerosol volume backscattering cross-section to the molecular volume backscattering cross-section, is defined as $R(Z) - 1$. The term $B_p(Z) + B_m(Z)$ is proportional to the lidar signal times the squared distance, Z^2 , from ground. We estimate the molecular component of the backscattering signal B_m from a model density, or from the retrieval of the atmospheric molecular density by means of temperature and pressure soundings. In this two-wavelength lidar approach, model density profiles from U.S. Standard Atmosphere, 1976 were used.

The lidar backscatter ratios for two-wavelength lidar measurements, R_1 and R_2 are,

$$R_1(Z) = 1 + \frac{B_{p1}(Z)}{B_{m1}(Z)}, \quad (3.6)$$

and,

$$R_2(Z) = 1 + \frac{B_{p2}(Z)}{B_{m2}(Z)}, \quad (3.7)$$

where, subscripts 1 and 2 represent the measurements from 532 nm (green) and 355 nm (UV), respectively. The two-wavelength lidar backscatter ratio profiles, $R_1(Z)$ and $R_2(Z)$, and aerosol backscatter ratio profiles, $R_1(Z) - 1$ and $R_2(Z) - 1$, at 03:20 UT, Dec. 3, 1991 are shown in Figure 3.1. A backscatter ratio $R(Z) = 1$, represents a region with nearly no particles. From the two-wavelength backscatter ratio profiles, we observed particles up to 35 km even six months after the Pinatubo eruption.

In a two-wavelength lidar system, two laser beams are emitted into the atmosphere simultaneously. Two lidar equations are used to describe the received power at each wavelength as,

$$P_1(Z) = P_{L1} \frac{A_L}{Z^2} \zeta_1 \beta_1 \frac{C_T}{2} e^{-2 \int_0^Z \alpha_1(r) dr}, \quad (3.8)$$

$$P_2(Z) = P_{L2} \frac{A_L}{Z^2} \zeta_2 \beta_2 \frac{C_T}{2} e^{-2 \int_0^Z \alpha_2(r) dr}, \quad (3.9)$$

where

$P_{1,2}(Z)$ are the received laser powers at a time corresponding to the leading edge of two laser pulses reaching to the range Z with wavelengths λ_1 and λ_2 respectively,

$P_{L1,L2}$ are the transmitted laser pulses power of λ_1 and λ_2 ,

A_L is the area of telescope primary mirror,

Z is the distance from telescope to the target area,

$\zeta_{1,2}$ are the system efficiencies for lidar systems at λ_1 and λ_2 ,

$\beta_{1,2}$ are the volume backscattering coefficients at λ_1 and λ_2 ,

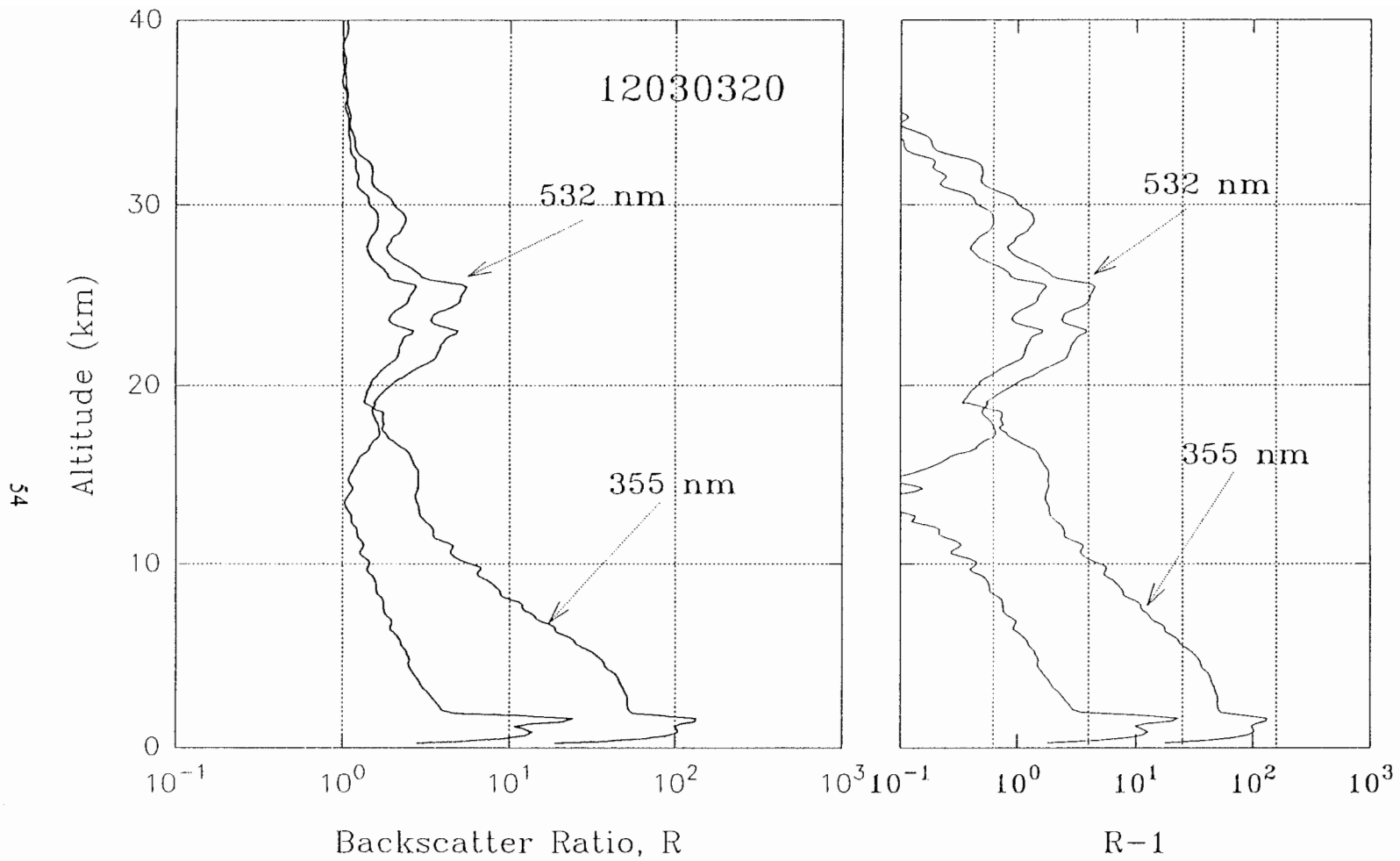


Figure 3.1. The lidar backscatter ratio profile, $R(Z)$, and particle ratio profile, $R(Z)-1$ measured at 03:20 UT on 3 December 1991. In the backscatter ratio calculations, model density profiles from U.S. Standard Atmosphere, 1976 were used.

c is the speed of light,

τ is the integration time of the detector,

$\alpha_{1,2}$ are the two-way attenuation coefficients at wavelength λ_1 and λ_2 .

The backscatter ratio profiles, $R(Z)$, from ground to 40 km for a thirty-minute integration period at 22:00 UT on 22 November 1991, at both 532 nm and 355 nm, are shown in Figure 3.2. By assuming a particle free atmosphere above 40 km, the normalization of lidar return profiles to $R_1(Z) = 1$ and $R_2(Z) = 1$ were performed in the region near 40 km. In Figure 3.2, the scattering ratio profiles of both 532 nm and 355 nm are close to unity above 35 km, which confirmed the assumption of a particle-free atmosphere above 40 km. The Pinatubo volcanic particle layer caused strong scattering in the lower stratosphere between 20 and 30 km, and some volcanic particles penetrated all the way up to 33 km. In the lower altitude region, from 8 to 13 km, cirrus clouds were clearly observed on the 532 nm lidar return profile but were not as distinct on the 355 nm lidar profile.

From the lidar backscatter ratios R_1 and R_2 , the backscatter signals contributed by particles at both wavelengths, B_{p1} and B_{p2} , can be calculated as,

$$B_{p1} = (R_1 - 1)B_{m1}, \quad (3.10)$$

and

$$B_{p2} = (R_2 - 1)B_{m2}, \quad (3.11)$$

respectively. Another way to observe the distribution of atmospheric particles or clouds is by using the two-wavelength particle backscatter ratio profile. This ratio profile is defined as the ratio of the volume particle backscattering cross-section, represented by backscattered signal, at 532 nm, B_{p1} , to the volume particle backscattering cross-section at 355 nm, B_{p2} , as,

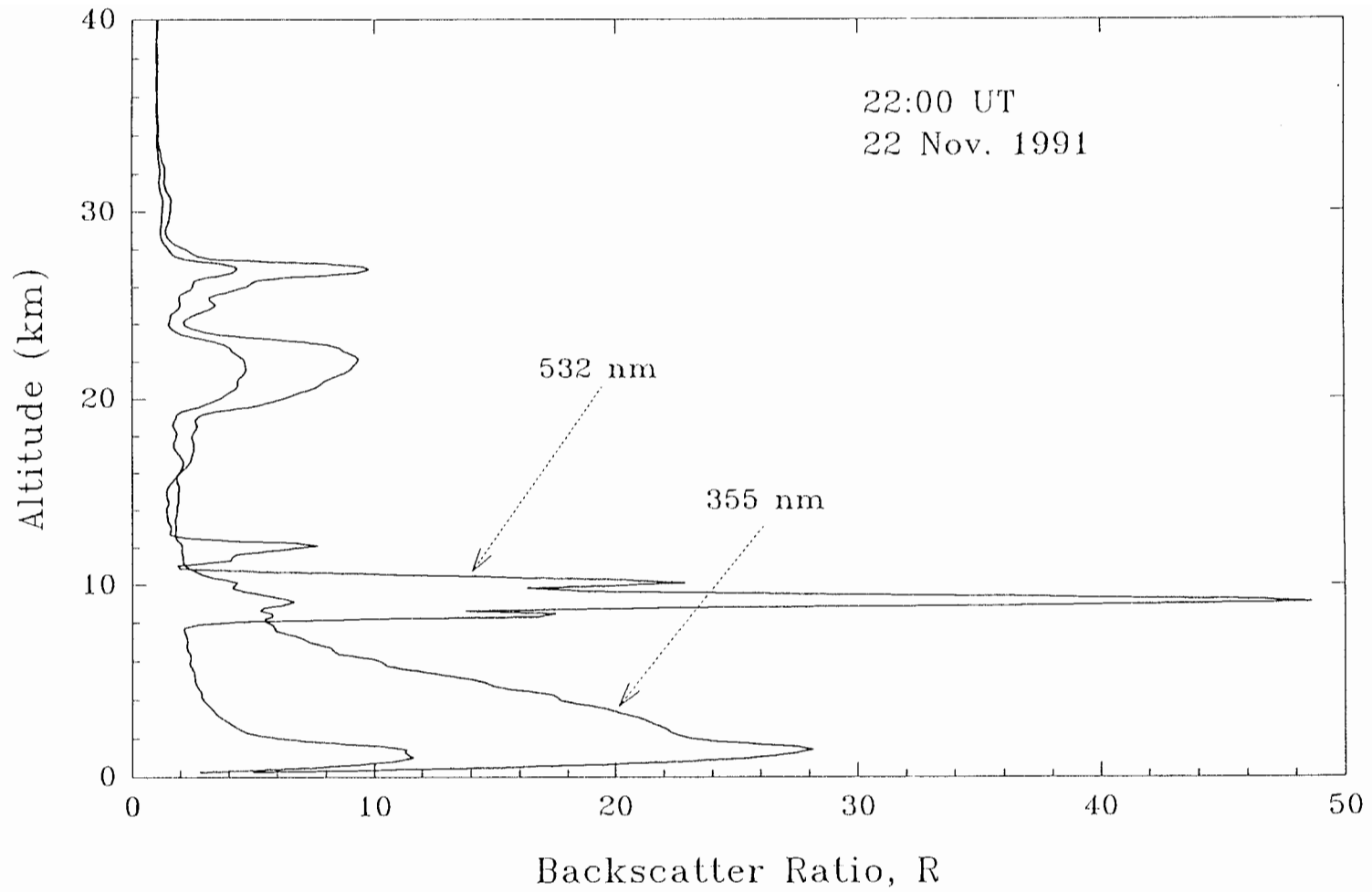


Figure 3.2. The lidar backscatter ratio profiles of 532 nm and 355 nm measured at 22:00 UT on 22 November 1991.

$$R_{12} \equiv \frac{B_{p1}}{B_{p2}} . \quad (3.12)$$

This two-wavelength particle backscatter ratio profile provides a measurement of aerosol and cloud properties. Figure 3.3 shows an example 30-minute integration of the two-wavelength particle backscatter ratio profile from ground to 40 km at 22:00 UT on 22 November 1991. Although the lidar backscatter ratio profiles, $R(Z)$, of 532 nm and 355 nm, are changing with altitude, this two-wavelength particle backscatter ratio (R_{12}) profile has a nearly constant value at the stratospheric volcanic dust layer, from 19 km to 32 km. The value of R_{12} is about 0.5, and it was nearly constant during the three-month period of the LADIMAS Campaign. For the cirrus cloud layer between 8.5 and 13 km, this R_{12} has a wide range of values. The variations of this two-wavelength particle backscatter ratio in the cirrus cloud layer are caused by the different shape, orientation, and size distributions of cirrus cloud particles.

For the stratospheric volcanic aerosol layer that we observed on the night of 22 November 1991, the particles over this region were the volcanic aerosols resulting from the Pinatubo volcano eruption in June 1991. By the time of the observation, sedimentation took away most volcanic dust, leaving only the small particles with uniform size through this region. The uniform size and other properties of the particles is deduced from the stable value of the wavelength dependence (see Figure 3.3). The wavelength dependence, q , of stratospheric volcanic aerosol layer particle scattering is derived from the following relation,

$$\frac{B_{p1}}{B_{p2}} = \left(\frac{\lambda_2}{\lambda_1}\right)^q. \quad (3.13)$$

Thus, the wavelength dependence q of stratospheric particle is

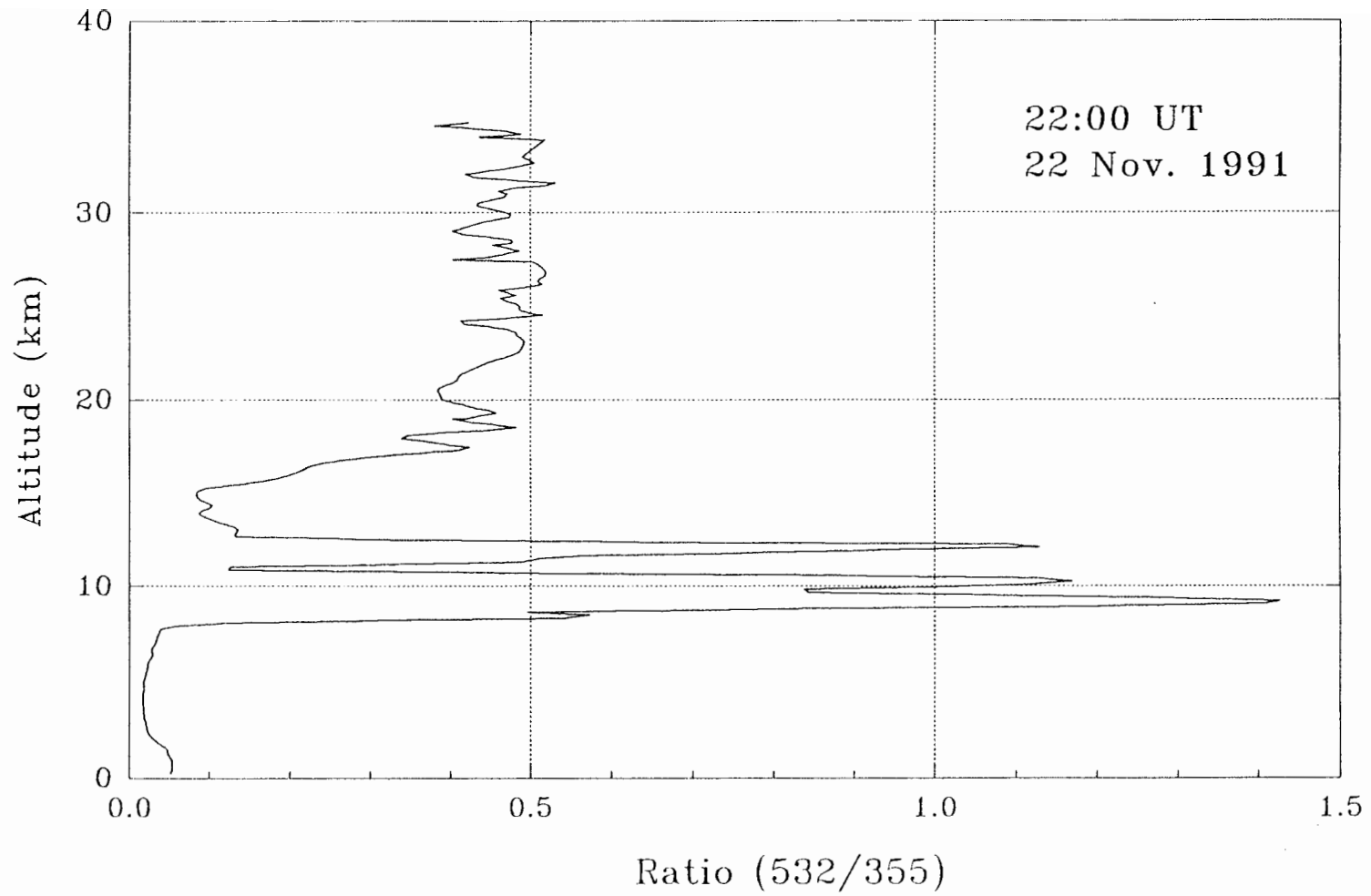


Figure 3.3. The two-wavelength particle backscatter ratio (R_{12}), β_{a1}/β_{a2} , measured at 22:00 UT on 22 November 1991.

$$q = \frac{\ln\left(\frac{B_{p1}}{B_{p2}}\right)}{\ln\left(\frac{\lambda_2}{\lambda_1}\right)}. \quad (3.14)$$

The wavelength dependence value q , which we calculated from the LADIMAS Campaign measurements ranged between 1.1 and 2.3, with a mean value of 1.66. This value can be compared to the lidar polar stratospheric cloud observations by Toon *et al.* [1990]. In their polar stratospheric cloud (PSC) observations at 603 nm and 1064 nm, they found the wavelength dependent value, q , ranging from 2 to 3 for PSC type 1b clouds. They suggested that these particles were most likely to be nearly spherical and with radii on the order of 0.5 μm . From our lidar observations, five months after the Pinatubo eruption, we can infer that the stratospheric volcanic aerosols were most likely to have a size from 0.5 μm to 0.75 μm with wavelength dependence $q = 1.66$ [Toon *et al.* 1990]. The measured two-wavelength particle backscatter ratios, at the stratospheric aerosol layer during the LADIMAS Campaign 1991, is shown in Table IV, together with the stratospheric aerosol wavelength dependence.

On 29 March 1992, nine months after the Pinatubo eruption, lidar observations of the stratospheric aerosol layer were performed at Penn State. The measured two-wavelength lidar profiles are shown in Figure 3.4. On the left of the figure, the two-wavelength returns from ground to 40 km are shown with a model molecular profile at each wavelength (shown by a dotted line). The Raman signal of the N_2 profile and water vapor profile are also shown on the figure, this will be discussed in Chapter 4. The two-wavelength particle backscatter ratio profile is shown on the right of the figure. From the comparison of the two-wavelength particle backscatter ratio profiles, R_{12} , on 29 March 1992 and on 22 November 1991, we notice the settling of the volcanic aerosol layer. On the two-wavelength particle backscatter ratio profiles of 29 March 1992, there

Table IV: Two-Wavelength Particle Backscatter Ratio (R_{12}) at the stratospheric aerosol layer during LADIMAS Campaign 91, with the corresponding one σ standard deviation error, the average stratospheric aerosol wavelength dependence \bar{q} , and its range.

Date/Time	$B_{\lambda_1}/B_{\lambda_2}$	σ	\bar{q}	q Range
1122/2200	0.4596	0.0386	1.92	1.7-2.1
1122/2242	0.5290	0.0784	1.57	1.2-1.9
1123/0121	0.4932	0.0390	1.75	1.6-1.9
1124/0028	0.4405	0.0447	2.23	1.8-2.3
1126/0156	0.5131	0.0505	1.65	1.4-1.9
1129/0102	0.4959	0.0550	1.73	1.5-2.0
1129/0150	0.6059	0.0356	1.24	1.1-1.4
1201/0102	0.4321	0.0342	2.07	1.9-2.3
1201/0137	0.5518	0.0559	1.47	1.2-1.7
1203/0320	0.4542	0.04035	1.95	1.7-2.2
1203/0419	0.4981	0.03265	1.72	1.6-1.9
1205/0100	0.5518	0.05594	1.47	1.2-1.7
1205/0151	0.5965	0.04985	1.27	1.1-1.5
1205/0326	0.5203	0.04363	1.62	1.4-1.8
1205/0402	0.5936	0.04193	1.29	1.1-1.5
Mean	0.5157		1.66	1.1-2.3
Std. Dev.	0.056		0.29	

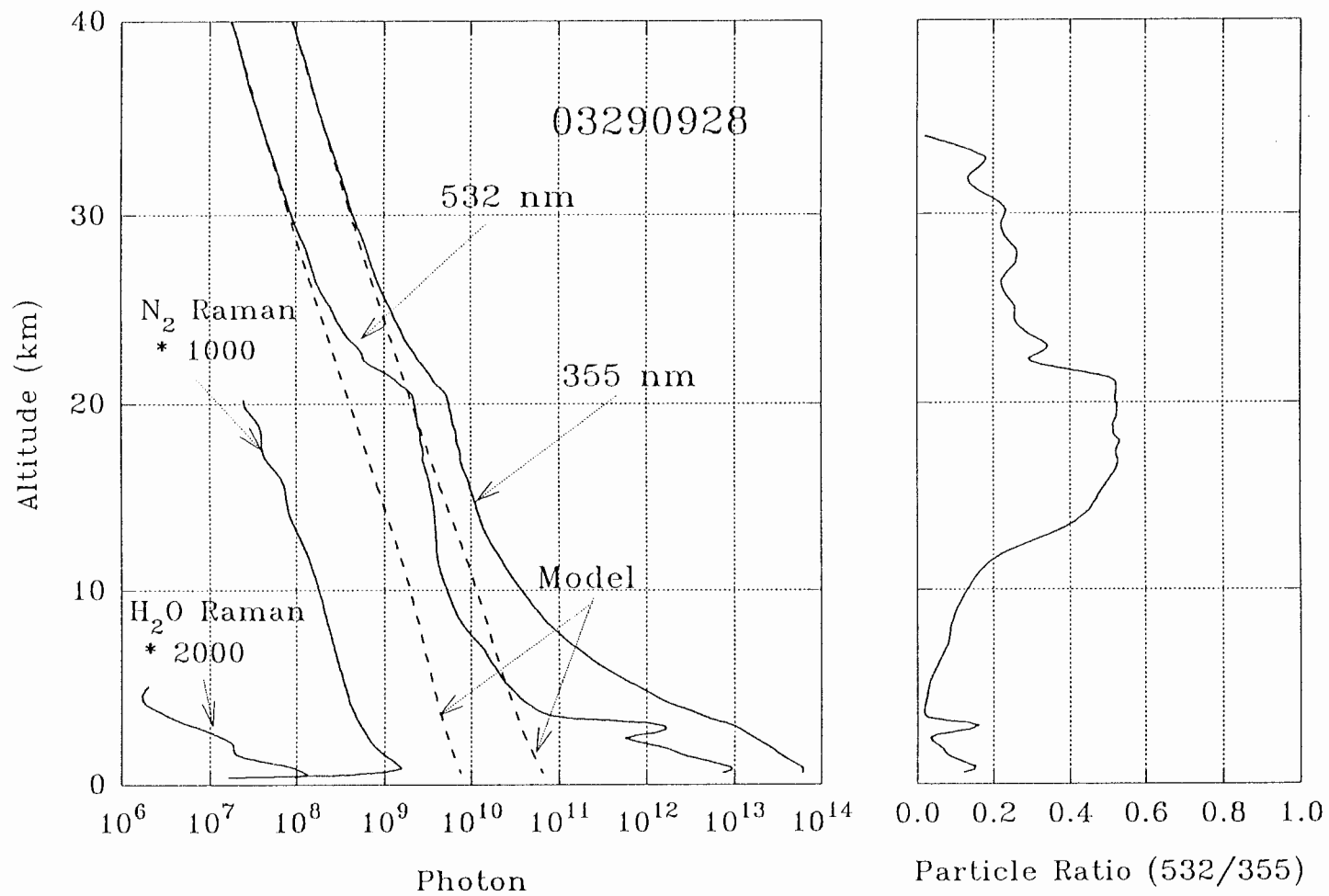


Figure 3.4. The two-wavelength lidar return profiles and two-wavelength particle backscatter ratio (R_{12}) profile measured at 09:28 UT on 29 March 1992.

appeared to be two different groups in the altitude region from 17 km to 32 km . Between 17 and 22 km , the ratio was about 0.5 , which was about the same as the value that we observed during the LADIMAS measurements, four month early. While at higher altitudes, 22 to 32 km , that ratio dropped to about 0.25 . This smaller ratio corresponds to particles with wavelength dependence $q = 3.4$, and with size around $0.25\ \mu\text{m}$. From the lidar observations, we concluded that nine months after the Pinatubo eruption, the volcanic dust layer at 41°N latitude with particle size of 0.5 to $0.75\ \mu\text{m}$ had settled to a lower altitude region, below 22 km . Smaller particles, with a diameter of about $0.25\ \mu\text{m}$, were left in the higher altitude region, 22 to 32 km .

We can observe the existence of particles from the ground to about 33 km from the backscatter ratio $R(Z)$ profiles (see Figure 3.2), but we cannot discern information the particle size grouping from these profiles. On the other hand, the two-wavelength particle backscatter ratio profile, Fig. 3.3, provides additional information on the rough grouping of particle sizes. In Figure 3.3, the R_{12} profile at 22:00 UT, 22 November 1991, shows one group of particles with an almost constant ratio of 0.5 from 19 to 32 km . The same ratio can be used to examine the cirrus cloud layers. In Figure 3.3, the scattering layers at 9 , 10.2 , and 12.3 km indicate a ratio of 1.1 to 1.4 . Based on the ratios, those particles may be of the similar type but they are quite different from those found in the stratospheric layers above.

Several sets of two-wavelength particle backscatter ratio profiles in the altitude range from 15 to 35 km are shown in Figure 3.5. The two profiles on the night of 22 November 1991 were almost constant from 19 to 32 km , which means that the size and other properties of aerosol particles over this region were likely to be the same. About three months later, during March 1992, the assumed larger particle size group moved down to the region between 15 and 22 km and left a smaller particle size group in the region from 22 to 32 km .

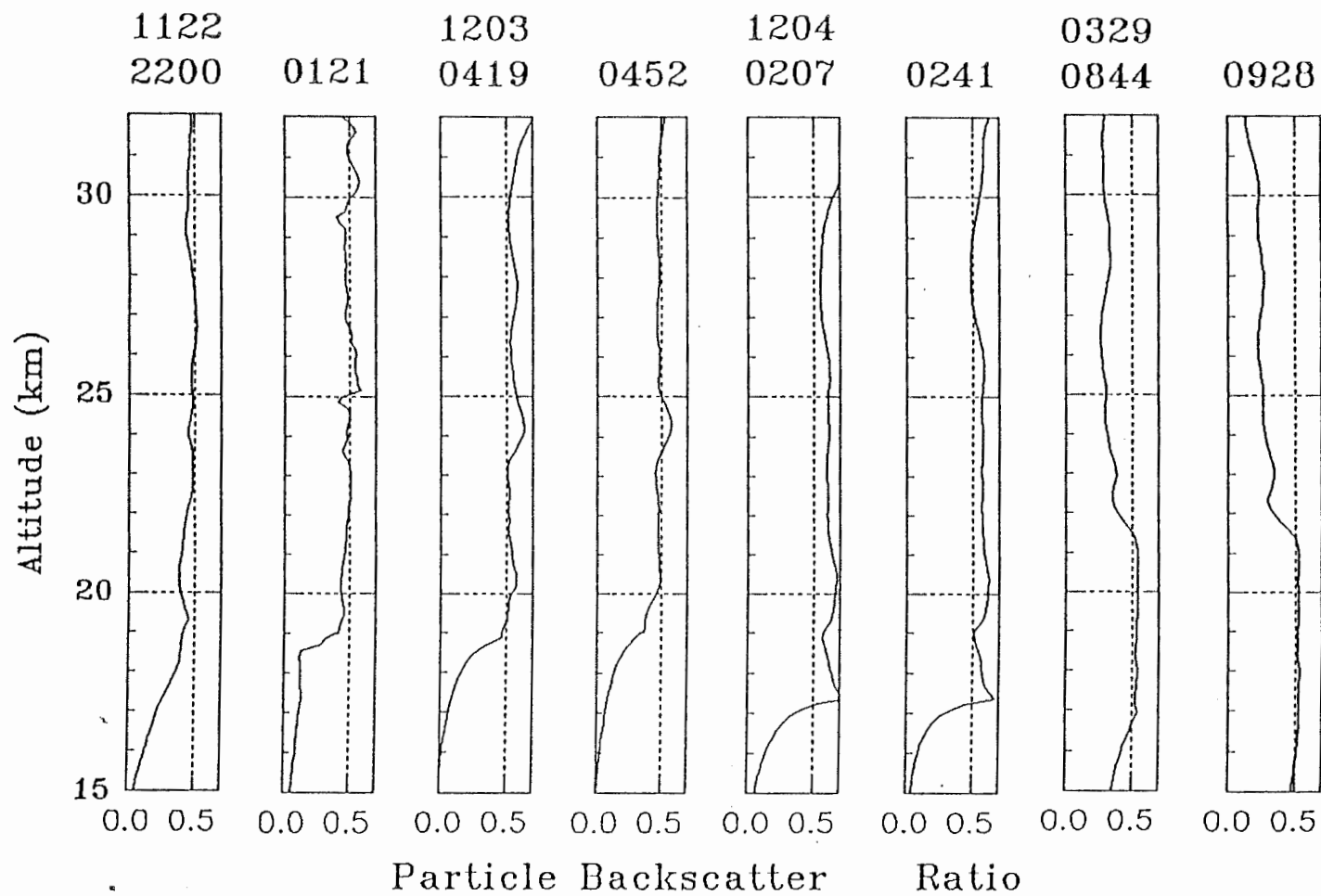


Figure 3.5. The several night's two-wavelength particle backscatter ratio (R_{12}) profiles in the altitude from 15 to 35 km, measured on 1122/2200, 1122/0121, 1203/0419, 1203/0452, 1204/0207, 1204/0241, 0329/0844, and 0329/0928.

3.2 Two-wavelength Lidar Atmospheric Properties

Lidar returns from two different laser wavelengths, λ_1 and λ_2 , provide more information about atmospheric properties than a one-wavelength lidar does. In fact, major errors in interpretation of the profiles can be made with only a single-wavelength analysis. By using multi-wavelength lidar, we want to measure the stratospheric density and temperature in the presence of particles. The two-wavelength lidar equations are expressed as equations (3.8) and (3.9). The atmospheric transmittance, $\mathcal{T}(Z, \lambda)$, for each wavelength is expressed as,

$$\mathcal{T}(Z, \lambda) = e^{-2 \int_0^Z \alpha(Z, \lambda) dz}, \quad (3.15)$$

where α is the volume extinction coefficient. In equations (3.8) and (3.9), the molecular (Rayleigh) backscattering coefficient β and extinction coefficient α at two wavelengths have the following relations,

$$\beta_m(\lambda_1) = \left(\frac{\lambda_2}{\lambda_1}\right)^4 \beta_m(\lambda_2), \quad (3.16)$$

$$\alpha_m(\lambda_1) = \left(\frac{\lambda_2}{\lambda_1}\right)^4 \alpha_m(\lambda_2), \quad (3.17)$$

$$\beta_m(\lambda_1) = \frac{3}{8\pi} \alpha_m(\lambda_1), \quad (3.18)$$

where the subscript m stands for molecules. That is, for Rayleigh (molecule) scattering, the backscattering coefficient and extinction coefficient have a fourth-power wavelength dependence and a $3/(8\pi)$ relation between α and β . For the particle scattering a set of similar relations exists as,

$$\beta_p(\lambda_1) = x * \beta_p(\lambda_2), \quad (3.19)$$

$$\beta_p(\lambda_1) = y * \alpha_p(\lambda_1), \quad (3.20)$$

$$\alpha_p(\lambda_1) = z * \alpha_p(\lambda_2), \quad (3.21)$$

where the subscript p stands for particle. However the coefficients x , y , and z do not have any unique value as the corresponding values in the case of Rayleigh scattering. These three coefficients can be determined from the scattering theory developed by Mie [1908] under the assumption that they are spherical particles. The condition for the particle detection by multi-wavelength lidar is,

$$\frac{\beta_m(\lambda_1)}{\beta_m(\lambda_2)} \neq \frac{\beta_p(\lambda_1)}{\beta_p(\lambda_2)}. \quad (3.22)$$

In other words, the wavelength dependence of the molecular (Rayleigh) backscatter is different from the wavelength dependence (q value from Equation 3.14) of the aerosol backscatter. Two different approaches have been tried to derive molecular backscattering signal from two-wavelength lidar measurements, a numerical closed-form solution and an inversion using a known two-wavelength particle backscatter ratio R_{12} . The uncertainty about the types of stratospheric particles limits the usefulness of both approaches on the stratospheric profiles of density and temperature. These two approaches are discussed in the following sections.

3.2.1 Numerical Approach of Two-wavelength Lidar Inversion Algorithm

The lower atmosphere is mixed with molecules and particles in an unknown proportion. The volume extinction coefficient, α , and volume backscatter coefficient, β , can be expressed as a combination based upon molecule and particle contributions,

$$\alpha = \alpha_m + \alpha_p, \quad (3.23)$$

$$\beta = \beta_m + \beta_p, \quad (3.24)$$

The two-wavelength lidar equations (3.8) and (3.9) can be expressed in terms of molecular and particle volume backscatter and extinction coefficients,

$$P_1(Z) = \frac{K_1}{Z^2} [\beta_{m_1}(Z) + \beta_{p_1}(Z)] e^{-2 \int_0^Z (\alpha_{m_1}(r) + \alpha_{p_1}(r)) dr}, \quad (3.25)$$

$$P_2(Z) = \frac{K_2}{Z^2} [\beta_{m_2}(Z) + \beta_{p_2}(Z)] e^{-2 \int_0^Z (\alpha_{m_2}(r) + \alpha_{p_2}(r)) dr}, \quad (3.26)$$

where, $K_1 = P_{L_1} A_l \zeta_1 \frac{c\tau}{2}$, $K_2 = P_{L_2} A_l \zeta_2 \frac{c\tau}{2}$,

and $\zeta_{1,2}$ are two-wavelength lidar system efficiencies at each wavelength. Because the relation between the particle extinction coefficient and particle backscatter coefficient is complicated and not unique, an empirical approximation is used. We take the relationship between the extinction and backscatter for particles to be,

$$\alpha_p = 8\pi\beta_p, \quad (3.27)$$

Instead of using the particle backscatter wavelength dependence, q , which we derived from the LADIMAS Campaign '91 measurements using Eq. 3.14, here we used an commonly accepted empirical approximation of q . This empirical approximation of the wavelength dependence of particle extinction coefficients, α_p , is derived from meteorological visibility [Camagni and Sandroin, 1984],

$$\alpha_p = 3.91 V^{-1} \left(\frac{550}{\lambda} \right)^q. \quad (3.28)$$

where, V is the meteorological visibility. The particle backscatter wavelength dependence, q , is

expressed as,

$$q = 0.0585V^{\frac{1}{3}} \text{ for } V \leq 6000 \text{ m,} \quad (3.29)$$

$$= 1.3 \text{ for average visibility.}$$

The relation between molecular extinction coefficient and backscatter coefficient has a factor of $8\pi/3$, and the molecular extinction wavelength dependence is λ^{-4} . From Eq. (3.27), (3.28) and (3.29), the empirical relation approximation between particle extinction coefficient and particle backscatter coefficient has a factor of 8π , and the extinction wavelength dependence of particle is $\lambda^{-1.3}$. From above assumptions about extinction coefficients and backscatter coefficients, the molecular backscatter cross-section gradient with unit height, $d\beta_{m2}(Z)/dZ$, and the particle backscatter cross-section gradient with unit height, $d\beta_{p2}(Z)/dZ$, are derived from Eq. (3.25) and (3.26) and written in the following two independent simultaneous equations,

$$\left(\frac{\lambda_2}{\lambda_1}\right)^4 \frac{d}{dZ} \beta_{m2}(Z) + \left(\frac{\lambda_2}{\lambda_1}\right)^{1.3} \frac{d}{dZ} \beta_{p2}(Z) = (A+B) * C, \quad (3.30)$$

$$\frac{d}{dZ} \beta_{m2}(Z) + \frac{d}{dZ} \beta_{p2}(Z) = (D + E) * F. \quad (3.31)$$

Here, the factors A, B, C, D, E, and F are group of calculation terms and have no physical meaning individually. They are,

$$A = \frac{1}{P_1(Z)} \frac{P_1(Z_1) - P_1(Z_2)}{dZ}, \quad (3.32)$$

$$B = \frac{16\pi}{3} \left[\left(\frac{\lambda_2}{\lambda_1}\right)^4 \beta_{m2}(Z) + 3 \left(\frac{\lambda_2}{\lambda_1}\right)^{1.3} \beta_{p2}(Z) \right], \quad (3.33)$$

$$C = \left(\frac{\lambda_2}{\lambda_1}\right)^4 \beta_{m_2}(Z) + \left(\frac{\lambda_2}{\lambda_1}\right)^{1.3} \beta_{p_2}(Z), \quad (3.34)$$

$$D = \frac{1}{P_2(Z)} \frac{P_2(Z_1) - P_2(Z_2)}{dZ}, \quad (3.35)$$

$$E = \frac{16\pi}{3} [\beta_{m_2}(Z) + 3\beta_{p_2}(Z)], \quad (3.36)$$

$$F = \beta_{m_2}(Z) + \beta_{p_2}(Z). \quad (3.37)$$

The Equations 3.30 and 3.31 contain only two unknowns, $d\beta_{m_2}(Z)/dZ$ and $d\beta_{p_2}(Z)/dZ$. From the profiles of the two-wavelength lidar measurements, we derived the molecular contribution to the lidar return at wavelength 2. Starting from an upper aerosol-free altitude Z_1 ($\beta_{a_2}(Z_1) = 0$), with a known molecular volume backscatter cross-section, β_{m_2} , the molecular volume backscatter cross-section at Z_2 , which is one step below Z_1 , is calculated from the gradient of the molecular volume backscatter cross-section profile as,

$$\beta_{m_2}(Z_2) = \beta_{m_2}(Z_1) + \frac{d}{dZ} \beta_{m_2}(Z) * (Z_1 - Z_2). \quad (3.38)$$

Since the molecular backscatter cross-section, σ_π , is known [Measures, 1992], the atmospheric molecular number density is calculated from the volume backscatter cross-section by,

$$\beta_\pi(\lambda) \equiv N\sigma_\pi(\lambda). \quad (3.39)$$

The two-wavelength lidar return profiles at 03:20 UT on 3 December 1991 are shown in Figure 3.6. The measured two-wavelength profiles were tied to model profiles at 39 km, and the profile of 355 nm was shifted from the return profile of 532 nm by a factor of 5.04, *ie.* $(532/355)^4$. The two-wavelength particle backscatter ratio (R_{12}) profile is shown on the right. Assuming there was only one kind of particle present throughout this layer, the R_{12} was constant within this

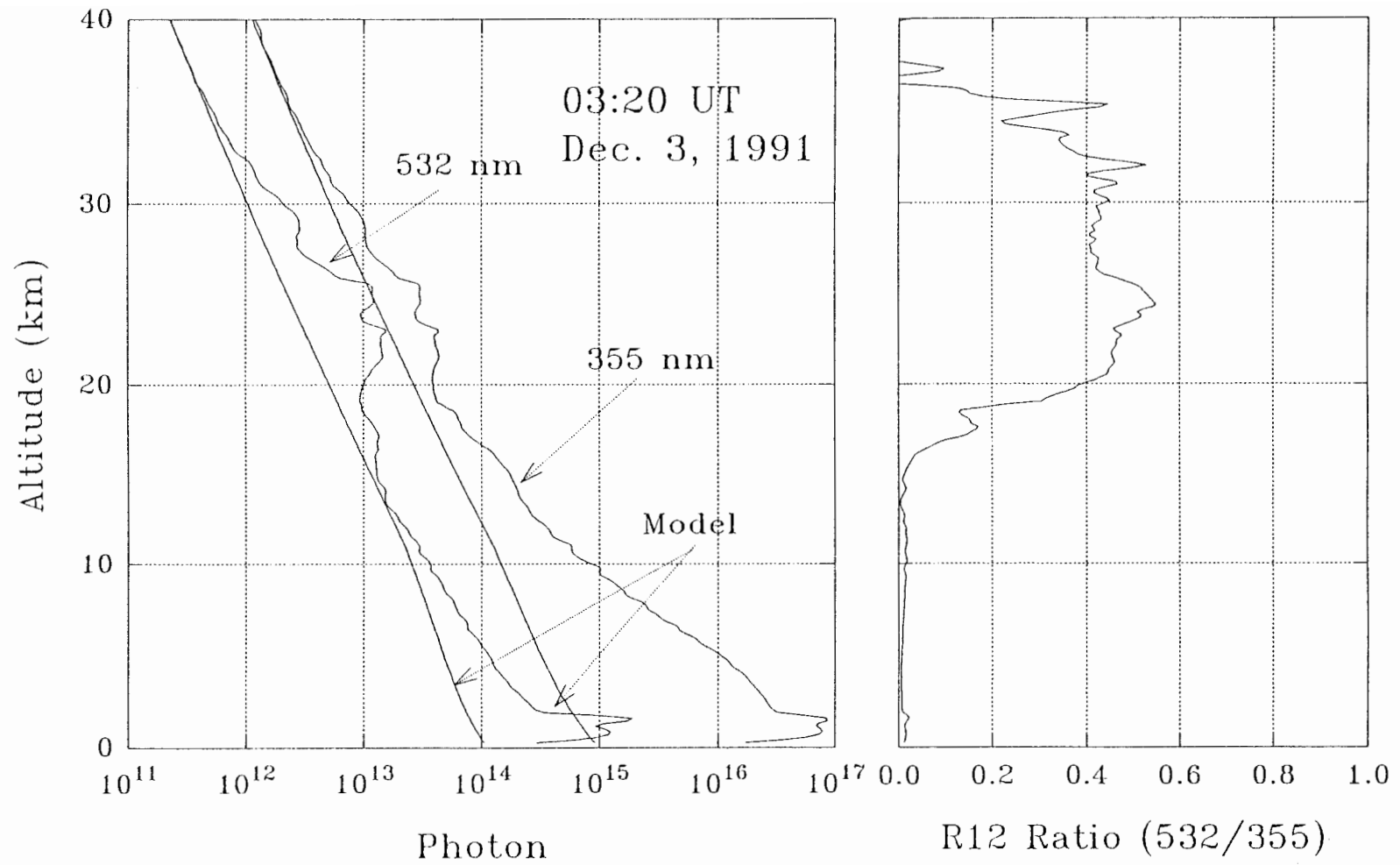


Figure 3.6. The two-wavelength lidar profiles and R_{12} profile measured at 03:20 UT on 3 December 1991 from ground to 40 km.

particle layer. The calculated molecular profiles at 355 nm in the altitude region from 15 to 40 km , based on the above closed-form two-wavelength lidar inversion algorithm, are shown in Figure 3.7, with wavelength dependence q changing from 1 to 1.7 to cover the statistical uncertainty of R_{12} . The stratospheric aerosol layer was distributed from 19 km to about 35 km , (see Figure 3.6). In Figure 3.7, it is obvious that the two-wavelength closed-form inversion can partially remove the stratospheric aerosol contribution of the lidar profile and can result in a relatively good return profile from 26 km to 40 km . Comparing with the R_{12} profile, on the right of Figure 3.6, there is a significant departure from a smooth profile in the altitude region from 23 km to 26 km . This feature could indicate that there was another type or independent group of particles present within this altitude region. With our assumption of a fixed wavelength dependence, q , over the whole particle layer, we could not separate all of the particle contribution from the stratospheric lidar profile.

In the interest of finding whether a different wavelength dependence, q , would better represent another group of particles in the altitude region from 23 to 26 km , we have considered a value of $q = 0.6$ for this stratospheric region, (see Figure 3.8). The calculated molecular return profiles were closer to the model return profile in that region, but we still could not remove the particle contribution totally. The uncertainty of the aerosol layer wavelength dependence, q , is the reason the closed-form solution of the two-wavelength lidar measurement could not provide the correct atmospheric density profile. Due to the wild change of density gradient, the temperature integration from this numerical closed-form approach is not presentable.

3.2.2 Two-wavelength Inversion Algorithm

If the stratospheric aerosol layer is dominated by one group of particles with a constant two-wavelength particle backscatter ratio, defined in Equation 3.12, the molecular portion of the

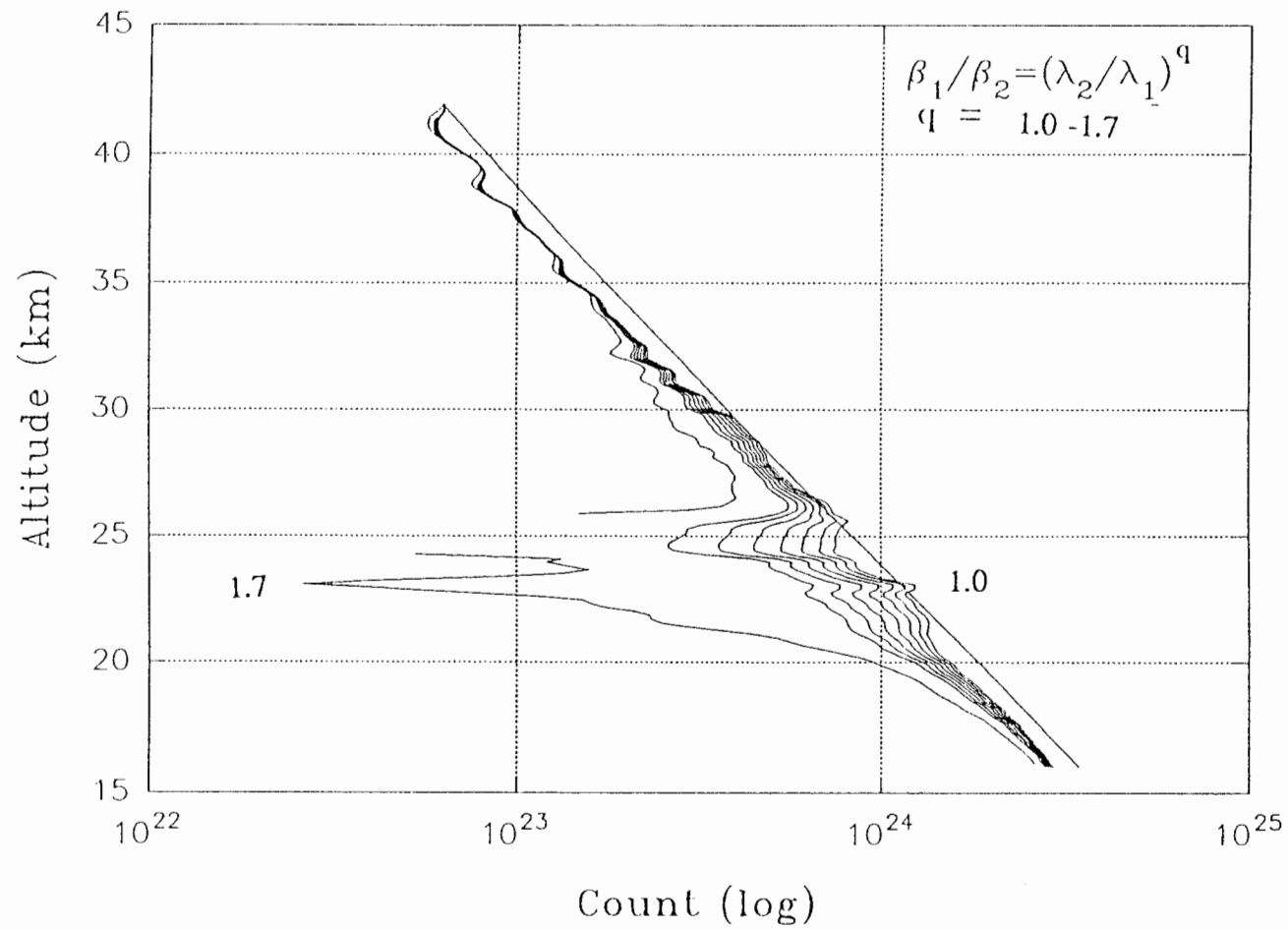


Figure 3.7. The molecular density profiles derived from two-wavelength lidar equations by assuming one size of particles at stratospheric volcanic aerosol layer.

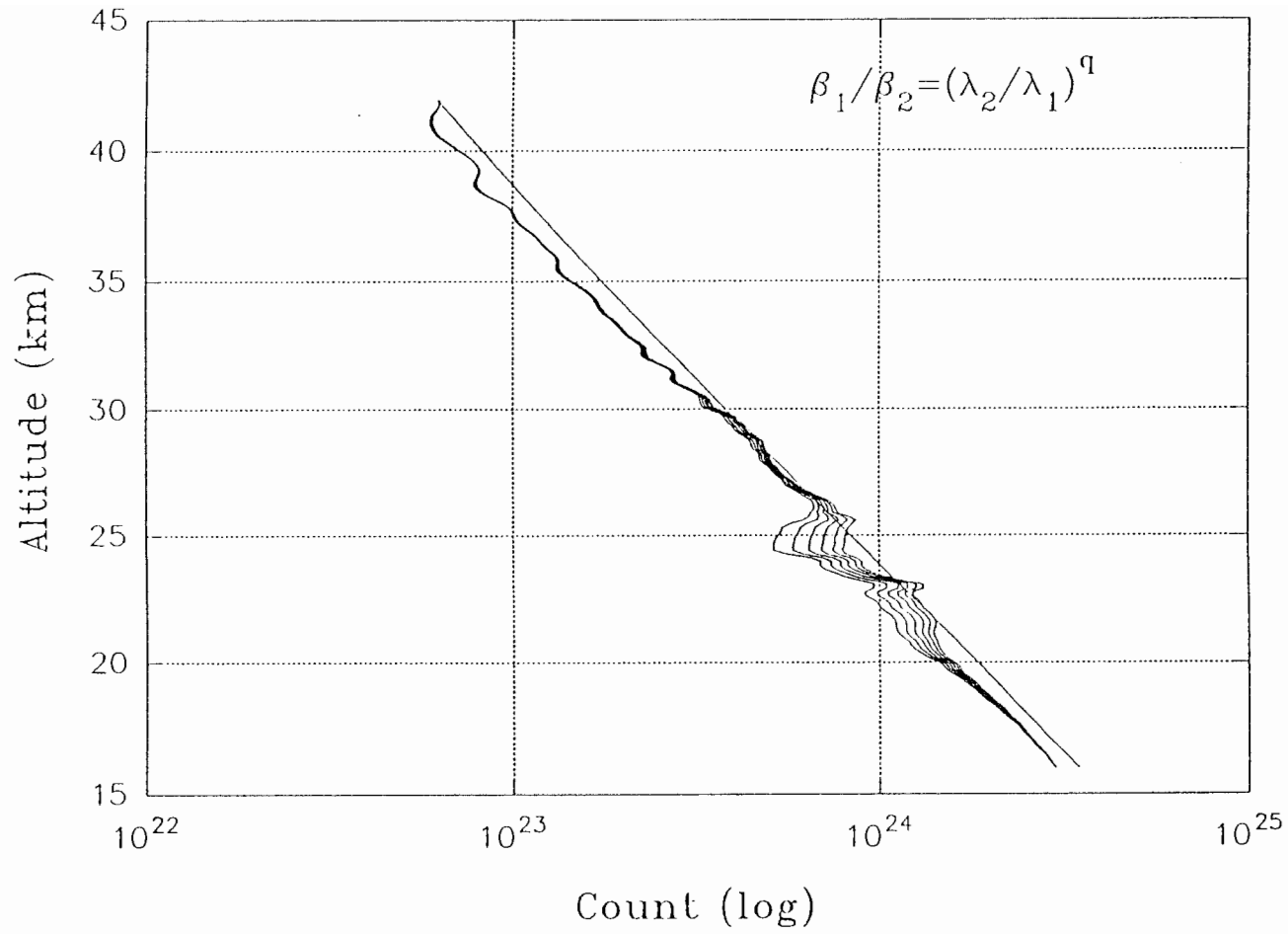


Figure 3.8. The molecular density profiles derived from two-wavelength lidar equations by letting the wavelength dependence q fixed at 0.6 in the altitude range 23 to 26 km, and changing from 1 to 1.5 otherwise.

lidar signal can be derived from the two-wavelength lidar measurements. In this case, the total signal profiles of 355 nm and 532 nm are expressed as B_{T355} and B_{T532} respectively, including particle and molecular contributions. The corresponding return signals from molecules are B_{M355} and B_{M532} . The two-wavelength particle backscatter ratio can be expressed in terms of B_{T532} , B_{T355} , B_{M532} , and B_{M355} as,

$$R_{12} \equiv \frac{B_{T532} - B_{M532}}{B_{T355} - B_{M355}} \quad (3.40)$$

In this approach, we assume the two-wavelength particle backscatter ratio R_{12} at the stratospheric aerosol layer is known as a mean value, a , from previous measurements, i.e. let a represent an average value throughout the stratospheric aerosol layers,

$$a \triangleq \overline{R_{12}} \Big|_{\text{aerosol layers}} \quad (3.41)$$

The ratio of the molecular portion of the returned signals from both wavelengths is defined as,

$$b \equiv \frac{B_{M355}}{B_{M532}} = \left(\frac{532}{355}\right)^4 \quad (3.42)$$

Equation (3.40) can be expressed as,

$$B_{T532} - B_{M532} = a \cdot (B_{T355} - b \cdot B_{M355}) \quad (3.43)$$

The molecular portion of the returned signal at 532 nm wavelengths, B_{M532} , is derived as,

$$B_{M532} = \frac{a \cdot B_{T355} - B_{T532}}{(a \cdot b - 1)} \quad (3.44)$$

The density, density ratio, and temperature profiles at 22:00 UT on 22 November, 03:20 UT and 05:28 UT on 3 December, which were calculated from Equation (3.44), are shown in Figures 3.9, 3.10, and 3.11 with corresponding R_{12} profiles shown on the far right. The two-wavelength particle backscatter ratio used is the mean value over the stratospheric aerosol layer. The range

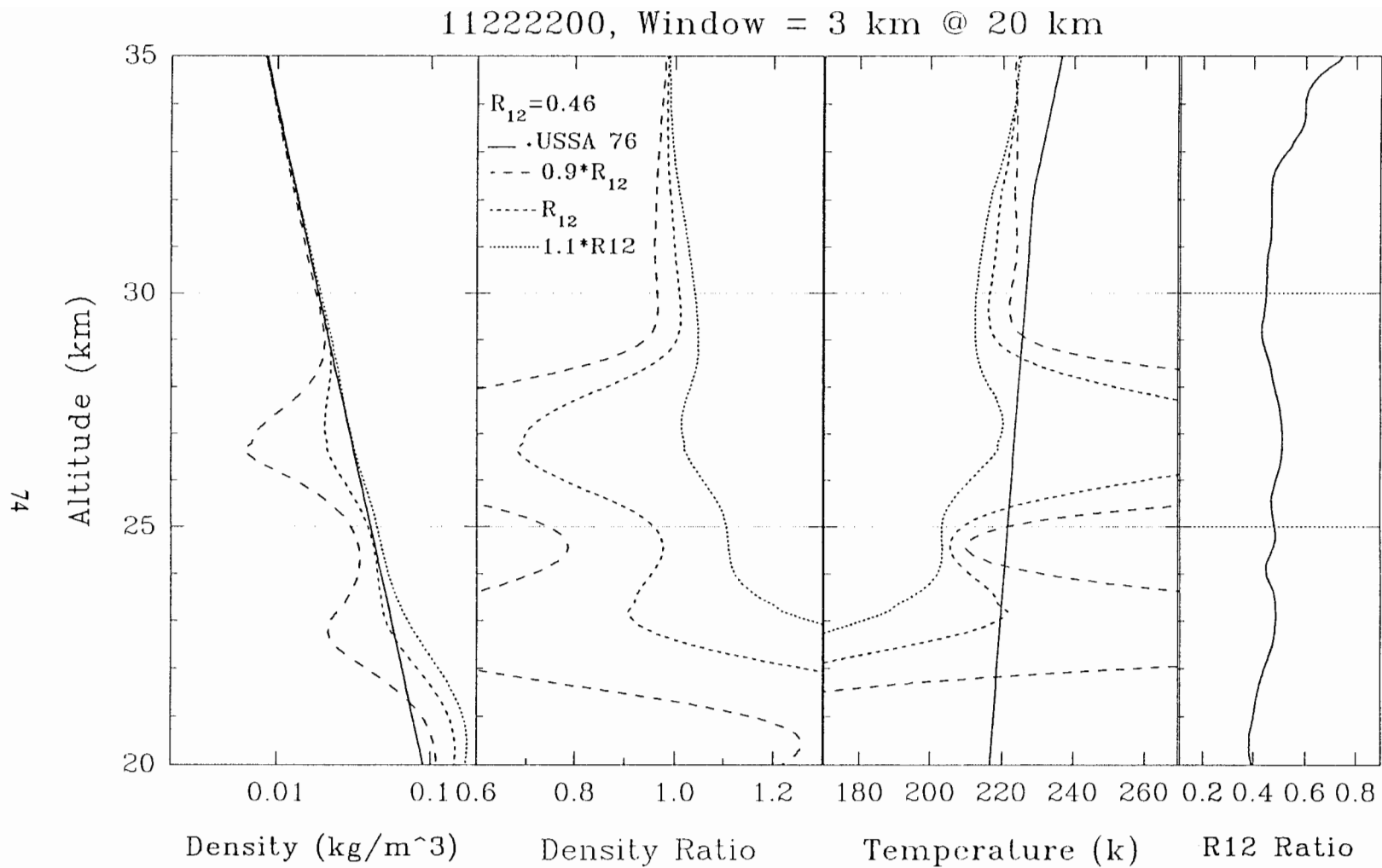


Figure 3.9. The two-wavelength lidar derived density, density ratio, and temperature profiles with corresponding R_{12} profile measured at 22:00 UT on 22 November 1991.

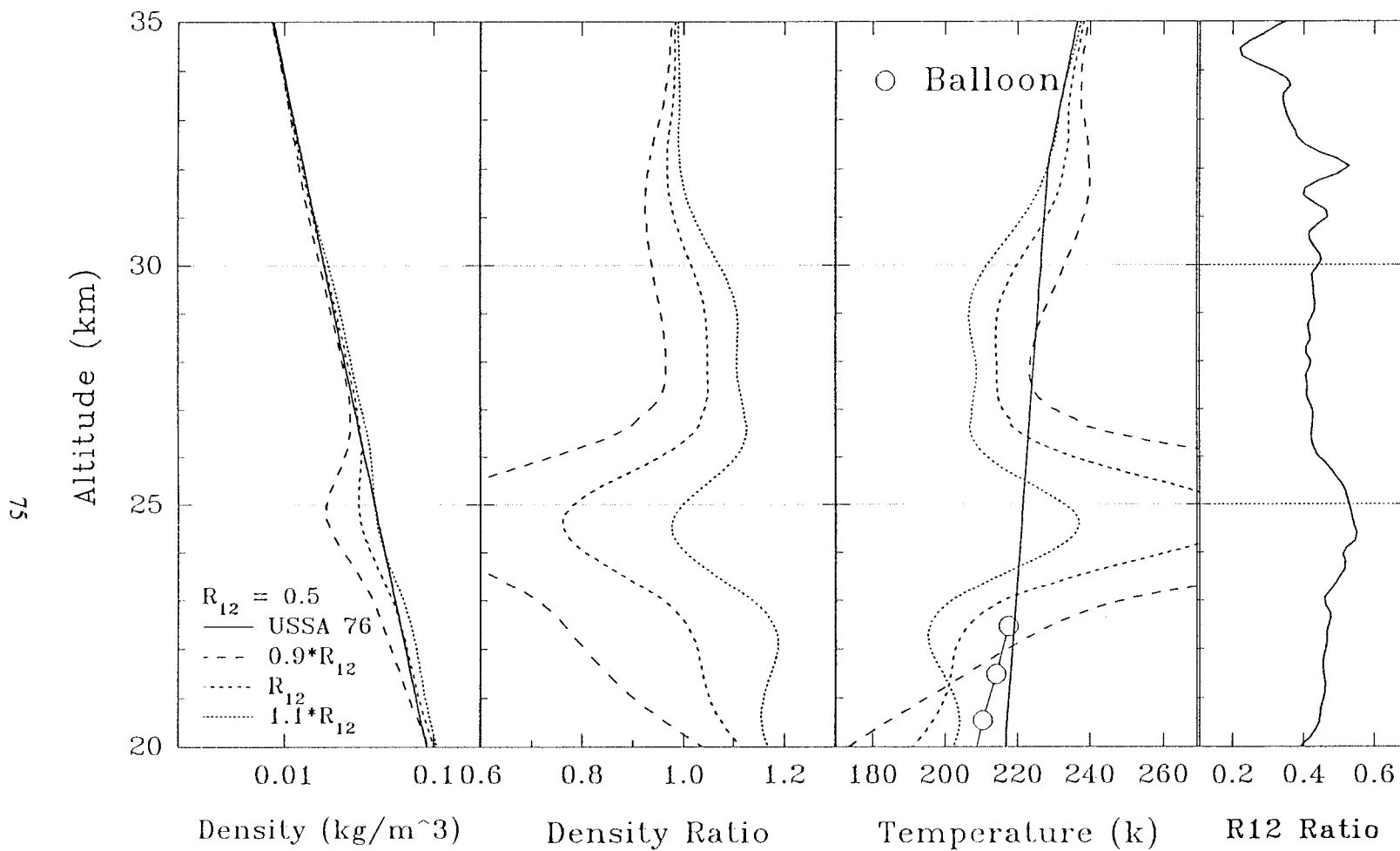


Figure 3.10. The two-wavelength lidar derived density, density ratio, and temperature profiles with corresponding R_{12} profile measured at 3:20 UT on 3 December 1991.

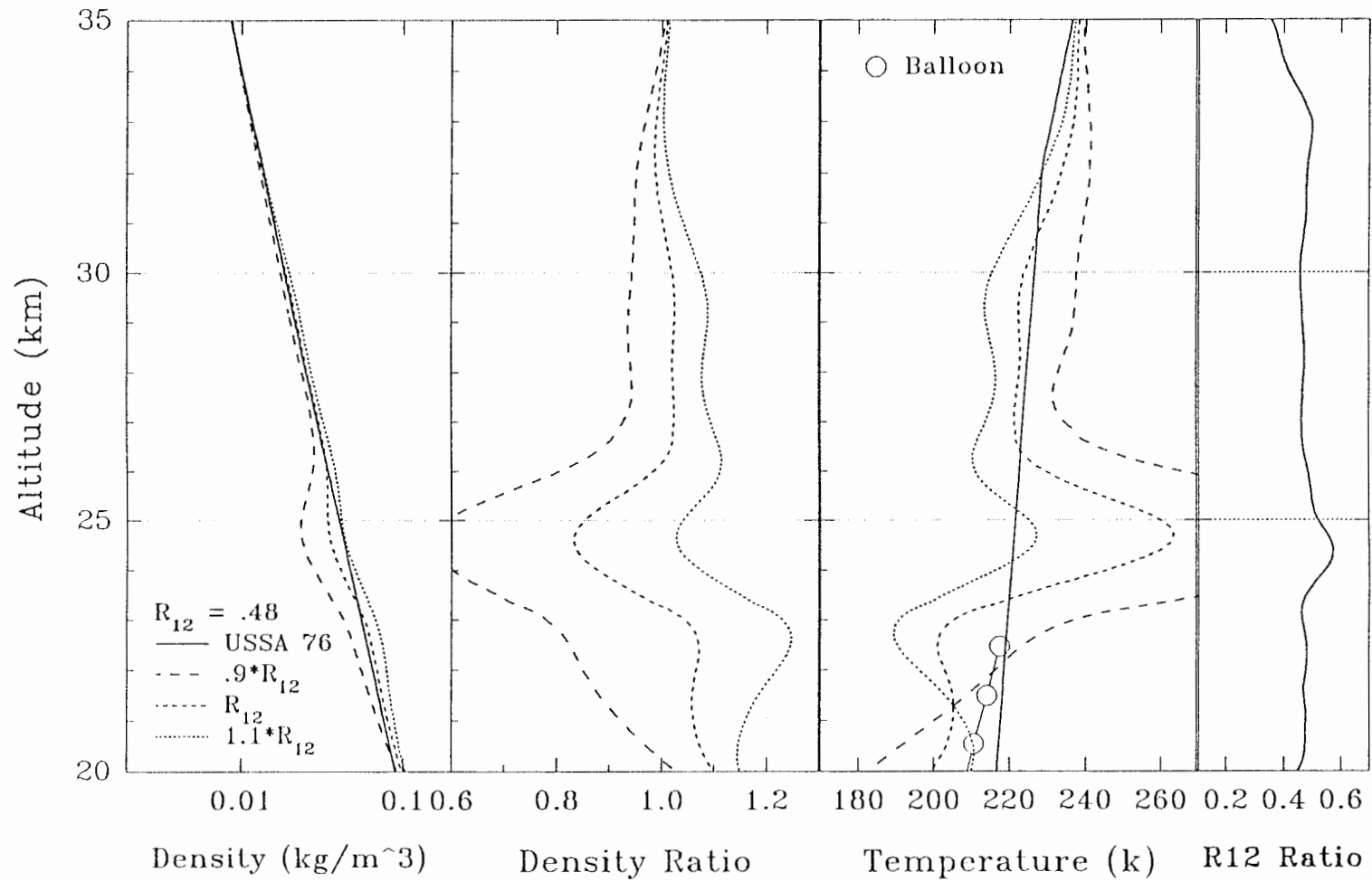


Figure 3.11. The two-wavelength lidar derived density, density ratio, and temperature profiles with corresponding R_{12} profile measured at 5:28 UT on 3 December 1991.

of $\pm 10\%$ around the mean value of a are shown for comparison of the variations associate with the uncertainty of the R_{12} value calculation. The corresponding two-wavelength lidar profiles and two-wavelength particle backscatter ratio profile can be used to retrieve the molecular portion of the returned signal by using a constant R_{12} value in the upper part of the stratospheric aerosol layer, above 27 km , until the value of two-wavelength particle backscatter ratio changes. On the night of 3 December 1992, a bump appeared on the R_{12} profiles around 24 to 25 km . This bump is probably due to another group of particles with different size or properties. The consecutive two-wavelength particle backscatter ratio profiles on 3 December 1991 are shown in Figure 3.12, where the bump at 24 km was present on all profiles. On the next day, 4 December 1992, a similar feature was observed at about 20 km . The changes in the two-wavelength particle backscatter ratio profile severely limit the usefulness of the two-wavelength inversion for stratospheric density and temperature measurements.

3.3 Summary of Chapter

In this chapter, we have discussed the applicability of using two-wavelength lidar to measure atmospheric properties. The different wavelength dependencies of the molecular and particle backscattering cross-sections provides additional information that makes the two-wavelength lidar valuable as a diagnostic tool to describe where the atmosphere is aerosol-free and molecular scatter analysis can be applied. Single-wavelength Rayleigh lidar can be used to probe the atmosphere at upper stratospheric altitudes but cannot detect whether particles are present in the region and where the analysis is valid.

The two-wavelength particle backscatter ratio (R_{12}), which we defined in Equation 3.12, provides a way to study atmospheric particle distribution by using multi-wavelength lidar. From this ratio, the wavelength dependence of the particle scattering cross-section is inferred. This ratio

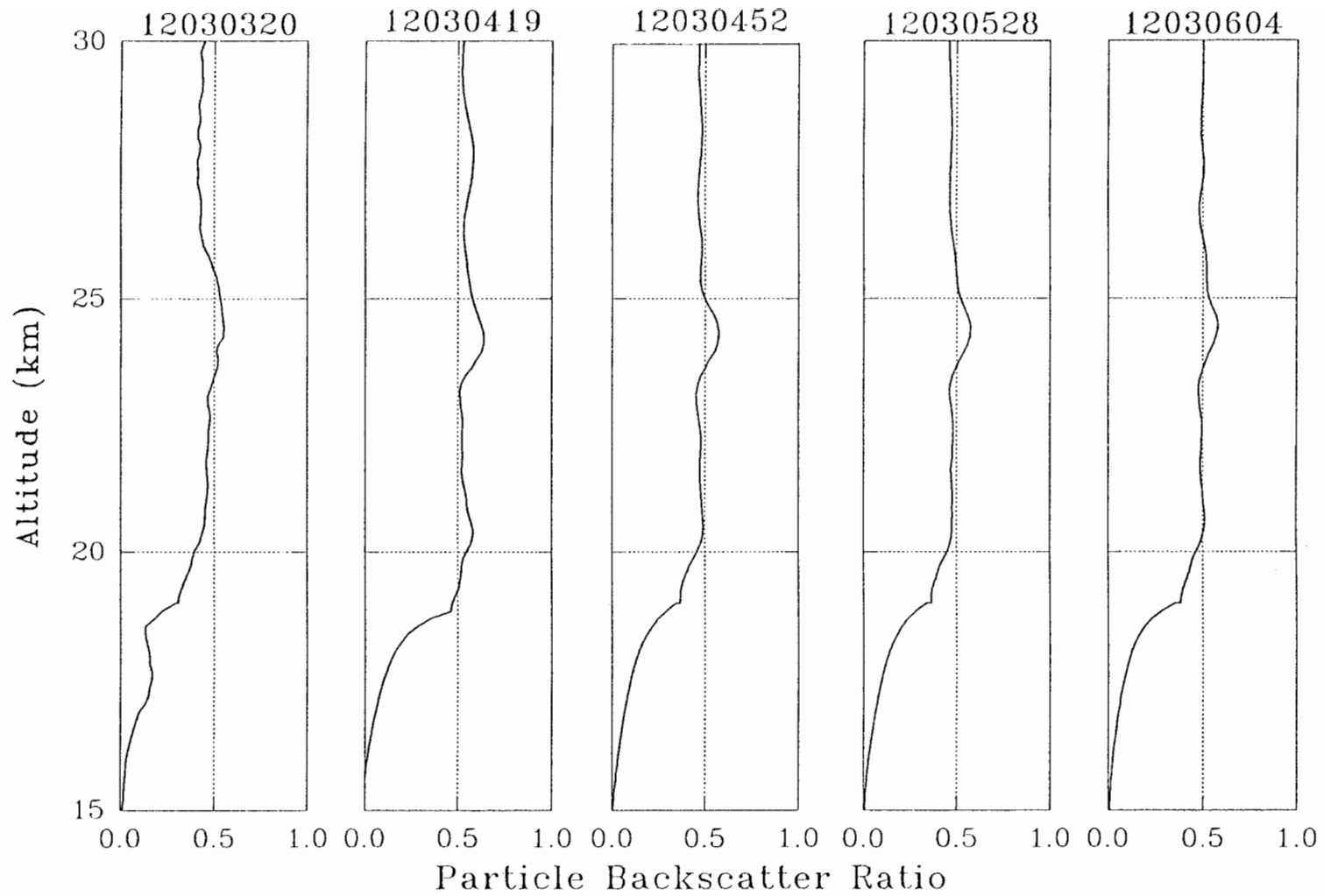


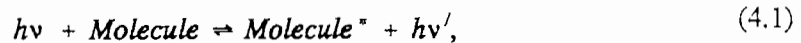
Figure 3.12. The consecutive two-wavelength particle backscatter ratio (R_{12}) profiles measured on 3 December 1991.

was almost a constant in the lower stratospheric aerosol layer but it was not at all constant in the tropospheric cloud layers. A constant value of two-wavelength particle backscatter ratio represents a group of particles with the same characteristics, such as, size, shape, and composition. The two-wavelength backscatter ratio value of the volcanic particle layer in the 20 to 30 *km* altitude range was around 0.5 about five months after the Pinatubo volcanic eruption, and it was about 0.25 nine months after the eruption. From the R_{12} profiles, we observed the settling of the Pinatubo volcanic particles into the lower stratospheric layer. Two different approaches for analyzing two-wavelength lidar data for atmospheric properties, density and temperature, were tried. Due to the presence of more than one particles type in the stratosphere, the two-wavelength lidar has limited use for the inversion of atmospheric properties in this region.

Chapter 4

ATMOSPHERIC PROFILING USING THE RAMAN TECHNIQUE

Raman scattering is one kind of molecular scattering process primarily characterized by the fact that the scattered radiation is frequency-shifted from the incident radiation. The shifted frequency amount corresponds to the energy level spacings in the scattering molecule. Frequency-shifted scattering is, of course, an inelastic scattering process. Raman scattered wavelengths may generally be regarded as the result of an impinging light quantum of a frequency, ν , exchanging energy with a molecule by the following scheme,



where h is the Planck's constant. The impinging light quantum is scattered with an altered frequency, ν' .

Raman lidar operates much as an ordinary lidar except that the detector is designed to measure the inelastic Raman vibrational or rotational scattered radiation components of the atmospheric N_2 , O_2 , or some other species. By measuring both the frequency-shifted Raman scattering return of N_2 and the unshifted Rayleigh return (*i.e.* the centered "Q-branch," $\Delta J = 0$) of the lidar profiles, we can separate the signals that are due to molecules from those that result from particles in the atmosphere. Such Raman scattering measurements provide another technique in laser remote sensing because they can identify and quantify a trace constituent in the background of the major constituents of a mixed atmosphere.

In this chapter, we discuss the measurements of tropospheric density and temperature profiles using frequency-shifted Raman nitrogen vibrational-rotational components. The Penn State LAMP lidar system measures the backscatter signals at several wavelengths. Using a Nd:YAG laser source with output wavelength at 532 nm , the nitrogen Raman vibrational first

Stokes lines at 607 nm can be used to determine the atmospheric extinction profile.

4.1 Raman Scattering Process

In Raman scattering, the magnitude of the wavelength shift of the scattered photon provides a unique signature of the scattering molecular species. This frequency shift is independent of the incident laser wavelength and corresponds to the vibrational energy states of these molecular species. Raman scattering returns from the atmosphere are quite insensitive to the presence of particles except for their atmospheric extinction. By using both the frequency-shifted Raman return signal and the signal at the fundamental laser wavelength, we can separate the atmospheric scattering signal due to uniformly mixed gas molecules, such as N_2 , from the combined signal due to other molecules and particles. In principle, we can use Raman lidar to determine each constituent density because the backscattering differential cross-section, $d\sigma/d\Omega$, is known either experimentally or theoretically.

4.1.1 Stokes and Anti-Stokes Raman Lines

Spectral analysis of a scattered wave reveals a series of sideband frequencies, ν_r . Those sideband frequencies are shifted down and up by an amount equal to the irradiated molecule's vibrational frequency, $\Delta\nu_r$. The lower frequencies are *Stokes* lines when the molecule gains energy from the radiation field. If the molecule loses energy to the radiation field, the higher radiated frequency components are *anti-Stokes* lines. These can be expressed by the following equation,

$$\nu_r = \nu_0 \pm \Delta\nu_r, \quad (4.2)$$

where ν_0 is the frequency of the incident wave. The Stokes lines, $\nu_0 - \Delta\nu_r$, generally have a

higher intensity than the anti-Stokes lines, $\nu_0 + \Delta\nu_r$. In fact, the simple molecules of the atmosphere such as N_2 , O_2 , etc. have such large energy shifts between vibrational states that the anti-Stokes lines are never populated at normal atmospheric temperature. The Raman vibrational scattering processes are schematically illustrated in Figure 4.1. The first Stokes lines are at a significant distance from the fundamental frequency. So, these first Stokes lines can be easily separated with a proper filter. The respective first Stokes lines of O_2 , N_2 and H_2O at excitation wavelengths of 532 nm, 355 nm, and 266 nm as observed by the Penn State Lamp lidar system, are shown in Table V.

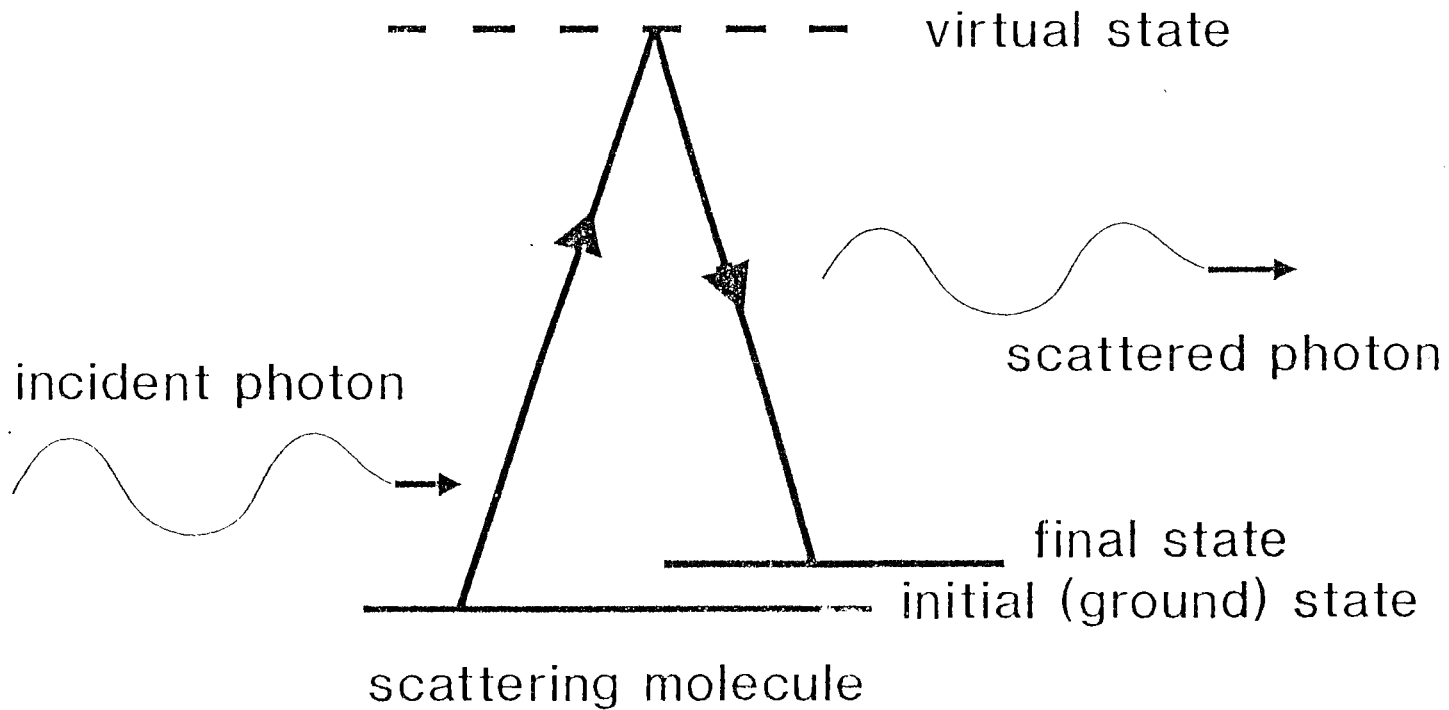
Table V. First Stokes Lines of O_2 , N_2 and H_2O			
Fundamental Wavelength (nm)	Raman O_2 (nm)	Raman N_2 (nm)	Raman H_2O (nm)
532	580	607	660
355	376	387	408
266	277	284	295

4.1.2 Vibrational Raman Scattering

The structure of the $\nu = 0$ to 1 nitrogen vibrational-rotational band is well known [Inaba, 1976]. It consists of a strong Q -branch, where the intensity is independent of temperature, together with Stokes and anti-Stokes rotational lines forming envelopes on either side of the Q -branch. The Stokes and anti-Stokes rotational lines together contribute about 20% of the total band intensity. The intensities of individual lines vary with temperature, but their integrated total

RAMAN SCATTERING

(INELASTIC PHOTON SCATTERING)



83

Figure 4.1. Schematic representation of Raman vibrational Stokes scattering.

energy does not. The theoretical distribution of the Raman nitrogen rotational spectrum is shown in Figure 4.2 [Inaba and Kobayasi, 1972] for the first Stokes vibrational state. This corresponds to the first Stokes shift spectrum of the N_2 molecule at 300 K with the frequency shifted by 2330.7 cm^{-1} from the emitted frequency.

Figure 4.3 illustrates the backscatter cross-section of the Rayleigh and Raman returns of O_2 , N_2 , and H_2O from an ordinary atmosphere with the laser emission centered at 532 nm. The backscattered laser radiation distribution consists of a narrow band aerosol signal which is superimposed upon a temperature Doppler broadened signal due to backscatter by molecules. The injection seeded laser has a line width of 80 MHz, which is not significantly broadened by the particle Doppler velocity, but the molecular scatter is Doppler broadened to about 1.3 GHz at room temperature. Due to the narrow width of particle scattering frequency, this particle backscatter spectrum corresponds to the linewidth of the laser, which is about 80 MHz. Figure 4.3 also shows Rayleigh and Raman rotational scattering by the molecules. In the figure, vibrational-rotational Raman lines of N_2 , O_2 , and H_2O are indicated with thermal broadening lines. When the atmosphere is excited by a doubled Nd:YAG laser of 532 nm wavelength, the center of the shifted spectrum is at 607 nm for N_2 , at 587 nm for O_2 , and at 660 nm for water vapor (H_2O). The absolute density of each molecular species is estimated by comparing its Raman backscatter intensity with the Raman scattering intensity from N_2 or O_2 molecules which occupy the same volume and which are assumed to be of known concentration and density.

4.1.3 Rotational Raman Scattering

The Raman rotational spectrum consists of two branches, an O (anti-Stokes) branch and an S (Stokes) branch of approximately equal amplitude. These two branches locate symmetrically on the frequency axis on each side of the Cabannes line, Figure 4.4. This molecular rotational

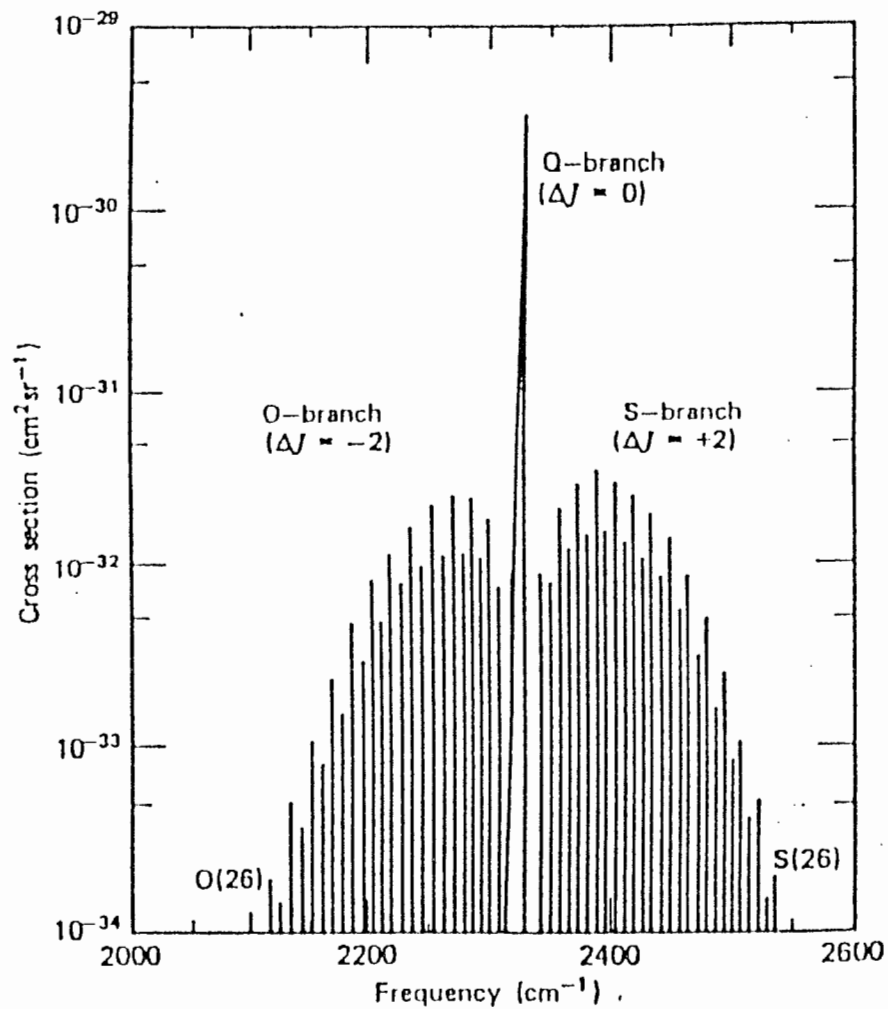


Figure 4.2. The theoretical distribution of vibrational-rotational Raman spectrum ($\nu = 0$ to 1 vibrational transition) at 300 K (after Inaba, 1972).

MOLECULAR RAMAN SHIFT FROM 532 NM

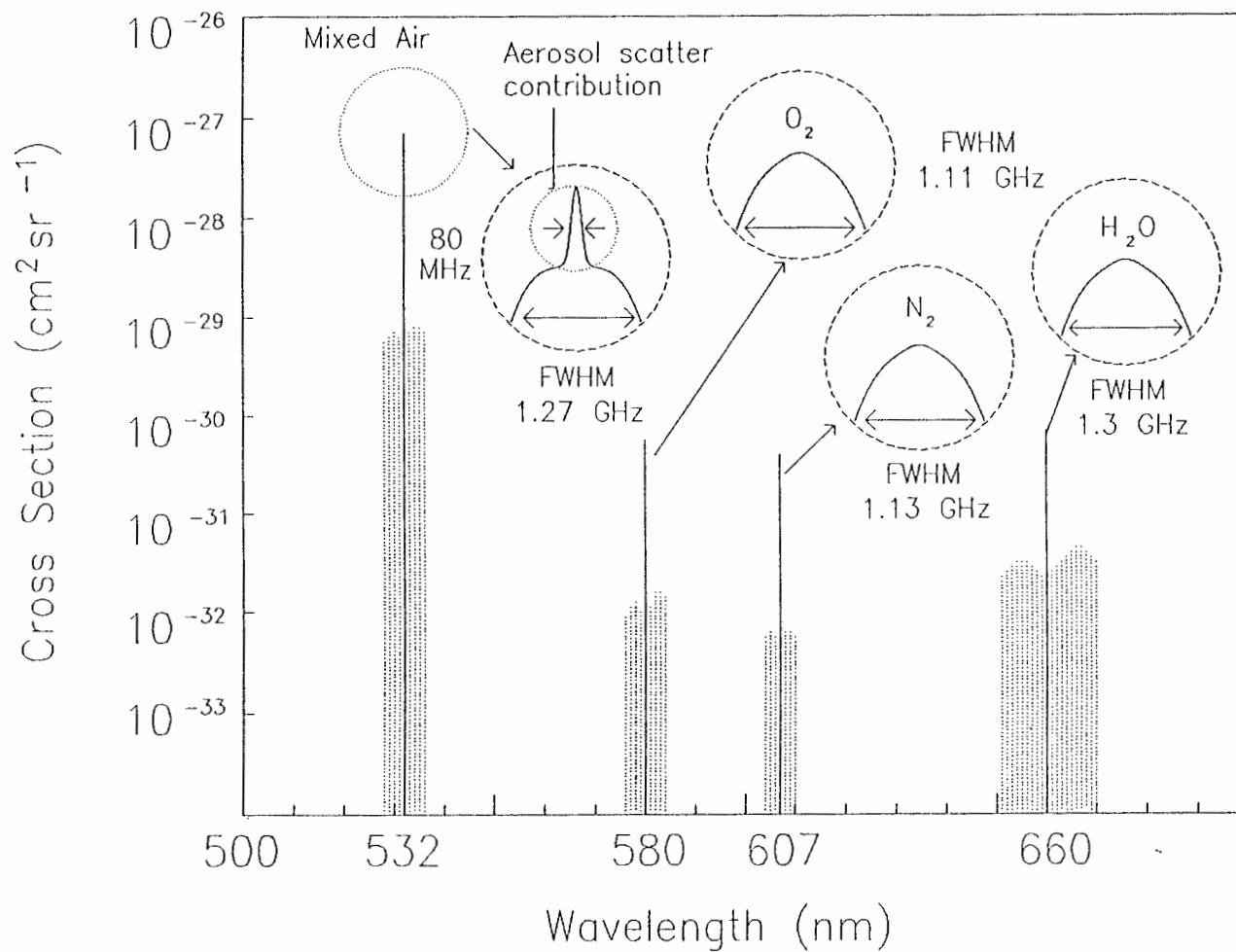


Figure 4.3. The molecular Raman shifted from 532 nm of N_2 , O_2 , and H_2O .

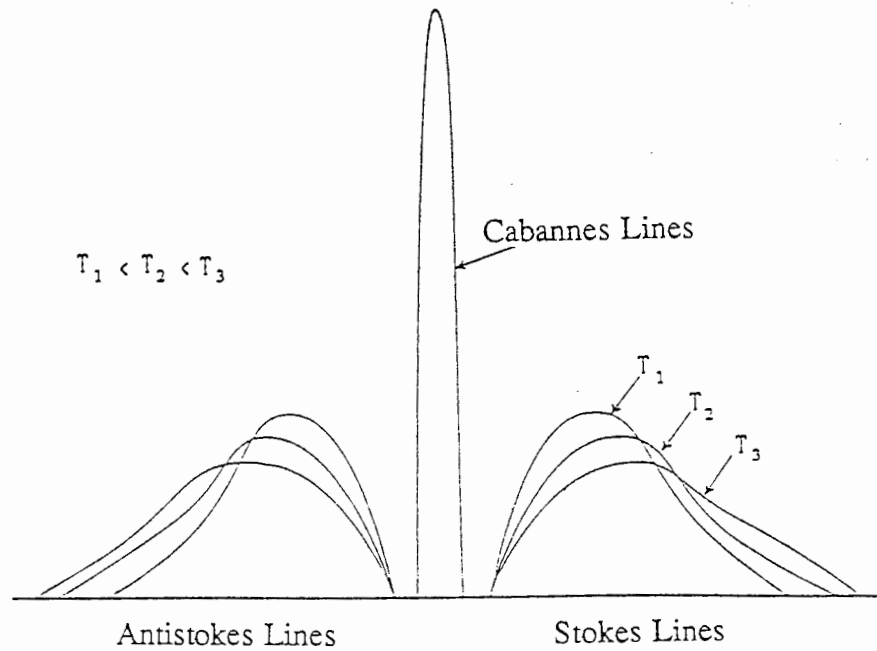


Figure 4.4. Envelop of the rotational Raman spectrum. The Raman rotational spectral envelop changes shape as a function of temperature.

Raman spectral envelope changes shape as a function of temperature. The envelope of spectral lines reflects the temperature dependence of rotational energy level population. By measuring the intensity ratio between two parts of the rotational Raman band, one can infer the atmospheric temperature free of the effect of atmospheric attenuation. Cooney [1972] measured temperature profiles up to 2 km by analyzing the backscattered nitrogen Raman rotational spectrum. His lidar used a ruby laser transmitter at 694 nm wavelength and interference filters to select spectral regions. In the rotational Raman atmospheric measurements, rotational Raman scattering of molecular oxygen also contributes to the measurement. Using the anti-Stokes rotational lines of the N₂ and O₂ Raman spectrum, Nedeljkovic *et al.* [1993] measured the temperature profile directly for altitudes between 10 and 30 km.

Using the N₂ vibrational Raman scattering signal, we are able to measure the attenuation

of the atmosphere. This atmospheric attenuation is generally different at both the emitted and backscattered wavelengths. Thus, an atmospheric transmission measurement at more than one wavelength is important for the vibrational Raman lidar technique. Compared to the vibrational Raman lidar, the rotational Raman lidar technique provides a direct temperature measurement which is essentially independent of atmospheric transmission.

4.2 Raman Lidar Measurements of Optical Properties

A major difficulty in the interpretation of pulsed lidar backscatter data is that the atmospheric transmittance cannot be easily evaluated from the received laser backscatter intensity. Prior information concerning the relationship between the backscatter coefficient and the extinction coefficient is necessary to evaluate the atmospheric transmittance from lidar measurements [Leonard and Caputo, 1974]. The backscatter coefficient for Raman scattering, however, depends only on the Raman cross-section and number density of the specific molecule. In the lower atmosphere, below *100 km*, the fraction of nitrogen in the atmosphere is constant. The collected Raman signal at *607 nm*, from excitation of *532 nm* (doubled Nd:YAG), is proportional to the nitrogen number density, except the signal has been attenuated by the atmospheric transmission loss.

4.2.1 Using Raman Techniques to Measure Extinction Coefficients and Atmospheric Transmission

The received power in a Raman lidar measurement from the atmospheric scatterer at altitude *Z* is described by the Raman lidar equation,

$$P_r(Z) = P_L \frac{A_r}{Z^2} \xi \beta(Z) \frac{c\tau}{2} \mathcal{T}(v_o) \mathcal{T}(v_r), \quad (4.3)$$

where,

$\beta(Z)$ is the molecular volume backscattering coefficient at altitude Z ,

$\mathcal{T}(v_o)$ is the atmospheric transmittance at the transmitted frequency v_o ,

$\mathcal{T}(v_r)$ is the atmospheric transmittance at the received frequency v_r .

The other parameters are the same as those in the molecular (Rayleigh) lidar equation, Eq. 2.1.

The difference between this and the molecular (Rayleigh) lidar equation (Eq. 2.1), is that the transmitted and received frequencies, v_o and v_r , are different.

The Raman lidar equation, Eq. 4.3, which describes the Raman signal return from molecular scatter at an altitude Z , can be expressed as,

$$P(Z) = \frac{K}{Z^2} \beta(Z) \exp\left\{-\int_0^Z [\sigma(\lambda_L, r) + \sigma(\lambda_R, r)] dr\right\}, \quad (4.4)$$

where, $P(Z)$ is the signal received from altitude Z , the system coefficient K includes all of the system constants which are distance independent, $\beta(Z)$ is the volume Raman backscatter coefficient, and $\sigma(\lambda_L, r)$ and $\sigma(\lambda_R, r)$ are the volume extinction coefficients at the emitted and returned wavelengths, respectively. Rearranging terms, the Raman lidar equation can be expressed as,

$$\exp\left\{\int_0^Z [\sigma(\lambda_L, r) + \sigma(\lambda_R, r)] dr\right\} = \frac{K\beta(Z)}{Z^2 P(Z)}. \quad (4.5)$$

A widely used signal variable is the logarithmic range-adjusted power $S(r)$, which is defined as,

$$S(Z) = \ln[Z^2 P(Z)]. \quad (4.6)$$

Taking logarithms of both side of Equation (4.5), the Raman lidar equation becomes,

$$\int_0^Z [\sigma(\lambda_L r) + \sigma(\lambda_R r)] dr = \ln K + \ln \left[\frac{\beta(Z)}{Z^2 P(Z)} \right]. \quad (4.7)$$

The differential equation corresponding to the above Raman lidar equation is,

$$\begin{aligned} \sigma(\lambda_L Z) + \sigma(\lambda_R Z) &= \frac{d}{dZ} \left[\ln \frac{\beta(Z)}{Z^2 P(Z)} \right], \\ &= \frac{d}{dZ} \ln \beta(Z) - \frac{d}{dZ} \ln [Z^2 P(Z)], \\ &= \frac{d}{dZ} \ln \beta(Z) - \frac{d}{dZ} S(Z). \end{aligned} \quad (4.8)$$

Two volume extinction coefficients, $\sigma(\lambda_L)$ and $\sigma(\lambda_R)$, due to molecular extinction and particle extinction can be expressed as,

$$\sigma(\lambda_L) = \sigma_m(\lambda_L) + \sigma_p(\lambda_L), \quad (4.9)$$

and,

$$\sigma(\lambda_R) = \sigma_m(\lambda_R) + \sigma_p(\lambda_R), \quad (4.10)$$

respectively. Then the differential equation Eq. 4.8 becomes,

$$\sigma_m(\lambda_L) + \sigma_p(\lambda_L) + \sigma_m(\lambda_R) + \sigma_p(\lambda_R) = \frac{d}{dZ} \ln \beta(z) - \frac{d}{dZ} S(z). \quad (4.11)$$

Rearranging terms of the above equation, the sum of the aerosol extinction coefficient through the entire laser beam path, $\sigma_p(\lambda_L) + \sigma_p(\lambda_R)$, becomes,

$$\sigma_p(\lambda_L) + \sigma_p(\lambda_R) = \frac{d}{dZ} \ln \beta(Z) - \frac{d}{dZ} S(Z) - \sigma_m(\lambda_L) - \sigma_m(\lambda_R). \quad (4.12)$$

The wavelength dependence of particle extinction coefficients is λ^{-q} , where $0.7 < q < 1.9$ for tropospheric particles. Here, we chose $q = 1$ which is reasonable assumption for tropospheric particles [Ansmann et al., 1990]. The wavelength dependence of the molecular extinction coefficients is λ^{-4} . From equation (4.12) and the wavelength dependence of particle and molecule,

the particle extinction coefficient at the laser emitted wavelength is expressed as,

$$\sigma_p(\lambda_L) = \frac{\frac{d}{dz} \ln \beta(z) - \frac{d}{dz} S(z) - [\sigma_m(\lambda_L)(1 + (\frac{\lambda_L}{\lambda_R})^4)]}{[1 + (\frac{\lambda_L}{\lambda_R})^q]} \quad (4.13)$$

The initial value of the volume Raman backscattering coefficient, $\beta(z)$, and the volume extinction coefficient, $\sigma_m(\lambda_L)$, are based on the density profile from the U.S. Standard model, 1976, as,

$$\sigma_m = N(z) * \frac{8\pi}{3} * 5.45 * 10^{-32} * [\frac{550}{\lambda(nm)}]^4 \quad m^{-1}, \quad (4.14)$$

and,

$$\beta = N(z) \sigma_{\pi}^{Raman}. \quad (4.15)$$

The differential form of $\ln \beta(Z)$ is,

$$\begin{aligned} \frac{d}{dz} \ln \beta(z) &= \frac{d}{dz} [\ln N(z) + \ln \sigma_{\pi}^{Raman}] \\ &= \frac{d}{dz} \ln N(z), \end{aligned} \quad (4.16)$$

where, the molecular volume backscattering extinction coefficient does not change with altitude.

From equation (4.13), the particle extinction coefficient at the emitted wavelength can be written as,

$$\sigma_p(\lambda_L) = \frac{\frac{d}{dz} \ln N(z) - \frac{d}{dz} S(z) - \sigma_m(\lambda_L)[1 + (\frac{\lambda_L}{\lambda_R})^4]}{[1 + (\frac{\lambda_L}{\lambda_R})^q]} \quad (4.17)$$

In this expression, the molecular number density, $N(Z)$, and the molecular extinction coefficient, $\sigma(\lambda_L)$, are calculated from a model. From the particle and molecular extinction

coefficients at the emitted laser wavelength, we can calculate the corresponding extinction coefficients at the Raman return wavelength,

$$\sigma_p(\lambda_R) = \sigma_p(\lambda_L) \left(\frac{\lambda_L}{\lambda_R} \right)^q, \quad (4.18)$$

$$\sigma_m(\lambda_R) = \sigma_m(\lambda_L) \left(\frac{\lambda_L}{\lambda_R} \right)^4. \quad (4.19)$$

The two-way particle and molecular extinction coefficient profiles are,

$$\begin{aligned} \sigma_p &= \sigma_p(\lambda_L) + \sigma_p(\lambda_R) \\ &= \sigma_p(\lambda_L) \left[1 + \left(\frac{\lambda_L}{\lambda_R} \right)^q \right], \end{aligned} \quad (4.20)$$

and

$$\begin{aligned} \sigma_m &= \sigma_m(\lambda_L) + \sigma_m(\lambda_R) \\ &= \sigma_m(\lambda_L) \left[1 + \left(\frac{\lambda_L}{\lambda_R} \right)^4 \right], \end{aligned} \quad (4.21)$$

respectively. Using these defined extinction coefficients, the two-way transmittance profile of Raman lidar measurement, $T^2(z)$ is,

$$T^2(z) = \exp \left\{ - \int_0^z (\sigma_p(r) + \sigma_m(r)) dr \right\}. \quad (4.22)$$

The extinction coefficient and transmission profiles calculated from the 607 nm N_2 Raman return signal on the night of 22 November 1991 are shown in Figure 4.5. Those regions where the extinction coefficient was negative are probably due to system noise. This technique is very sensitive to slope changes such as those observed on the original range-corrected Raman signal profile, the dashed line in Figure 4.6. The solid line in Figure 4.6 is the transmission-corrected Raman profile which represents the atmospheric molecular response. The sky was mostly clear

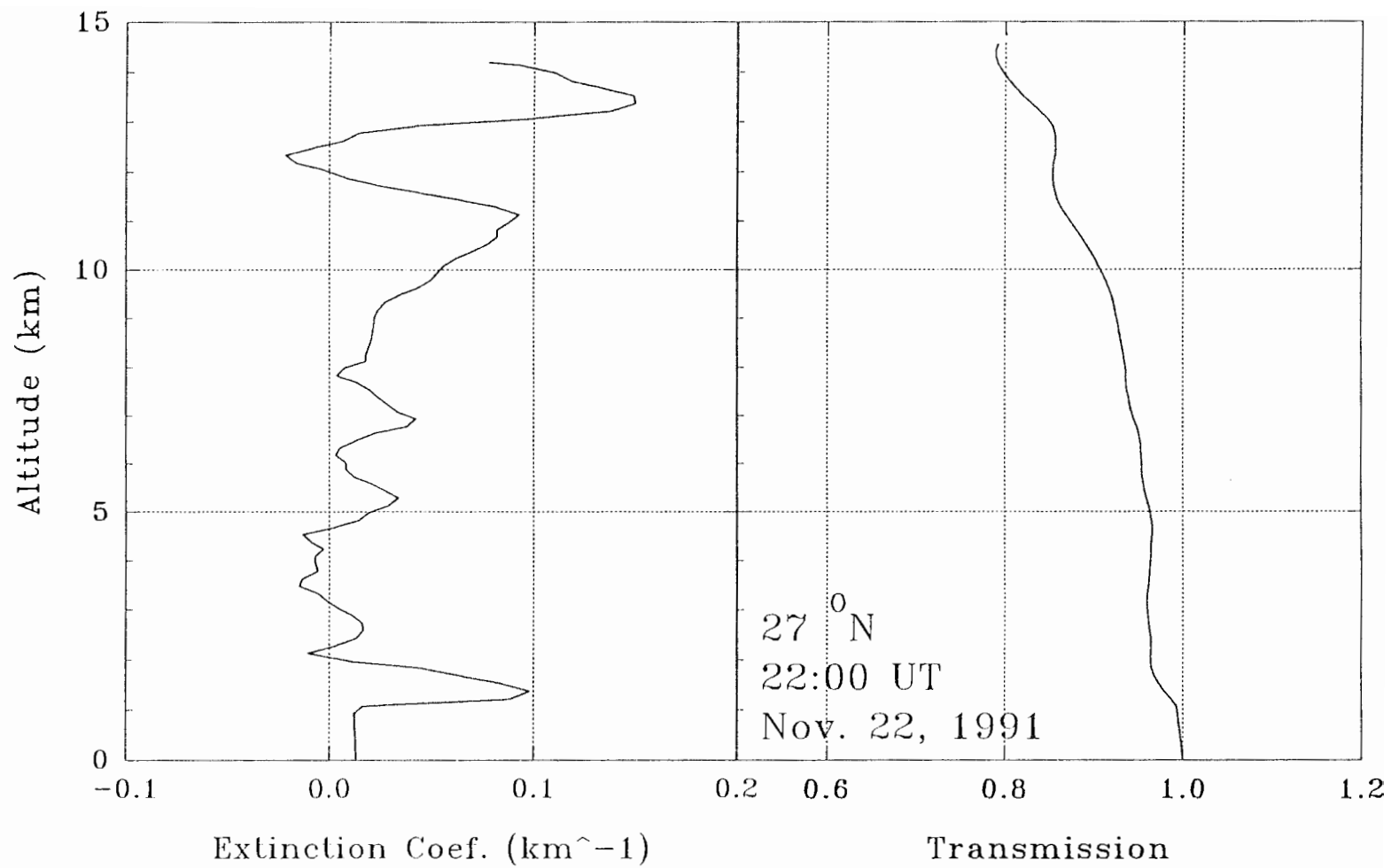


Figure 4.5. Extinction coefficient and transmission profiles have been derived from $607 \text{ nm } N_2$ Raman channel signal measured at 22:00 UT on 22 November 1991.

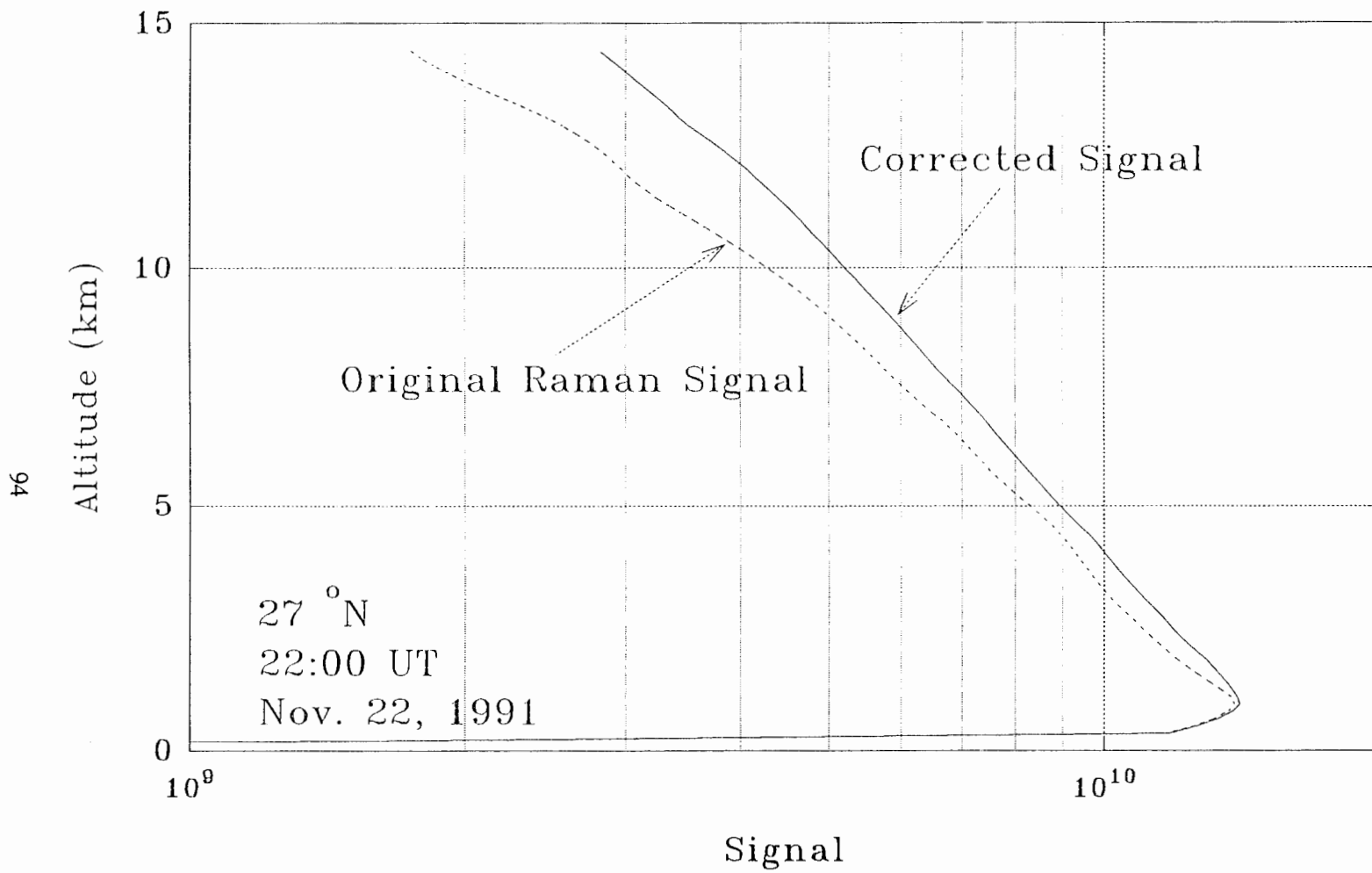


Figure 4.6. The original and transmission corrected 607 nm, N_2 Raman channel signal profiles measured at 22:00 UT on 22 November 1991.

on the night of 22 November 1991, with only a thin cloud layer distributed around 1.5 km which is observed in the extinction coefficient profile. This cloud layer was also observed on the low-altitude two-wavelength particle backscattering ratio profile, (see Figure 4.7). By using the Raman technique, we can derive the atmospheric extinction coefficient and transmission profiles.

4.2.2. LAMP Raman Lidar Optical Properties Measurements

The two-way aerosol and molecular extinction coefficients, Eq. 4.20 and 4.21, are based on the Raman channel signal and model density. This coefficient was based on the difference between the Raman channel signal and the normalized balloon density measurement, see Figure 4.8. For Raman N_2 signal to represent the atmospheric density profile, the balloon measured density profile was normalized to the peak value of the Raman N_2 signal profile. The difference between these two profiles was due to the two-way atmospheric attenuation, 532 nm upward and 607 nm downward. So, we derived the two-way atmospheric extinction and transmission profiles from this difference.

The comparison of the two different Raman N_2 profiles for the calculated atmospheric extinction and transmission are shown on the center and right of Figure 4.8 respectively. The extinction coefficient and transmission profiles derived from the 532 nm profile by using the Klett inversion [Klett, 1981, 1985] are shown for comparison. In Figure 4.8, the solid line is the calculation using the model atmosphere as reference, and the long-dashed line is the calculation based on the difference between the Raman N_2 return and the normalized balloon measurement. The extinction coefficient profiles from the Klett inversion, the short-dashed line in Fig. 4.8, could not provide accurate density and temperature measurements. The Klett inversion has difficulty in calculations under the cloudy or inhomogeneous particle distribution conditions. This inferior performance of the Klett inversion is due to inappropriate assumptions, such as the assumed

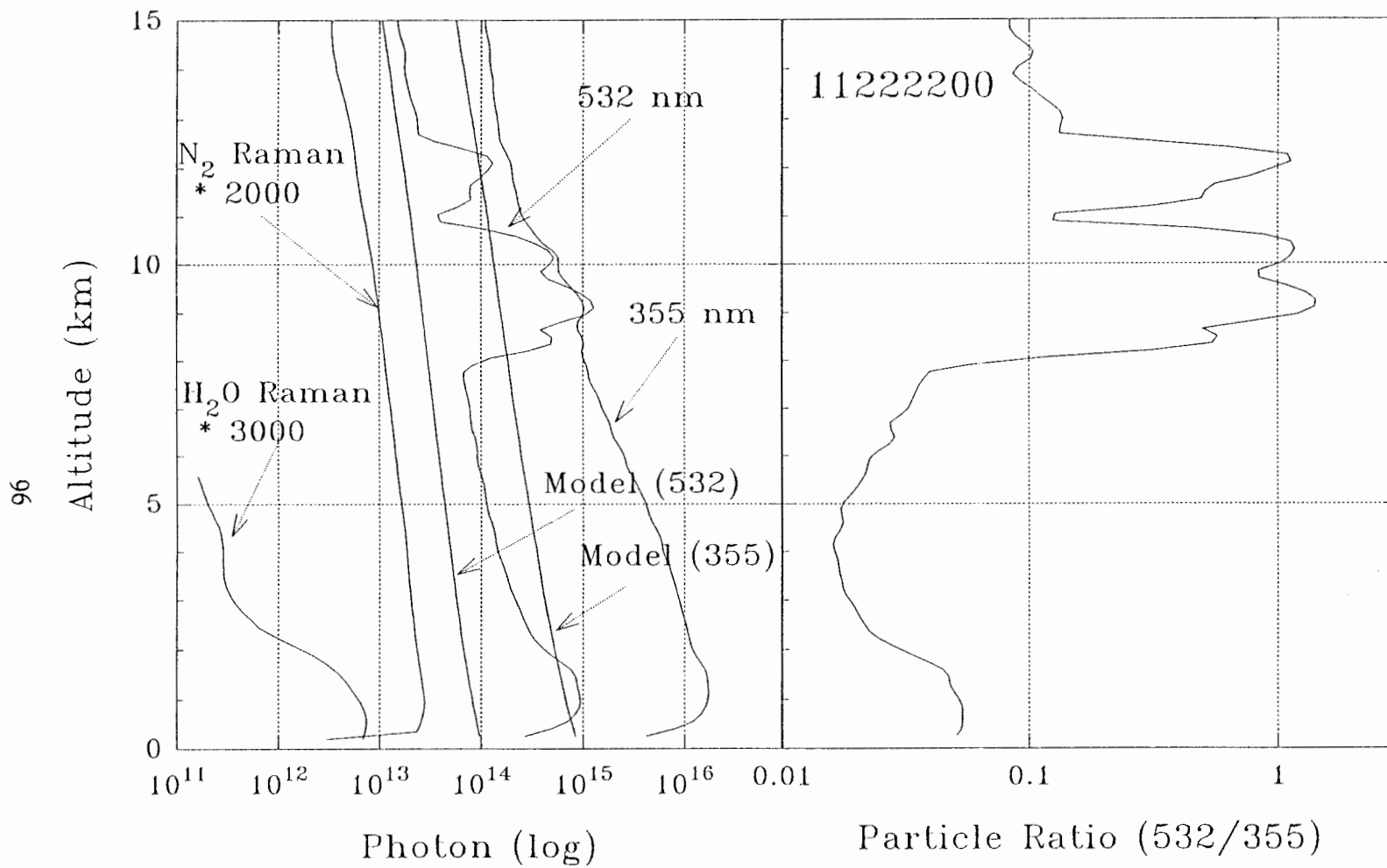


Figure 4.7. The low altitude two wavelengths, N_2 and H_2O Raman signal profiles, and R_{12} profiles measured at 22:00 UT on 22 November 1991.

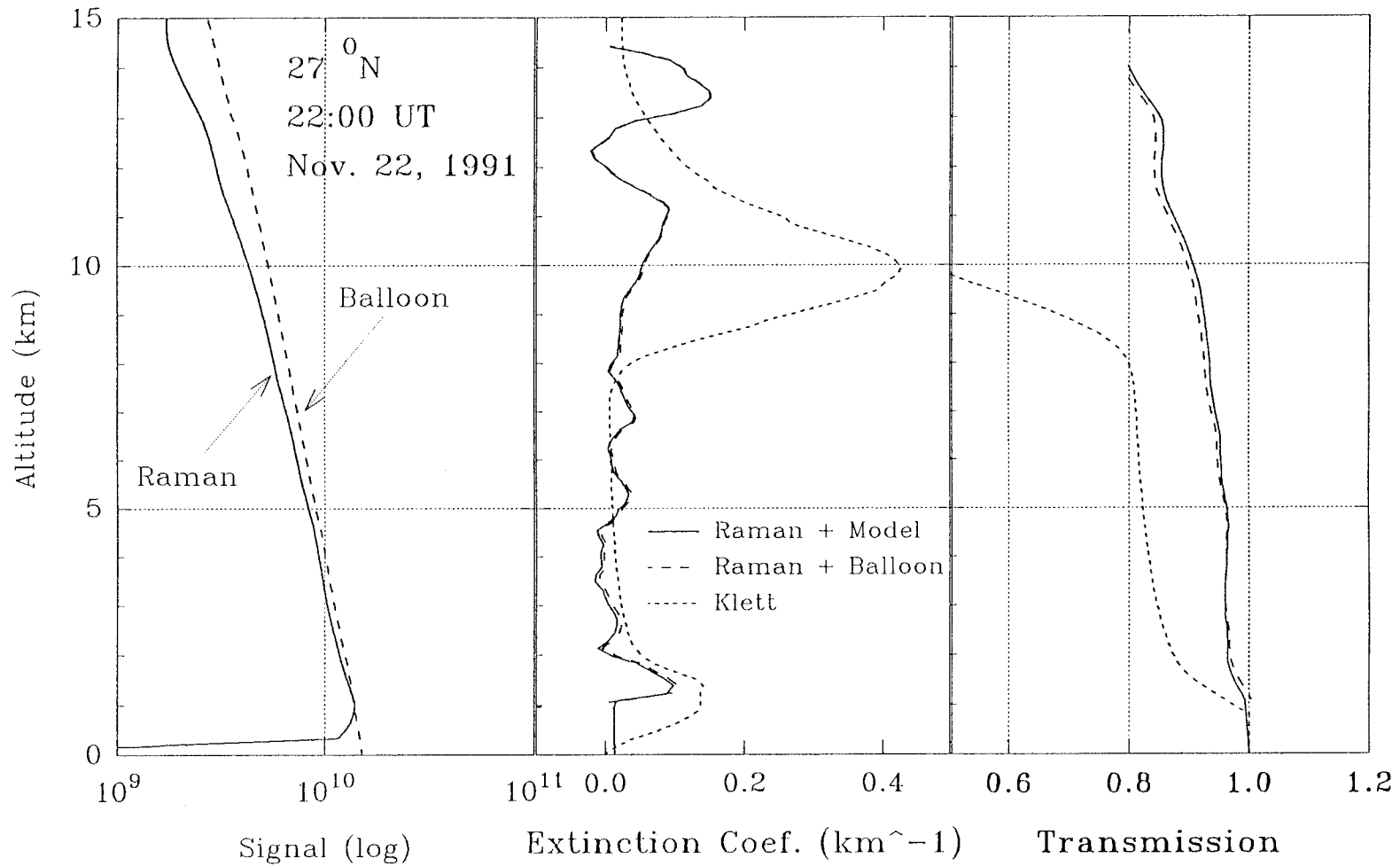


Figure 4.8. The Raman signal, normalized balloon density, extinction coefficient, and transmission profiles measured at 22:00 UT on 22 November 1991. Three extinction coefficient and transmission profiles were derived from the difference between Raman 607 nm channel signal profile and normalized balloon, or model, profile, and 532 nm channel signal profile by Klett inversion.

homogeneous particle distribution of strong scatterers. Two different Raman approaches, based on model density calculation and based on balloon density measurement, were used to calculate the extinction coefficient and transmission profiles, and they show good agreement above the boundary layer, with a transmission difference of no more than 1%.

4.3 Raman Measurements of Atmospheric Properties

The insensitivity of the atmospheric Raman backscatter signal to the presence of particles provides a useful tool for detecting molecular concentration from lidar returns. A vibrational Raman lidar can measure the molecular density profile of an atmospheric constituent except for the extinction produced by particle and molecular scattering. The Raman cross-section is about a factor of 1,000 smaller than the corresponding Rayleigh cross-section, (see Table I in Chapter 1). With such a small scattering cross-section, it is difficult to measure the molecular density at high altitude.

Observations of frequency-shifted Raman backscatter components from the vibrational-rotational band of nitrogen have been reported by Cooney [1968], and Cooney *et al.* [1969]. The Raman backscatter return component from N_2 was measured by rejecting the backscatter return of the Rayleigh line. The N_2 Raman signal profile generally represents the molecular density in the clear atmosphere but is reduced by atmospheric attenuation. This atmospheric attenuation is small unless intense particle or cloud layers are present.

We used the calculated two-way transmittance profile, $T^2(Z)$ in Eq. 4.22, to correct the atmospheric attenuation on the raw range-adjusted Raman channel signal profile, $P(Z)$. The density profile was derived by tying the signal profile to the U.S. Standard Atmosphere, 1976 model density profile at 8 km. This altitude is an atmospheric isopycnic level. At this altitude, the mean latitudinal and seasonal density variation is supposed to be less than two percent [USSA76, 1976].

From this density profile, we calculated the density ratio profile and temperature profiles as in the case of the Rayleigh signal processing.

The original range-adjusted Raman N_2 profile and transmission-corrected Raman profiles at 22:00 on 22 November, 1991 are shown in Figure 4.6. The dashed line is the original range-adjusted Raman N_2 profile, and the solid line is the transmission-corrected Raman profile. The ratio profile of measured density to model density from the U.S. Standard Atmosphere, 1976, and the temperature profile derived from the density profile are shown in Figure 4.9. The profile on the left is the density ratio profile from 1 km to 15 km. On the right side of Figure 4.9, the Raman N_2 channel temperature measurement was compared with a balloon radiosonde measurement. The balloon was released two hours earlier than the lidar measurements were made. The one standard deviation signal error bars of the Raman channel measurements are shown. This Raman lidar temperature measurement agreed well with the *in situ* balloon measurement. The transmission-corrected atmospheric profiles, density ratio and temperature, were compared with the profiles directly derived from the Raman N_2 channel signal without the attenuation correction, Figure 4.10. From this comparison we conclude that the profiles without correction, shown as dotted lines, cannot be used to represent the atmosphere. The raw Raman channel signal has to be corrected for the atmospheric attenuation to represent the true atmospheric profile. The limited accuracy to which this correction can be made has raised the question of whether this technique is a useful approach.

The first steps in the measurement of atmospheric properties, density and temperature, using Raman techniques is to determine the transmission loss and to correct the profiles for extinction. The extinction coefficient and transmission loss calculations are discussed in Section 4.2.1, these can be successfully applied in clear or thin-cloud conditions. The analysis will not work when the sky has multi-layers of clouds or thick-cloud conditions, as illustrated in Figures

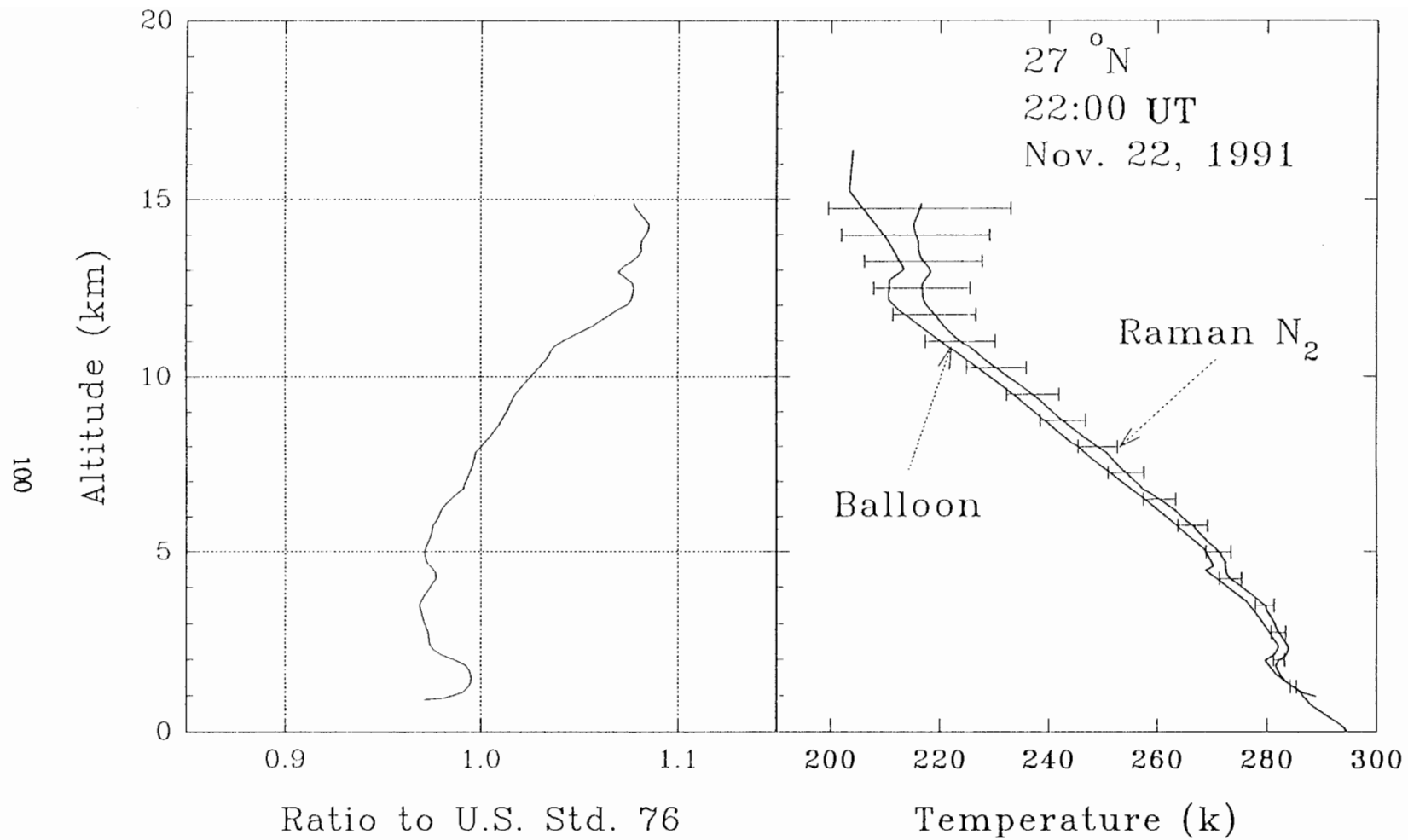


Figure 4.9. Density ratio and temperature profiles have been derived from 607 nm N₂ Raman signal profile. The derived temperature profile is compared with the balloon measurement. One standard deviation error is the lidar measurement error.

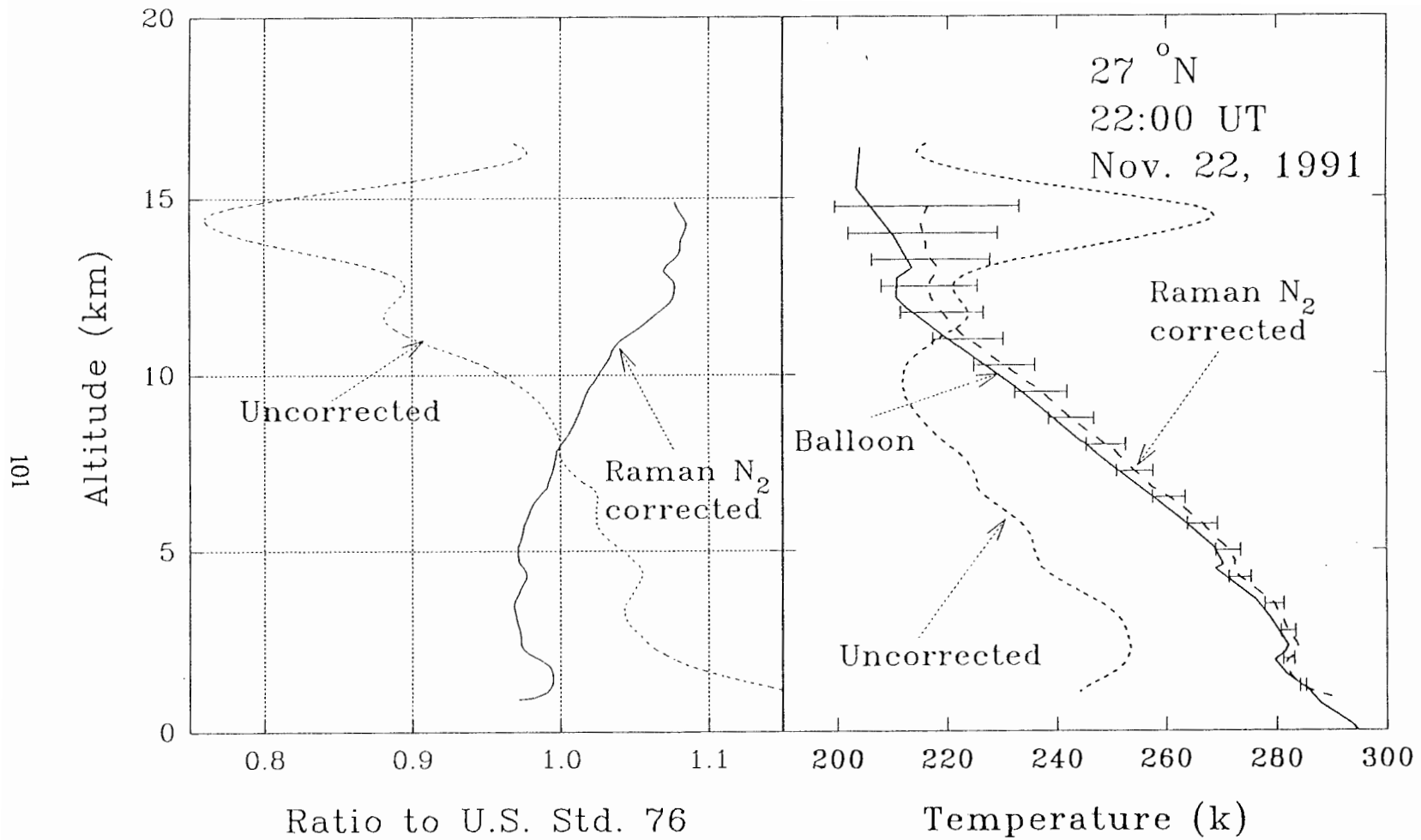


Figure 4.10. Atmospheric properties profiles at 22:00 UT on 22 November 1991, were derived from transmission corrected Raman N_2 channel signal and compared with the profiles without transmission correction.

4.11 to 4.14. Figure 4.11 shows the derived density ratio and temperature profiles at 03:25 UT on 4 December 1991, which was a cloudy night with a cloud layer of about 2.5 km thick centered at 1.5 km. The corresponding Raman signal, extinction coefficient, and transmission profiles derived from the above relations are shown in Figure 4.12 where we observed a low altitude cloud layer in the profiles. Figure 4.13 shows the derived extinction coefficient and transmission profiles on the night of 24 November 1991 where a large cloud layer from the ground to 3 km and a cirrus cloud at 8 km were observed. The corresponding density and temperature profiles are shown in Figure 4.14, note these profiles are not in agreement with the balloon measurements due to the presence of cloud layers.

4.4 Summary of Chapter

Table VI presents a summary of the maximum extinction coefficients derived from the 607 nm Raman N_2 channel, cloud observations from the two-wavelength particle backscatter return profile. In this table, we give the summary of the Raman channel temperature measurements during the Penn State LADIMAS Campaign 1991 and later measurements at the Penn State University on the night of 29 March 1992. The peak extinction coefficients below 10 km altitude are listed in the table. Cloud observations in Table VI provide information about the location and thickness of cloud layers. We conclude that the quality of the temperature profiles from vibrational Raman channel measurements is not satisfactory when significant high altitude clouds (about 9 km altitude), thick clouds (over 2.5 km), or multiple layer clouds are present. One possible reason for this poor Raman lidar performance is due to the multiple scattering inside of thick cloud layers. The question of how to handle cloudy conditions using vibrational Raman techniques is still under investigation.

The rotational Raman scattering technique provides an effective method to measure

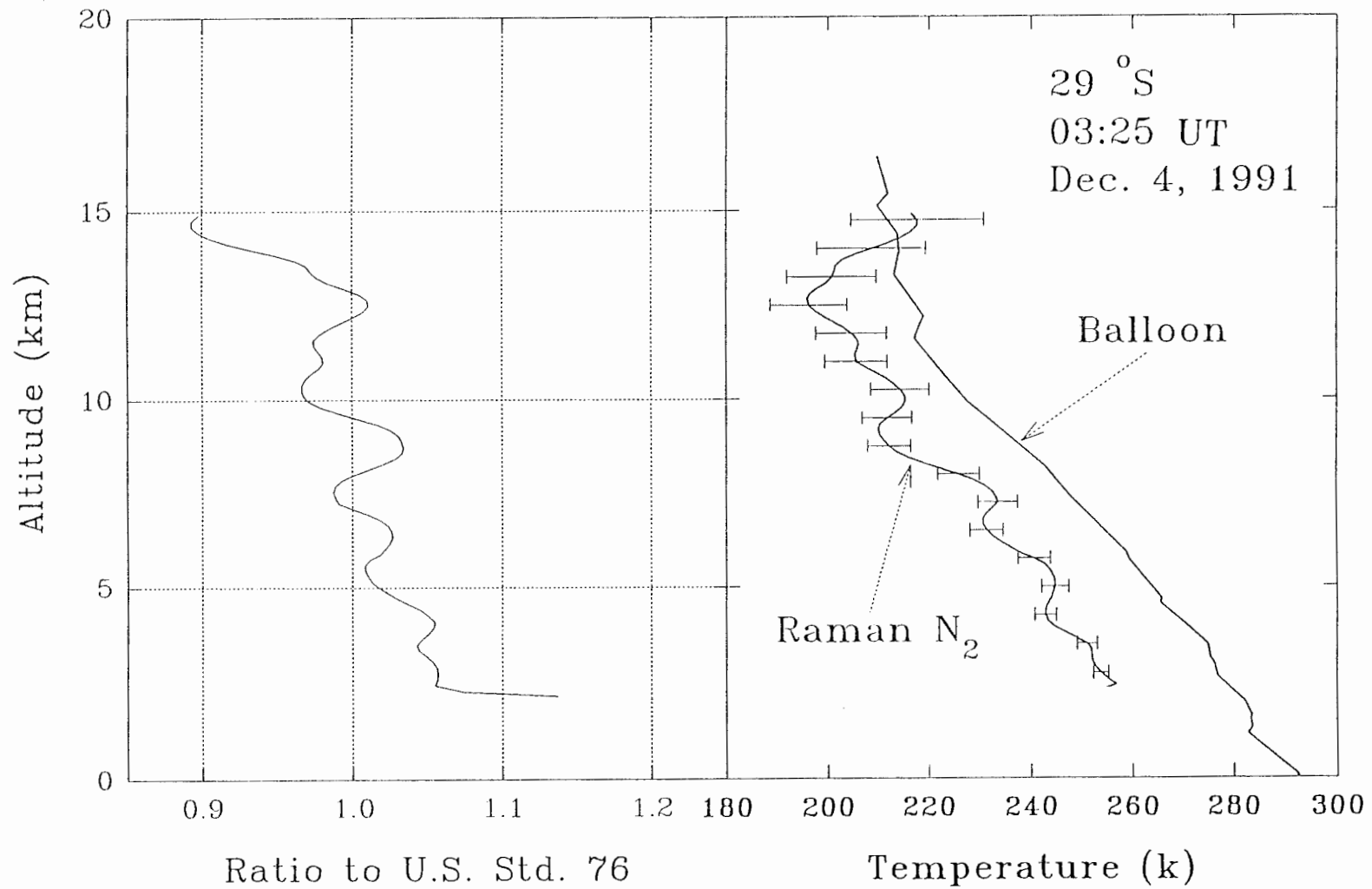


Figure 4.11. Density ratio and temperature profiles were derived from transmission corrected 607 nm N₂ Raman signal measured at 03:25 UT on 4 December 1991. A cloud layer distributed from 2 to 4 km altitude is shown which made the vibration Raman channel atmospheric profiles retrieval difficult.

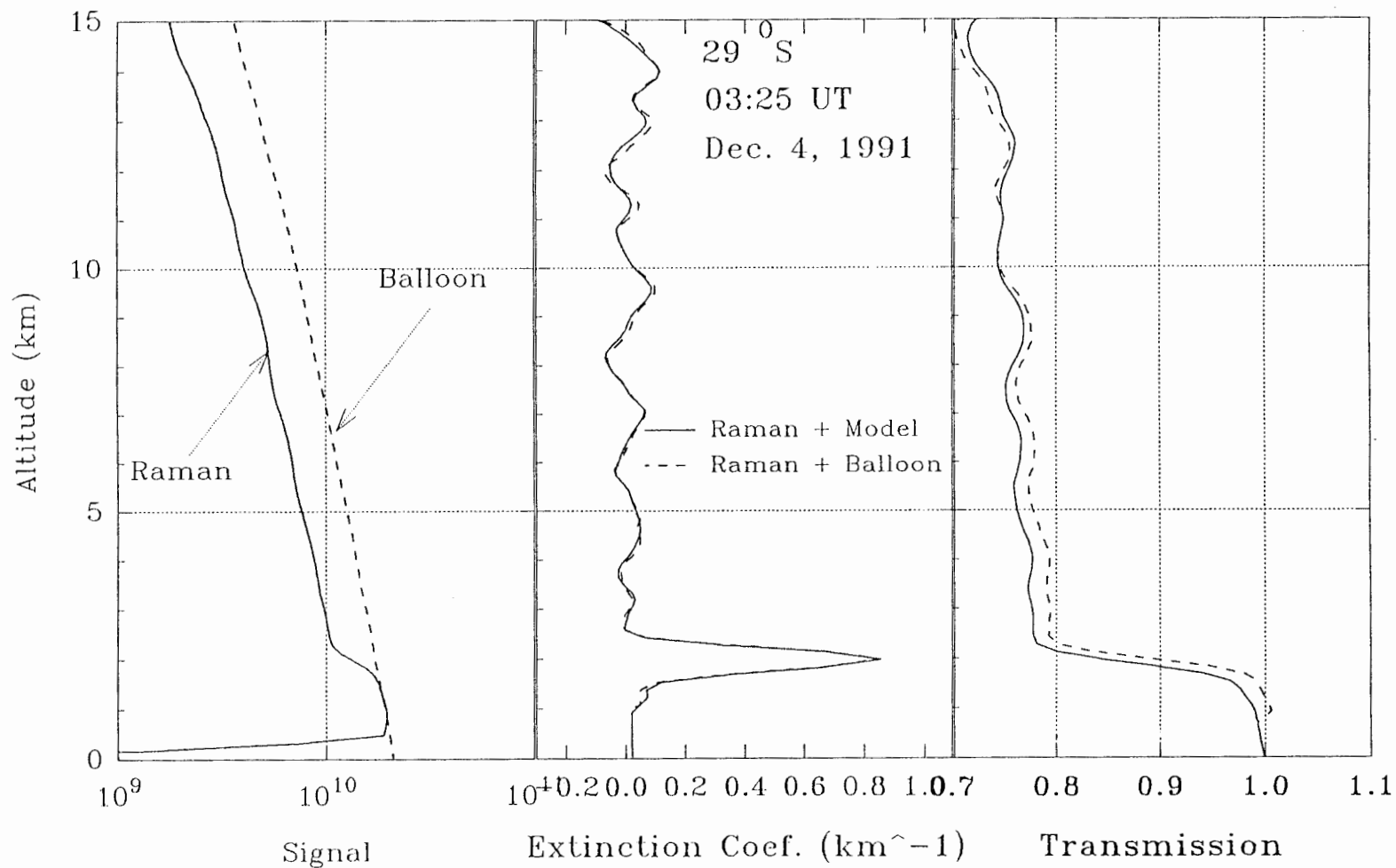


Figure 4.12. The Raman signal, normalized balloon density, derived extinction coefficient and transmission profiles measured at 03:25 UT on 4 December 1991. Two extinction coefficient and transmission profiles were derived from the difference between Raman 607 nm channel signal profile and normalized balloon, or model, profile. The existence of lower altitude cloud layer is evident.

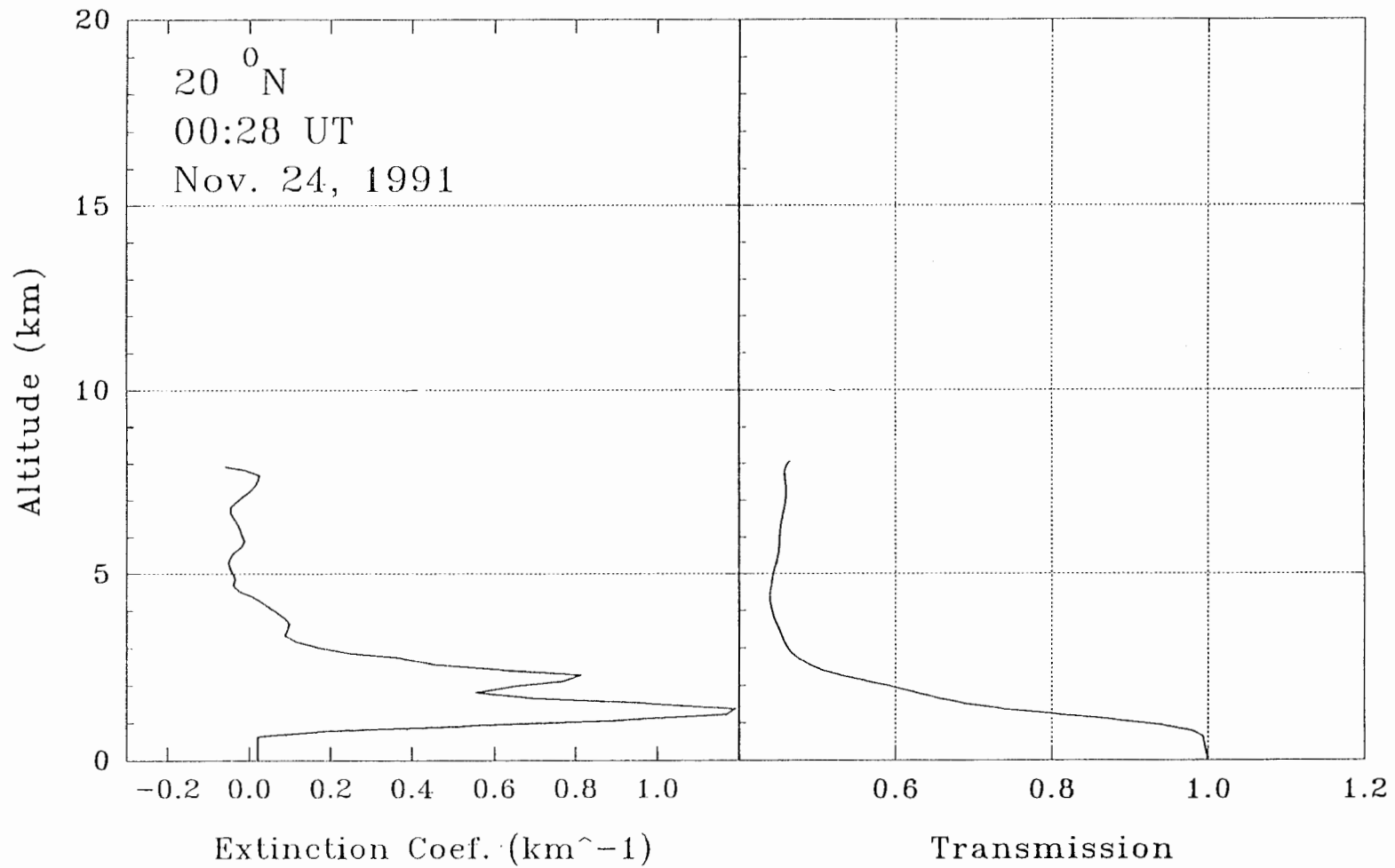


Figure 4.13. The Raman channel signal derived extinction coefficient and transmission profiles on a cloudy condition measured at 00:28 UT on 24 November 1991.

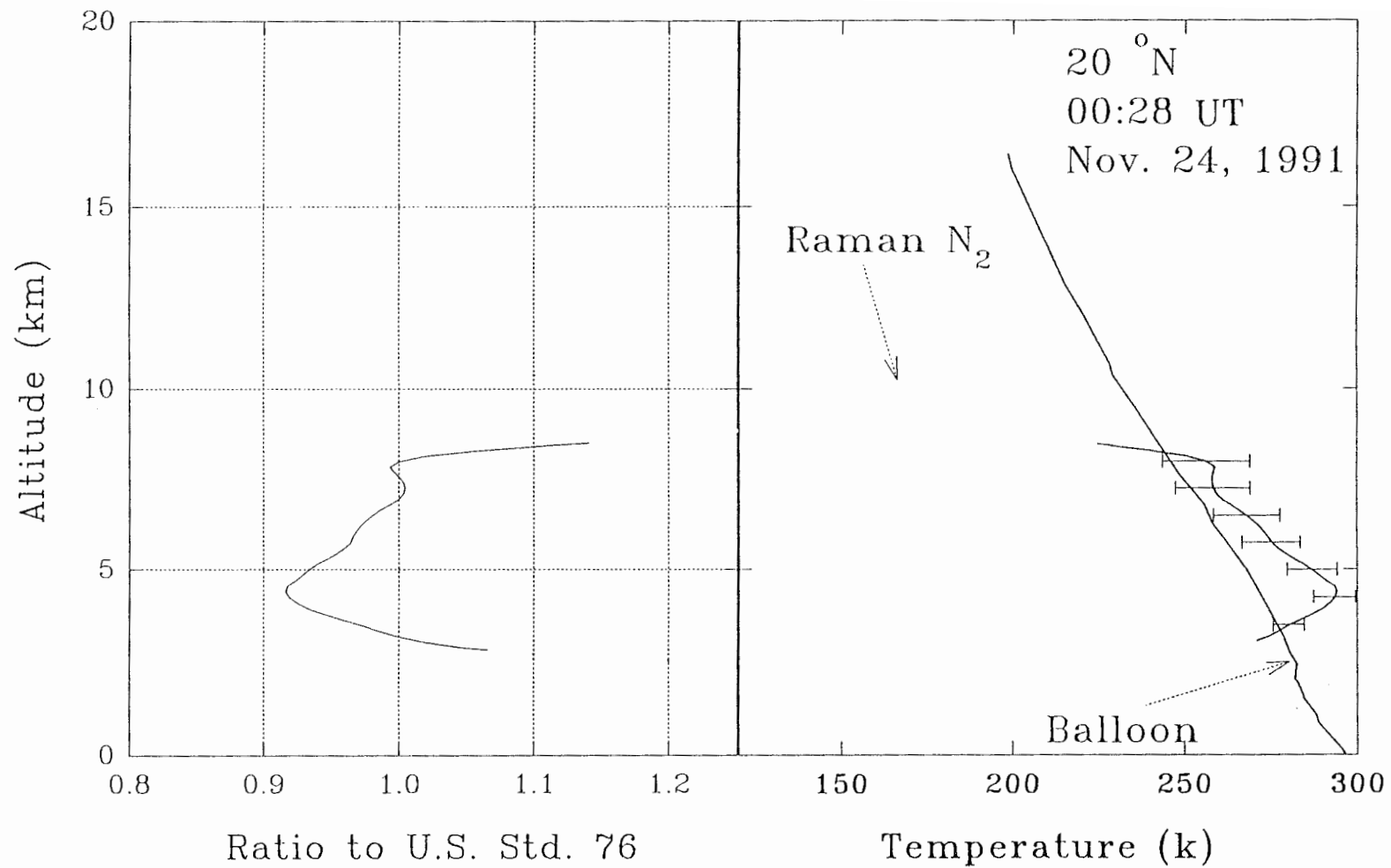


Figure 4.14. The density ratio and temperature profiles derived from transmission corrected $607\text{ nm } N_2$ Raman signal misread at 00:28 UT on 24 November 1991. The cloudy condition made vibration Raman channel atmospheric profiling unsuccessful.

TABLE VI Vibrational Raman channel extinction coefficient, clouds thickness and location, and temperature profile quality.

Date/ Time	Profile ended (km)	Max. Ext (km ⁻¹) @ (km) Below 10 km	Cloud(s)@ (km) /Thickness (km)	Temperature profile
1122/2200	17	0.1@1.2	1.5/2	Good
1122/2242	17	0.2@1.2	1.5/2	Good
1123/0121	10	0.35@1.2	1.5/1, 8/3, 11/2	Bad
1124/0028	11	0.2@1.2	1.5/3, 9.5/1.5	Bad
1126/0156	7.5	0.4@1	2/3, 7/1	Bad
1129/0102	15	0.2@1	1.5/2.5	O.K
1129/0150	15	0.15@1	1.5/2.5	O.K
1201/0137	12	1.11@1	1.5/2	O.K
1203/0320	9.5	0.15@9.5	1.5/2	O.K
1203/0419	12	0.05@4	-----	Good
1203/0452	12.5	0.05@4	-----	Good
1203/0528	12	0.05@1	9/2	Bad
1204/0207	19	0.05@1	-----	Good
1204/0241	19.5	0.04@1	-----	Good
1204/0325	15	0.85@2	1.5/3	Bad
1204/0357	15	1.2@2	1.5/3	Bad
1205/0100	15	0.4@1	1/3, 6/2, 9/1.5	Bad
1205/0151	15	0.6@1	1/3, 6/2	Bad
1205/0326	15	0.23@1	1.5/2	Good
1205/0402	18	0.7@1.5	1.5/2	Good
0329/0844	15	0.7@1.5	3/2	Good
0329/0928	17	0.65@1.5	3/1	Good
0329/1012	13	0.71@1.5	3/1	Good

temperature profiles directly and avoids the need for atmospheric transmission correction. The unique feature of the rotational Raman scattering technique is the fact that the relative intensity of the rotational states depends only on temperature. Its calibration depends on only spectroscopic characteristics and requires only one normalization, or system calibration, based on a nearby radiosonde measurement. Some early results of the Penn State Lidar group on rotational Raman are shown in Figure 4.15. On the right of Figure 4.15 are the rotational N_2 Raman signal profiles from the ground to 5 km at 530 nm and 528 nm. This thirty-minute integrated lidar measurement was made at 02:09 UT on 13 June 1993. On the left of Figure 4.15, the solid line is the derived rotational Raman scattering lidar temperature profile, and the dotted line is the balloon radiosonde measurement which was obtained 21 minutes later. These two temperature profile measurements show very good agreement. The top coordinate on the temperature profile plot is the ratio of 528/530. The rotational Raman lidar technique provides a way to accurately measure lower atmospheric temperature profiles without being bothered by the presence of the tropospheric or boundary layer particle scattering.

In summary, the Raman lidar technique has the following advantages:

- (1) The Raman technique does not require the use of a particular laser frequency, and hence, one can choose the laser frequency in a spectral region free from atmospheric absorption.
- (2) The Raman technique enables a range-resolved measurement of preselected atmospheric constituents from a single laser wavelength.
- (3) The Raman technique is not limited to any particular type of molecule and can profile almost any of the chemicals present in the air, as long as these chemicals have sufficient concentration and cross section to permit detection.
- (4) The Raman technique avoids the ambiguity in the backscatter signal at the laser

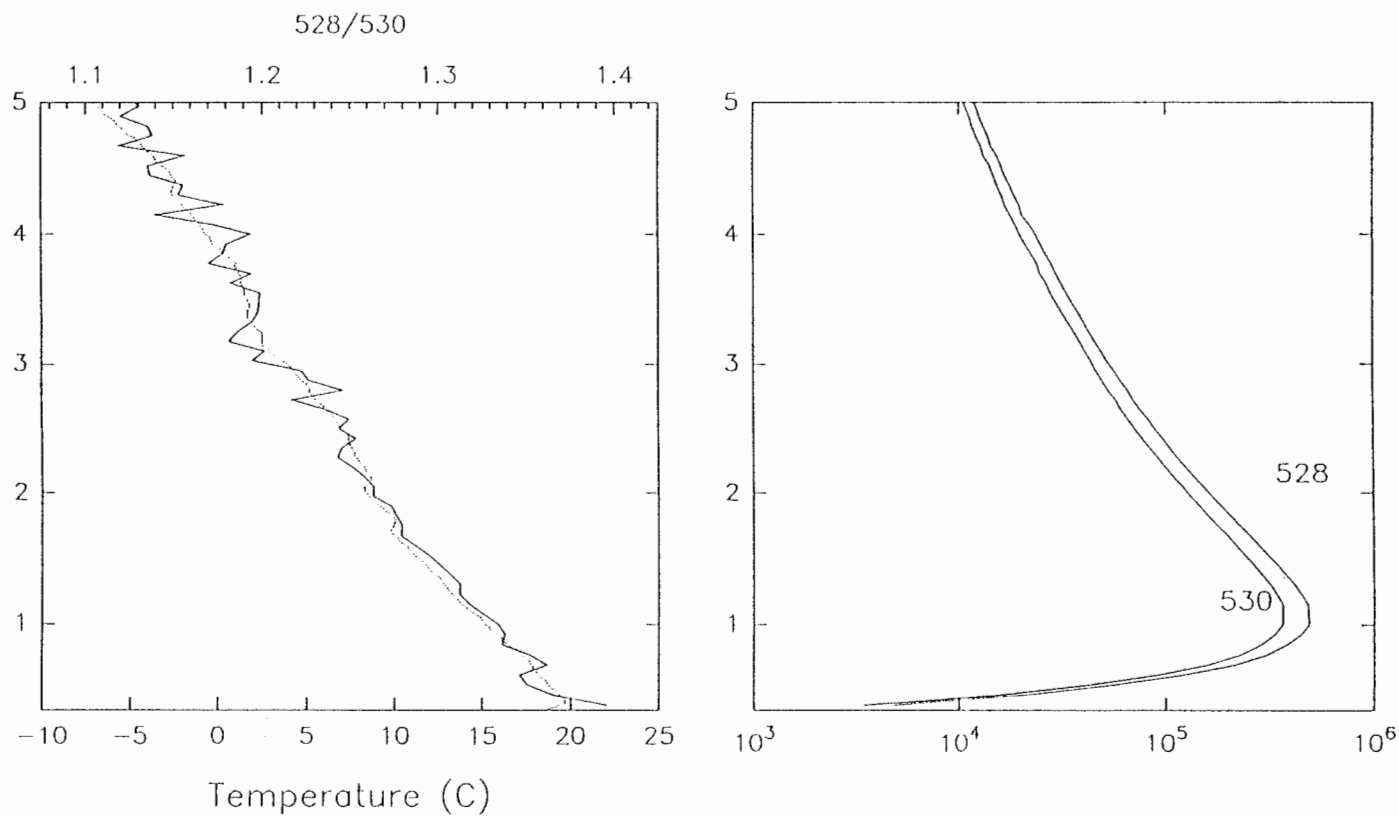


Figure 4.15. Rotational N_2 Raman temperature measurement at 02:09 UT on 13 June 1993, from ground to 5 km has been compared with balloon released at 02:30 UT, 13 June 1993. On the right, two profiles show the 30 minutes integrated photocount at 528 nm and 530 nm. On the left, the solid line is the rotational Raman lidar temperature measurement and the dotted line is the balloon measurement [McKinley, 1994].

frequency due to the particle scattering components under some atmospheric conditions, the density profile measurement can be obtained from an N_2 or O_2 molecule profile.

- (5) The Raman technique backscatter signals from major components of the atmosphere such as N_2 and O_2 , makes it possible to determine the absolute molecular density of a minor species by comparing the measured intensities to that of major component [Inaba and Kobayasi, 1972].
- (6) True optical extinction profiles can be obtained by comparison of measured Raman signal from N_2 or O_2 with a model or balloon profile of the gradient in atmospheric density.
- (7) Measurement of the N_2 Raman signal at two wavelengths (*i.e.* 607 and 387 nm) provide data on the wavelength dependence of extinction.

The main disadvantage of the Raman lidar scheme is the low detection sensitivity at long ranges due to the small Raman scattering cross-section. Thus both a high-power laser and shorter wavelengths are preferred for Raman measurements. Improvements in the signal strength can be obtained by using large telescopes, long integration times, and by making use of species with higher molecular concentrations.

Chapter 5

CONCLUSIONS AND SUGGESTED FUTURE WORK

5.1 Summary and Conclusions

This research investigates the feasibility of using lidar for atmospheric sensing from the ground to 80 km by combining Rayleigh scattering, two-wavelength probing, and Raman scattering lidar techniques. The atmospheric properties in which we are interested include atmospheric density, density ratio, temperature, and atmospheric extinction. Data were collected from January 1989 to July 1993 including two major campaigns, AIDA and LADIMAS, and with additional measurements at Penn State University. The AIDA campaign covered the early spring from January 15 to April 5, 1989 in Arecibo, Puerto Rico, $18^{\circ}N$. The three-month LADIMAS campaign included shipboard measurements across the latitudinal region from $70^{\circ}N$ to $65^{\circ}S$. Lidar measurements have been made at Penn State, $42^{\circ}N$, on an irregular basis during 1991, 1992 and 1993.

The molecular backscatter signals were used to determine the relative density as a ratio to U.S. Standard Atmosphere, 1976, and temperature profiles in the mesosphere and stratosphere. Part of the molecular backscatter data used in this research work was from the NSF CEDAR (Coupling, Energetic, Dynamic, Atmospheric Region) sodium resonance lidar, which was operated at Arecibo during the AIDA 1989 campaign. The signal processing techniques used, including pre-processing, background noise determination and subtraction, profile filtering and smoothing, have been discussed. By assuming a particle-free region above 30 km , I calculated atmospheric density, density ratio to model, and temperature profiles from lidar measurements.

Another useful lidar atmospheric profile is the backscatter ratio profile. This ratio is defined as total, molecular and particle, backscatter signal divided by the molecular portion of backscatter signal. This backscatter ratio, which is also related to atmospheric turbidity, provides

the information about volcanic aerosol layers, cirrus cloud layers, and boundary aerosol layer distributions.

The two-wavelength lidar approach was proposed to measure the relative density and temperature profiles in the stratospheric volcanic particle layer from 20 to 40 km. By assuming fixed wavelength dependence, q , of particle scattering cross-section over the entire volcanic aerosol layer, a closed-form two-wavelength lidar inversion algorithm (Eq. 3.40-3.43) was developed to separate the stratospheric particle and molecular contributions of the returned signal. The two-wavelength lidar approach was able to retrieve the backscattered molecular signal in the stratospheric volcanic aerosol layer from the top of the layer, near 35 km, downward to about 27 km. Starting from 27 km downward, an additional group of particles was present in the stratospheric volcanic aerosol layer. This was revealed by the two-wavelength particle backscatter ratio (R_{12}) profiles. A constant two-wavelength particle backscatter ratio profile implies that there was only one type of particles dominant in that altitude region. On the other hand, a changing ratio profile implies the presence of several groups of particles. The presence of other groups of particles makes two-wavelength inversion of density and temperature profiles impossible.

The two-wavelength lidar approach was found valid for measuring atmospheric profiles only when the two-wavelength particle backscatter ratio is a constant single value within the volcanic aerosol layer. From the observations of two-wavelength particle backscatter ratio profiles, I found that there were usually two or more groups of particles present in the stratospheric volcanic aerosol layer. By using more wavelengths in a lidar instrument, it might be possible to derive additional information such as wavelength dependence of scattering particles when multiple types of particles are present. The wavelength dependence of different particles will lead to the determination of stratospheric density and temperature.

To derive the tropospheric density from a vibrational N_2 Raman lidar return, a

transmission correction of the Raman channel signal is necessary. The atmospheric transmission at the laser wavelength has been determined uniquely from the known atmospheric density profile and Raman N_2 return signal profile. In this research, two calculations have been attempted to find the tropospheric extinction coefficient and transmission profiles from the vibrational N_2 Raman channel signal. Then the tropospheric density and temperature profiles were calculated from the transmission-corrected N_2 Raman channel signal. The quality of the tropospheric density and temperature profiles obtained above the boundary layer depends on good visibility in the troposphere. For multilayer clouds or thick clouds, the N_2 vibrational Raman signal approach will not provide acceptable profiles for atmospheric properties. A contributing reason for the poor atmospheric profiling from the vibrational Raman N_2 channel is probably multiple scattering inside the cloud layer which leads to large extinction. The difficulty in using the N_2 Raman signal is the requirement to integrate the profile downward for several kilometers before convergence is achieved. The presence of layers of scattering lead to small uncorrected extinction gradient in the density profile in most cases.

A combination of density ratio and temperature profiles based upon the several analysis techniques for measurements at 01:51 UT on 5 December 1991 are shown in Figure 5.1. Temperature profiles were compared with the U.S. Standard Atmosphere, 1976. Three different lidar analysis techniques were applied to different altitude regions and the results are shown beyond their region of applicability for emphasis. Below 15 km , vibrational Raman N_2 provided good density and temperature measurements. The two-wavelength lidar analysis provided density and temperature measurements in the altitude region between 30 and 40 km . The volcanic aerosol particle effects on the measurements limited the single wavelength lidar analysis to altitude above 35 km . From 20 to 40 km , the two-wavelength technique yields a reasonable density measurement, with density measurement within 20% of standard atmosphere, even with the presence of

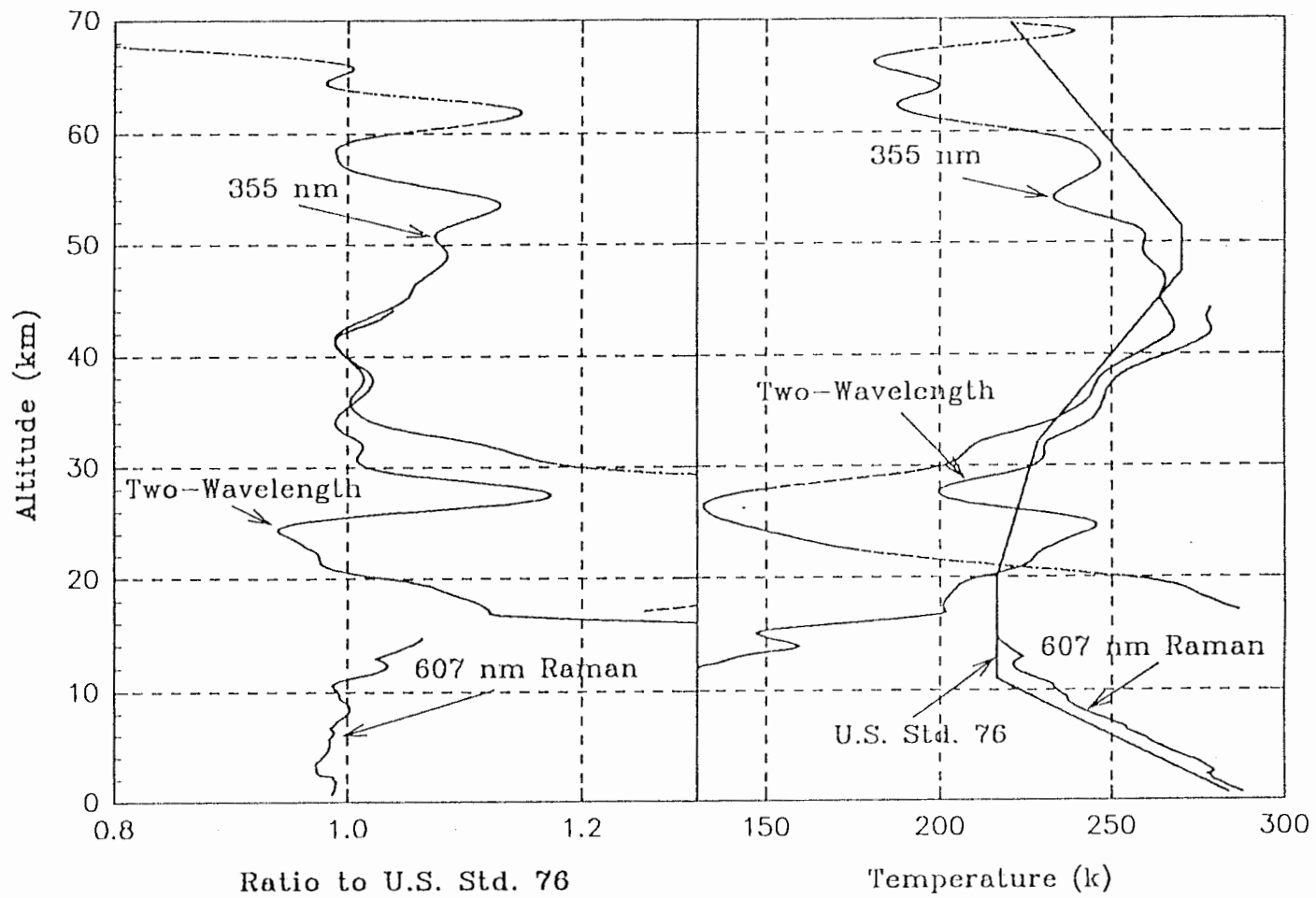


Figure 5.1. The summarized density ratio and temperature profiles by different lidar techniques on 5 December 1991. Derived temperature profile is compared with the U.S. Standard Atmosphere, 1976.

volcanic aerosols. Middle atmosphere gravity waves above *40 km* were observed on the density ratio and temperature profiles from the *355 nm* Rayleigh lidar measurement. With a more powerful laser and larger telescope, the Raman technique can extend well above *20 km*. Thus by combining these three lidar techniques, it is possible to measure the atmospheric properties from the ground to the mesosphere under relatively clear sky conditions.

The molecular rotational Raman lines near *528 nm* and *530 nm* excited by *532 nm* laser radiation have been used for lower tropospheric temperature profiling. Temperature was measured by taking the intensity ratio between these two wavelength regions. Compared with vibrational Raman scattering, the rotational Raman measurement does not require an absolute calibration and only depends on signal ratio at the particular range bin. The rotational Raman lidar has been demonstrated as a valid technique in the troposphere, even when aerosols are present. This method is totally independent of model assumptions, and sampling geometry used, and requires only a single radiosonde comparison to develop the inversion algorithm.

The two-wavelength particle backscatter ratio profile provides a unique tool to study the distribution of the stratospheric volcanic aerosol layer. This two-wavelength particle backscatter ratio is constant when there is only one particle type. We assume that this group of particles has the same size distribution, same shape, and same refractive index when the ratio remains constant. Observations of stratospheric volcanic aerosol layers and cirrus cloud layers show that different particle groups have different two-wavelength particle backscatter ratios. Based on the study from the LADIMAS Campaign and the lidar measurements at Penn State, the settling of the Pinatubo volcanic aerosol particles has been observed. Three months were required for particles to settle from a layer centered near *32 km* to *22 km*. Further investigations should help an understanding of the behavior of this volcanic aerosol layer.

Atmosphere structure measurements have been demonstrated by combining several lidar

techniques, including Rayleigh, two-wavelength, vibrational N_2 Raman, and rotational N_2 Raman techniques. The Rayleigh lidar is valid for measurements above 35 km , under the assumption of a particle-free atmosphere. Two-wavelength lidar can derive stratospheric properties where there is only one dominant group of particles, such as from 27 km to 35 km during the LADIMAS campaign. With a powerful laser and a sensitive detection system, vibrational Raman lidar is capable of measuring density and temperature above the tropopause. The rotational Raman lidar provides the accurate temperature profile measurements from ground to 15 km , or higher, even in the presence of tropospheric aerosol and clouds.

This research effort assessed the applicability of the two-wavelength lidar technique in the range 20 to 40 km . I have shown the uniqueness and the importance of using two wavelengths to identify regions containing particles, as well as, to show when the dominant particle type changes. The limitations of two-wavelength lidar technique in the measurements of atmospheric properties, density and temperature, was discussed. I have demonstrated the power of the Raman technique, N_2 vibrational and rotational components, for accurate measurements of the atmospheric structure properties and definition of the optical environment. The application of N_2 vibrational Raman technique in atmospheric properties is limited to the above boundary layer and clear sky conditions.

Active lidar remote sensing offers several distinctive capabilities which were not possible with passive systems. The most apparent capability is the high vertical or horizontal resolution due to the short pulse lengths and precise round trip timing of the backscattered radiation. The increased spatial and temporal resolution and accuracy of active lidar systems are extending our understanding of the processes that occur in the atmosphere.

5.2 Recommendations for Future Work

To further enhance and extend the research results presented in this thesis, several future topics are recommended:

1. Improvement and further verification of the technique of using the rotational Raman lidar technique to measure the lower tropospheric temperature.
2. Investigations of the use of multiple wavelengths, more than two, for lidar measurements of stratospheric aerosol layer properties.
3. Investigations of mesospheric and stratospheric dynamics and gravity wave propagation studies based upon lidar measurements.
4. Long period observations of the stratospheric aerosol layers to study the evolution processes.

BIBLIOGRAPHY

- Abreu, V.J., Lidar from Orbit, *Optical Engineering*, 19, 489-493, 1980.
- Ansmann, A., M. Riebesell, U. Wandinger, C. Weitkamp, E. Voss, W. Lahmann, and W. Michaelis, Combined Raman Elastic-Backscatter LIDAR for Vertical Profiling of Moisture, Aerosol Extinction, Backscatter, and LIDAR Ratio, *Applied Physics B*, 55, 18-28, 1992.
- Ansmann, A., M. Riebesell, and C. Weitkamp, Measurement of Atmospheric Aerosol Extinction Profiles with a Raman Lidar, *Optics Letters*, 15, 1990.
- Arshinov, Yu.F., S.M. Bobrovnikov, V.E. Zuev, V.M. Mitev, Atmospheric temperature Measurements Using a Pure Rotational Raman Lidar, *Applied Optics*, 22, 2984-2990, 1983.
- Barrett, E.W. and O. Ben-Dov, Application of Lidar to Air Pollution Measurements, *Journal of Applied Meteorology*, 6, 500-515, 1967.
- Beatty, T.J. and C.S. Gardner, Lidar Observations of Gravity Waves and Their Spectra Near the Mesopause and Stratopause at Arecibo, *Atmos. Sci.*, 1990.
- Bilbe, R.M., S.J. Bullman, and F. Swaffield, An Improved Raman LIDAR System for the Remote Measurement of Natural Gas Release into the Atmosphere, *Measurement Science Technology*, 1, 495-499, 1990.
- Bilbro, J.W., Atmospheric Laser Doppler Velocimetry: An Overview, *Optical Engineering*, 19, 533-542, 1980.
- Blamont, J.E., M.L. Chanin, G. Magie, Vertical Distribution and Temperature Profile the Night Time Atmospheric Sodium Layer Obtained by Laser Backscatter, *Annales De Geophysique*, 28, 833-838, 1972.
- Browell, E.V., Ozone and Aerosol Measurements with an Airborne Lidar System, *Optics & Photonics News*, 2, 8-11, 1991.
- Camagni, P., and S. Sandroin, *Optical Remote Sensing of Air Pollution*, Elsevier, Amsterdam, 1984.
- Carswell, A.I., Lidar Remote Sensing of Atmospheric Aerosols, *Propagation Engineering: Third in a Series, SPIE*, 1312, 206-220, 1990.
- Chanin, M.L., and A. Hauchecorne, Lidar Observation of Gravity and Tidal Waves in the Stratosphere and Mesosphere, *J. Geophysical Research*, 86, 9715-9721, 1981.
- Chanin, M.L., A. Garnier, A. Hauchecorne, and J. Porteneuve, A Doppler Lidar for Measuring Winds in the Middle Atmosphere, *Geophysical Research Letters*, 16, 11, 1273-1276, 1989.

- Collis, R.T.H., Lidar, *Advances in Geophysics*, edited by H.E. Landsberg, and J. van Mieghem, 113-138, Academic Press, New York, 1969.
- Cooney, J.A., Measurements of the Raman Component of Laser Atmospheric Backscatter, *Applied Physics Letters*, 12, 40-42, 1968.
- Cooney, J., Remote Measurements of Atmospheric Water Vapor Profiles Using the Raman Component of Laser Backscatter, *Journal of Applied Meteorology*, 9, 182-184, 1970.
- Cooney, J., Measurement of Atmospheric Temperature Profiles by Raman Backscatter, *Journal of Applied Meteorology*, 11, 108-112, 1972.
- Cooney, J.A., A Method for Extending the Use of Raman Lidar to Daytime, *Journal of Applied Meteorology*, 12, 888-890, 1973.
- Cooney, J.A., Lidar Method of Measurement of Atmospheric Extinction and Ozone Profiles, *Applied Optics*, 25, 2035-2036, 1986.
- Cooney, J.A., Acquisition of Atmospheric Extinction Profiles by Lidar: Further Notes, *Applied Optics*, 26, 3487-3489, 1987.
- Cooney, J., Remote Measurements of Atmospheric Water Vapor Profiles Using the Raman Component of Laser Backscatter, *J. of Applied Meteorology*, 29, 9, 1990.
- Cooney, J., J. Orr, and C. Tomasetti, Measurements Separating the Gaseous and Aerosol Components of Laser Atmospheric Backscatter, *Nature*, 224, 1969.
- Cooney, J., K. Petri, and A. Salik, Measurements of High Resolution Atmospheric Water-Vapor Profiles by Use of a Solar Blind Raman Lidar, *Applied Optics*, 24, 104-108, 1985.
- Derr, V.E. and C.G. Little, A Comparison of Remote Sensing of the Clear Atmosphere by Optical, Radio, and Acoustic Radar Techniques, *Applied Optics*, 9, 1976-1992, 1970.
- Eloranta, E., Lidar Observations of the Atmospheric Boundary Layer, *Sixth Symposium on Meteorological Observations and Instrumentation*, New Orleans, La., published by the American Meteorological Society, Boston, Mass., 1987.
- Elterman, L.B., The measurement of stratospheric density distribution with the search light technique, *J. Geophys. Res.*, 56, 509-520, 1951.
- Evans, W.M.E., Evaluation of a Near-Infrared Photomultiplier for Airborne Lidar Applications, *NASA CR-145380*, 1978.
- Ferrare, R.A., S.H. Melfi, D.N. Whiteman, and K.D. Evans, Raman Lidar Measurements of Pinatubo Aerosols over Southeastern Kansas During November-December 1991, *Geophysical Research Letters*, 19, 1599-1602, 1992.

- Fiocco, G., L.D. Smullin, Detection of Scattering Layers in the Upper Atmosphere (60-140 km) by Optical Radar, *Nature*, 199, 1275, 1963.
- Fiocco, G., and J. B. DeWolf, Frequency Spectrum of Laser Echoes from Atmospheric Constituents and Determination of Aerosol Content of Air, *J. Atmos. Sci.*, 25, 488, 1968.
- Fiocco, G., G. Benedetti-Michelangeli, K. Maischberger, and E. Madonna, Measurement of Temperature and Aerosol to Molecule Ratio in the Troposphere by Optical Radar, *Nature Physical Science*, London, 229, 78, 1971.
- Gibson, A.J., and M.C.W. Sandford, The Seasonal Variation of the Night-Time Sodium Layer, *Journal of Atmospheric and Terrestrial Physics*, 33, 1675-1684, 1971.
- Gille, S.T., A. Hauchecorne, and M.L. Chanin, Semidiurnal and Diurnal Tidal Effects in the Middle Atmosphere as Seen by Rayleigh Lidar, *Journal of Geophysical Research*, 96, 7579-7587, 1991.
- Gobbi, G.P., F. Congeduti, and A. Adriani, Early Stratospheric Effects of the Pinatubo Eruption, *Geophysical Research Letters*, 19, 997-1000, 1992.
- Grant, W.B., Differential Absorption and Raman Lidar for Water Vapor Profile Measurements: A Review, *Optical Engineering*, 30, 40-48, 1991.
- Grund, C.J., E.W. Eloranta, University of Wisconsin High Spectral Resolution Lidar, *Optical Engineering*, 30, 6-12, 1991.
- Hamilton, P.M., The Application of a Pulsed-Light Rangefinder (Lidar) to the Study of Chimney Plumes, *Phil. Trans. Roy. Soc. Lond.*, A. 265, 153-172, 1969.
- Hardesty, R.M., M.J. Post, and R.M. Banta, Observing Atmospheric Winds with a Doppler Lidar, *Optics & Photonics News*, 2, 1991.
- Hauchecorne, A., M.L. Chanin, and P. Keckhut, Climatology and Trends of the Middle Atmospheric Temperature (33-87 km) as Seen by Rayleigh Lidar over the South of France, *Journal of Geophysical Research*, 96, 15297-15309, 1991.
- Hauchecorne, A., M.L. Chanin, P. Keckhut, D. Nedeljkovic, LIDAR Monitoring of the Temperature in the Middle and Lower Atmosphere, *Applied Physics*, B55, 29-34, 1992.
- Heaps, W.S., T.J. McGee, R.D. Hudson, and L.O. Caudill, Stratospheric Ozone and Hydroxyl Radical Measurements by Balloon-Borne Lidar, *Applied Optics*, vol. 21, pp. 2265-2274, 1982.
- Hinkley, E.D., *Laser Monitoring of the Atmosphere*, Springer-Verlag, New York, 1976.
- Houston, J.D., S. Sizgoric, A. Ulitsky, and J. Banic, Raman Lidar System for Methane Gas Concentration Measurements, *Applied Optics*, 25, 2115-2121, 1986.

- Hunt, W.H., S.K. Poultnery, Testing the Linearity of Response of Gated Photomultipliers in Wide Dynamic Range Laser Radar Systems, *IEEE Transactions on Nuclear Science*, NS-22, 116-120, 1975.
- Inaba, H., T. Kobayasi, Laser-Raman Radar --- Laser-Raman Scattering Methods for Remote Detection and Analysis of Atmospheric Pollution ---, *Opto-electronics*, 4, 101-123, 1972.
- Inaba, H., Detection of Atoms and Molecules by Raman Scattering and Resonance Fluorescence, in *Laser Monitoring of the Atmosphere*, Edited by E.D. Hinkley, Springer-Verlag, Berlin, 1976.
- Iwasaka, Y., and K. Isono, Lidar Observation of the Stratospheric Aerosols at Two Different Wavelength, 0.6943 μm and 1.06 μm , *Journal of Atmospheric and Terrestrial Physics*, 39, 117-120, 1977.
- Junge, C.E., C.W. Chagnon, and J.E. Manson, Stratospheric Aerosols, *Journal of Meteorology*, 18, 81-108, 1961.
- Junge, C.E., and J.E. Manson, Stratospheric Aerosol Studies, *Journal of Geophysical Research*, 66, 2163-2182, 1961.
- Junge, C.E., *Air Chemistry and Radioactivity*, Academic Press, New York, 1963.
- Keckhut, P., and M.L. Chanin, Middle Atmosphere Response to the 27-Day Solar Rotation as Observed by Lidar, *Geophysical Research Letters*, 19, 809-812, 1992.
- Kent, G.S., M.C.W. Sandford, and W. Keenlside, Laser Radar Observations of Dust from Comet Bennett, *Journal of Atmospheric and Terrestrial Physics*, 33, 1257-1262, 1971.
- Kerker, M., *The Scattering of Light*, Academic Press, New York, 1969.
- Killinger, D.K., and N. Menyuk, Laser Remote Sensing of the Atmosphere, *Science*, 235, 37-45, 1987.
- Klett, J.D., Stable Analytical Inversion Solution for Processing Lidar Returns, *Applied Optics*, 20, 211-220, 1981.
- Klett, J.D., Lidar Inversion with Variable Backscatter/Extinction Ratios, *Applied Optics*, 24, 1638-1643, 1985.
- Kneizys, F.X., E.P. Shettle, L.W. Abreu, J.H. Chetwynd, G.P. Anderson, W.O. Gallery, J.E.A. Selby, S.A. Clough, *User Guide to LOWTRAN 7*, AFGL-TR-88-0177, Air Force Geophysics Laboratory, Hanscom AFB, MA, 1988.
- Kobayasi, T., and H. Inaba, Laser Raman Radar for Chemical Analysis of Polluted Air, *Nature*, 224, 170-172, 1969.

- Kolev, I., O. Parvanov, and B. Kaprielov, Lidar Determination of Winds by Aerosol Inhomogeneities: Motion Velocity in the Planetary Boundary Layer, *Applied Optics*, 27, 2524-2531, 1988.
- Korb, C.L. and C.Y. Weng, A Theoretical Study of a Two-Wavelength Lidar Technique for the Measurement of Atmospheric Temperature Profiles, *Journal of Applied Meteorology*, 21, 1346-1355, 1982.
- Kwon, K.H., D.C. Senft, and C.S. Gardner, Lidar Observations of Sporadic Sodium Layers at Mauna Kea Observatory, Hawaii, *Journal of Geophysical Research*, 93, 14199-14208, 1988.
- Lefrere, J., J. Pelon, C. Cahen, A. Hauchecorne, and P. Flamant, Lidar Survey of the Post Mt. St. Helens Stratospheric Aerosol at Haute Provence Observatory, *Applied Optics*, 20, 1116-1117, 1981.
- Leonard, D.A., Observation of Raman Scattering from the Atmosphere Using a Pulsed Nitrogen Ultraviolet Laser, *Nature*, 216, 142-143, 1967.
- Leonard, D.A., and B. Caputo, A Single-ended Atmospheric Transmissometer, *Optical Engineering*, 13, 10-14, 1974.
- Ligda, M.G.H., Meteorological Observation with Pulsed Laser Radar, *Proc. Conf. Laser Technol.*, 1st, San Diego, U.S. Navy, 63, 1963.
- McCormick, M.P., The Use of Lidar for Atmospheric Measurements, *Remote Sensing Energy Related Studies*, edited by T.N. Vezeroglu, Hemisphere Press, Washington, Distributed by Wiley, N.Y., 113-218, 1975.
- McCormick, M.P., T.J. Swissler, W.P. Chu, and W.H. Fuller, Jr., Post-Volcanic Stratospheric Aerosol Decay as Measured by Lidar, *Journal of the Atmospheric Sciences*, 35, 1296-1303, 1978.
- McCormick, M.P., T.J. Swissler, W.H. Fuller, Jr., W.H. Hunt, and M.T. Osborn, Air Borne and Ground-Based Lidar Measurements of the El Chichon Stratospheric Aerosol from 90 °N to 56 °S, *Geofisica Internacional*, 23-2, 187-221, 1984.
- McDermid, I.S., S.M. Godin, and L.O. Lindqvist, Ground-based Laser DIAL System for Long-term Measurements of Stratospheric Ozone, *Applied Optics*, 29, 3603-3612, 1990.
- Mckinley, S.C., *Water Vapor Distribution and Refractive Properties of the Troposphere*, Master thesis, Dept. of Electrical Engineering, the Pennsylvania State University, May 1994.
- Measures, R.M., *Laser Remote Sensing, Fundamentals and Applications*, Krieger Publishing, Malabar, F.L., 1992.

- Megie, G., M.L. Chanin, G.Y. Toulinov, Y.P. Doudoladov, High Latitude Measurements of the Atomic Sodium concentration and Neutral Temperature at the Mesopause Level by the Lidar Technique, *Planetary Sciences*, 26, 27-35, 1978a.
- Megie, G., F. Bos, J.E. Blamont, M.L. Chanin, Simultaneous Nighttime Lidar Measurements of Atmospheric Sodium and Potassium, *Planetary Sciences*, 26, 1978b.
- Melfi, S.H., Remote Measurements of the Atmosphere Using Raman Scattering, *Applied Optics*, 11, 1605-1610, 1972.
- Melfi, S.H., Remote Sensing for Air Quality Management, *Laser Monitoring of the Atmosphere*, Chapter 2, edited by E.D. Hinkley, Springer-Verlag, Berlin, Heidelberg, 1976.
- Melfi, S.H., J.D. Lawrence, Jr., and M.P. McCormick, Observation of Raman Scattering by Water Vapor in the Atmosphere, *Applied Physics Letters*, 15, 295-297, 1969.
- Melfi, S.H., D. Whiteman, Observation of Lower-Atmospheric Moisture Structure and It's Evolution Using a Raman Lidar, *Bulletin American Meteorological Society*, 66, 1288-1292, 1985.
- Melfi, S.H., D. Whiteman, R. Ferrare, Observation of Atmospheric Fronts Using Raman Lidar Moisture Measurements, *Journal of Applied Meteorology*, 28, 789-806, 1989.
- Metzger, L.T., and C.S. Gardner, Temperature Determination from a Rayleigh Lidar, *Technical Report, EOSL No. 89-001*, University of Illinois at Urbana-Champaign, 1989.
- Mie, G., Beitrage zur Optik trüber Medien speziell kolloidaler Metallösungen, *Ann. Phys.*, 25, 377-445, 1908.
- Miller, M.S., C.S. Gardner, and C.H. Liu, Rayleigh Lidar Observations of Gravity Wave Activity in the Stratosphere and Lower Mesosphere, Electro-Optic Systems Laboratory, Department of Electrical and Computer Engineering, University of Illinois, *Technical Report, EOSL No. 87-008*, 1987.
- Nedeljkovic, D., A. Hauchecorne, and M.L. Chanin, Rotational Raman Lidar to Measure the Atmospheric Temperature from the Ground to 30 km., *IEEE Transactions on Geoscience and Remote Sensing*, 31, 90-101, 1993.
- Papayannis, A., G. Ancellet, J. Pelon, and G. Mégie, Multiwavelength Lidar for Ozone Measurements in the Troposphere and the Lower Stratosphere, *Applied Optics*, 29, 467-476, 1990.
- Pettifer, R.E.W. Signal Induced Noise in Lidar experiments, *Journal of Atmospheric and Terrestrial Physics*, 37, 669-673, 1975.
- Pettifer, P.E.W., and P.G. Healey, Signal Induced Noise in a 56 TUVF Photomultiplier, *Journal of Physics E: Scientific Instruments*, 7, 617-620, 1974.

- Philbrick, C.R., Measurements of the High Latitude Middle Atmosphere Dynamic Structure Using Lidar, *Environmental Research Papers*, No. 967, AFGL-TR-87-0053, 1987.
- Philbrick, C.R., and B. Chen, Transmission of Gravity Waves and Planetary Waves in the Middle Atmosphere Based on Lidar and Rocket Measurements, *Advance Space Research*, 12, 303-306, 1992.
- Philbrick, C.R., D.B. Lysak, T.D. Stevens, P.A.T. Haris, Y.C. Rau, Atmospheric Measurements Using the LAMP lidar during the LADIMAS Campaign, *16th International Laser Radar Conference*, Proceedings of the NASA Conference, MIT, Cambridge, Massachusetts, 1992
- Philbrick, C.R., D.P. Sipler, G. Davidson, W.P. Moskowitz, Remote Sensing of structure properties in the middle atmosphere using lidar, *Laser and Optical Remote Sensing: Instrumentation and Techniques Topical Meeting*, Optical Society of American, 123, 1987.
- Philbrick, C.R., F.R. Schmidlin, K.U. Grossman, G. Lange, D. Offermann, K.D. Baker, D. Krankowsky, and U. von Zahn, Density and temperature structure over northern Europe, *J. Atmos. Terr. Phys.*, vol. 47, pp. 159, 1985.
- Potter, J.F., Two-frequency Lidar Inversion Technique, *Applied Optics*, 26, 1250-1256, 1 April, 1987.
- Raman, C.V., K.S. Krishnan, A New Type of Secondary Radiation, *Nature*, 121, 501, 1928.
- Raman, C.V., A Change of Wave-Length in Light Scattering, *Nature*, London, 121, 619, 1928.
- Renaut, D., J.C. Pourny, and R. Capitini, Daytime Raman-Lidar Measurements of Water Vapor, *Opt. Lett.*, 5, 233-235, 1980.
- Riebessel, M., A. Ansmann, and C. Weitkamp, Raman Lidar Measurement of the Atmospheric Aerosol Extinction Profile, *Optical Remote Sensing of Atmosphere, Technical Digest*, 4, 308-311, 1990.
- Russell, P.B., B.M. Morley, J.M. Livingston, G.W. Grams, and E.M. Patterson, Orbiting Lidar Simulations. 1: Aerosol and Cloud Measurements by an Independent-Wavelength Technique, *Applied Optics*, 21, 1541-1553, 1982a.
- Russell, P.B., B.M. Morley, Orbiting Lidar Simulations. 2: Density, Temperature, Aerosol, and Cloud Measurements by a Wavelength-Combining Technique, *Applied Optics*, 21, 1554-1563, 1982b.
- Sasano, Y., and E.V. Browell, Light Scattering Characteristics of Various Aerosol Types Derived from Multiple Wavelength Lidar Observations, *Applied Optics*, 28, 1989.
- Sacco, V.M., F. Castagnoli, M. Morandi, and L. Stefanutti, Elastic Backscattering Lidar System for Atmospheric Measurements in Antarctica, *Optical and Quantum Electronics*, 21, 215-226, 1989.

- Sandford M.C.W., and A.J. Gibson, Laser Radar Measurements of the Atmospheric Sodium Layer, *Journal of Atmospheric and Terrestrial Physics*, 32, 1423-1430, 1970.
- Schotland, R.M., Some Observation of the Vertical Profile of Water Vapor by a Laser Optical Radar, *Proceedings of Fourth Symposium on Remote Sensing of the Environment*, Univ. of Michigan, Ann Arbor, 273-283, 1966.
- Schwiesow, R.L., and R.E. Cupp, Remote Doppler Velocity Measurements of Atmospheric Dust Devil Vortices, *Applied Optics*, 15, 1-2, 1976.
- She, C.Y., Remote Measurement of Atmospheric Parameters: New Application of Physics with Lasers, *Contemporary Physics*, 31, 247-260, 1990.
- She, C.Y., H. Latifi, J.R. Yu, R.J. Alvarez II, and R.E. Bills, C.S. Gardner, Two-Frequency Lidar Technique for Mesospheric Na Temperature Measurements, *Geophysical Research Letter*, 17, 929-932, 1990.
- She, C.Y., J.R. Yu, J.W. Huang, and C. Nagasawa, Na Temperature Lidar Measurements of Gravity Wave Perturbations of Wind, Density and Temperature in the Mesopause Region, *Geophysical Research Letters*, 18, 1329-1331, 1991.
- She, C.Y., J.R. Yu, H. Latifi, and R.E. Bills, High Spectral Resolution Fluorescence Lidar for Mesospheric Sodium Temperature Measurements, *Applied Optics*, 31, 2095-2106, 1992.
- Shipley, S.T., D.H. Tracy, E.W. Eloranta, J.T. Trauger, J.T. Sroga, F.L. Roesler, and J.A. Weinman, High Spectral Resolution Lidar to Measure Optical Scattering Properties of Atmospheric Aerosols. 1: Theory and Instrumentation, *Applied Optics*, 22, 3716-3724, 1983.
- Sorga, J.T., E.W. Eloranta, S.T. Shipley, F.L. Roesler, and P.J. Tryon, High Spectral Resolution Lidar to Measure Optical Scattering Properties of Atmospheric Aerosols. 1: Calibration and Data Analysis, *Applied Optics*, 22, 3725-3732, 1983.
- Stevens, T.D., P.A.T. Haris, Y.C. Rau, C.R. Philbrick, Latitudinal Lidar Mapping of Stratospheric Particle Layers, *1992 STEP Symposium/COSPAR Meeting*.
- Strauch, R.G., V.E. Derr, and R.E. Cupp, Atmospheric Temperature Measurement Using Raman Backscatter, *Applied Optics*, 10, 2665-2669, 1971.
- Strauch, R.G., and A. Cohen, Atmospheric Remote Sensing with Laser Radar, *Remote Sensing of the Troposphere*, edited by V.E. Derr, U.S. Department of Commerce, National Oceanic and Atmospheric Administration, Chapter 23, 1972.
- Toon, O.B., E.V. Browell, S. Kinne, J. Jordan, An Analysis of Lidar Observations of Polar Stratospheric Clouds, *Geophysical Research Letters*, 17, 393-396, 1990.
- Uchino, O., M. Maeda, J. Kohno, T. Shibata, C. Nagasawa, and M. Hirono, Observation of

- Stratospheric Ozone Layer by a XeCl Laser Radar, *Applied Physics Letters*, 33, 1978.
- Uchino, O., and I. Tabata, Mobile Lidar for Simultaneous Measurements of Ozone, Aerosols, and Temperature in the Stratosphere, *Applied Optics*, 30, 2005-2012, 1991.
- USSA76, NOAA, NASA AND USAF, *U.S. Standard Atmosphere, 1976*, 52-66, 1976.
- van de Hulst, H.C., *Light Scattering by Small Particles*, Dover Publications, Dover Publications Inc., New York, 1981.
- von Zahn, U., P. von der Gathen, and G. Hansen, Forced Release of Sodium from Upper Atmospheric Dust Particles, *Geophys. Res. Lett.*, 14, 76-79, 1987.
- von Zahn, U., and T.L. Hansen, Sudden Neutral Sodium Layers: A Strong Link to Sporadic E Layers, *J. Atmos. Terr. Phys.*, 50, 93-104, 1988.
- Wilson, R., A. Hauchecorne, and M.L. Chanin, Gravity Wave Spectra in the Middle Atmosphere as Observed by Rayleigh Lidar, *Geophysical Research Letters*, 17, 1585-1588, 1990.
- Woodman, D.P., Limitations in Using Atmospheric Models for Transmission Estimations, *Applied Optics*, 13, 2193-2195, 1974.
- Zuev, V.E., *Laser Beams in the Atmosphere*, Consultants Bureau, New York, 1982.

VITA

Yi-Chung Rau received his BS degree in Electrical Engineering from the Chung-Yuan University, Taiwan, R.O.C. in 1980. In 1987 he received his MS degree in Electrical Engineering from State University of New York at Stony Brook in Stony Brook, New York. Currently, he is a PhD candidate in Electrical Engineering at the Pennsylvania State University. His research interests are in the area of lidar and optical remote sensing, optical instrumentations and communications, digital signal and image processing, artificial neural network, and middle atmospheric dynamics. He is a member of the Institute of Electrical and Electronics Engineers (IEEE) and the American Geophysical Union (AGU).